

Investigation of Plasmonic Structures by Light and Electron Microscopy: Contributions to an Efficient Numerical Treatment

Dissertation

zur Erlangung des akademischen Grades

Doctor rerum naturalium (Dr. rer. nat.)

vorgelegt der

Naturwissenschaftlichen Fakultät II - Chemie, Physik und Mathematik
der Martin-Luther-Universität Halle-Wittenberg



von

Christian F. Matyssek

geboren am 28.12.1982 in Rinteln

Halle, den 30.03.2012 (Tag der Abgabe)

Tag der Verteidigung: 23.07.2012

Gutachter:

- 1: Prof. Dr. Wolfram Hergert (Betreuer)
Universität Halle-Wittenberg
- 2: Prof. Dr. Matrin Arnold
Universität Halle-Wittenberg
- 3: Prof. Dr. Lukas Eng
Technische Universität Dresden

Contents

Preface	iv
1 Notation and Conventions	v
2 Nomenclature	vi
3 List of Abbreviations	vii
1 Introduction	1
2 Electrodynamics	3
2.1 Maxwell's Equations	3
2.1.1 Material Properties — Constitutive Relations	3
2.1.2 The Wave Equation	6
2.1.3 Boundary Conditions	6
2.1.4 Electrodynamic Potentials	7
2.1.5 Frequency Domain Electrodynamics	8
2.1.6 Scale Invariance of Maxwell's equations	8
2.1.7 Constraints on the Fourier Components	9
2.1.8 Waves in Frequency Domain — the Helmholtz Equation	9
2.2 Plane Waves	12
2.3 Scattering Theory	13
2.4 Optical Properties of Metals	16
2.4.1 Drude model - Permittivity of the free Electron Gas	16
2.4.2 Lorentz Model	17
2.4.3 Permittivity Measurements	18
2.4.4 Permittivities used in this Thesis	19
2.4.5 Advanced Models	20
2.5 Plasmonics — Electrodynamics with Metals	21
2.5.1 Surface Plasmon Polaritons at planar Interfaces	21
2.5.2 Localized Surface Plasmon Polaritons	24
3 Numerical Methods	26
3.1 Mie Theory	27
3.1.1 Scalar Wave Functions	27
3.1.2 Vector Wave Functions	29
3.1.3 Field Expansion	30
3.1.4 Solution of the Scattering Problem	31
3.1.5 Incident Plane Wave	32
3.1.6 Scattering from a Spherical Particle	32

Contents

3.1.7	Remarks	34
3.2	T-Matrix and Null-Field Method	34
3.2.1	Representation Theorems for Electromagnetic Fields	35
3.2.2	The Null-Field Method	37
3.2.3	Remarks	39
3.3	Discontinuous Galerkin Time-Domain Method	39
3.3.1	Tessellation of the Computational Domain	40
3.3.2	Inter-element Coupling	41
3.3.3	Semi-discretization of the Problem	42
3.3.4	Time Stepping	43
3.3.5	Extensions	46
3.4	Finite Element Method	48
3.5	Other Methods	49
3.5.1	Time Domain Methods	49
3.5.2	Frequency Domain Methods	49
4	Shape Transformation of Silver Nano-Particles in Glass	51
4.1	Samples and Experimental Setup	51
4.2	Shape Transformation	53
4.3	Simulating the Experiment	54
4.3.1	Modeling the Experiment	54
4.3.2	Comparison of Numerical Methods	55
4.3.3	Scattering Efficiency	56
4.3.4	Near-field Distribution	57
4.3.5	Field Enhancement as a Function of Aspect Ratio	59
4.4	Conclusion	62
5	Electron Microscopy on Metallic Nano-Particles	63
5.1	Electron Energy Loss Spectroscopy	64
5.2	Cathodoluminescence Spectroscopy	65
5.3	Electron Microscopy on Metal Nano-Particles — A Literature Survey	66
5.4	The Loss- and Cathodoluminescence-Probability	67
5.4.1	Analytical and Numerical Results	70
5.4.2	Loss Probability in Experiments	71
5.4.3	Dimensionless Units	71
6	The T-Matrix Method for Electron Microscopy	72
6.1	Electron Excitation	72
6.2	Calculation of the Loss- and Cathodoluminescence-Probability	74
6.3	Results	75
6.3.1	Spherical Particle	76
6.3.2	Spheroidal Particles	81
6.3.3	Dimers of Spheres	84
6.4	Conclusion	88

Contents

7	The Discontinuous Galerkin Time-Domain Method for Electron Microscopy	89
7.1	Electron Excitation	89
7.2	Sphere - Discretization and Accuracy	92
7.2.1	Finite Simulation Time	94
7.2.2	Finite Computational Domain	95
7.2.3	Spatial Resolution	96
7.3	Spheroid — Far-field Patterns and Cathodoluminescence	97
7.3.1	Cathodoluminescence	97
7.3.2	Far-field Patterns	97
7.4	Sphere Dimer - Dark Mode Excitation	99
7.4.1	Time-Evolution of the Excited Fields	99
7.4.2	Dark and Bright Mode Excitation	100
7.5	Sphere Dimer as a Nano-Antenna	102
7.6	Sierpinski Triangle	105
7.7	Split Ring Resonator - Babinet's Principle	107
7.8	Conclusion	109
8	Conclusion and Outlook	111
	Bibliography	113
	Publication List	121
	Curriculum Vitae	122
	Eidesstattliche Erklärung	123
	Acknowledgements	124

Preface

Amongst all phenomena of the physical world, light might be the one which has captured mankind's minds and curiosity most. Not only has it been subject of scientific interest, but it also has found its way into literature and history in numerous metaphors, from *Let there be Light* to the age of *enlightenment*. The variety of metaphors corresponds to the wide range of ways vision influences the way men perceive the world around them. Understanding the nature of light has captured some of the finest minds who ever lived, from the ancient Greeks, e.g. Euclid¹, who studied the geometric aspects of vision, to Isaac Newton², who found light must consist of a stream of particles. Johann Wolfgang von Goethe³ studied the colors and gave a comprehensive account in his work *Zur Farbenlehre*. It took, however, some more time until a mathematical theory of light was established. In what can be considered one of the biggest intellectual achievement of all times, James Clerk Maxwell⁴ unified the existing theories of electricity and magnetism, which allowed him to identify light with electromagnetic radiation. This allowed different kinds of radiation, known as x-rays, visible light, infrared light, etc., to be regarded as similar phenomena, i.e. electromagnetic waves with different wavelengths. Besides yielding an overwhelming variety of applications, this discovery also influenced science itself. It was the electrodynamics of moving bodies that lead Albert Einstein⁵ to the Theory of Relativity. It is amazing that the equations Maxwell used to describe the electromagnetic fields are found to be accurate on astronomic length scales down to the nano-meter scale, where the accurate description of matter already requires quantum mechanics. With modern advances in nano-fabrication, it is an interesting question to what extend the classical description based on Maxwell's equations remain valid. This question is the concern of current research involving the optical properties of metallic nano-particles, falling in a rapidly growing field called *Plasmonics*. Plasmonics employs both, high-precision fabrication and experimental techniques on the one hand, and sophisticated numerical methods to simulate the experiments on the other. Having accurate, efficient numerical methods at hand will help to better understand experimental data and also will help to find new properties, optimal geometries and facilitates testing without the effort of sample preparation and expansive measurement equipment. It is this field of numerical methods for Plasmonics that this Thesis tries to contribute to. Before giving a detailed introduction to the Thesis and its topics, we will first give an overview of used notation, conventions and abbreviations.

¹* 360 B.C., † 280 B.C.

²* Woolsthorpe 4.1.1643, † Kensington 31.3.1727

³* Frankfurt a.M. 28.08.1749, † Weimar 22.03.1832

⁴* Edinburgh 13.6.1831, † Cambridge 5.11.1879

⁵* Ulm 14.3.1879, † Princeton 18.4.1955

1 Notation and Conventions

Space and time are regarded as natural domains for physical processes. Where convenient, we use the Fourier transform and the inverse Fourier transform as follows:

$$f(t) = \int d\omega f(\omega)e^{-i\omega t}, \quad (1a)$$

$$f(\omega) = \frac{1}{2\pi} \int dt f(t)e^{i\omega t}. \quad (1b)$$

Vectors are written in **bold** face, e.g. \mathbf{r} , \mathbf{E} , matrices are denoted by **bold underlined** letters, e.g. $\underline{\mathbf{T}}$. As we work in both, time and frequency domain, we use regular letters (e.g. $\mathbf{E} = \mathbf{E}(\mathbf{r}, t)$) for time-domain quantities and script letters (e.g. $\mathcal{E} = \mathcal{E}(\mathbf{r}, \omega)$) for frequency-domain quantities. This allows us to omit the arguments in certain calculations without causing confusion. SI units are used unless mentioned otherwise.

We often plot wavelength and frequency-dependent quantities. It has become customary to specify the frequency in units of electron volts. This has to be understood as the energy $E = \hbar\omega$ a photon of frequency ω carries. Those readers who are more acquainted with wavelength plots will benefit from the graph in Fig. 1 that relates photon energy in electron volts to vacuum wavelength in nanometers.

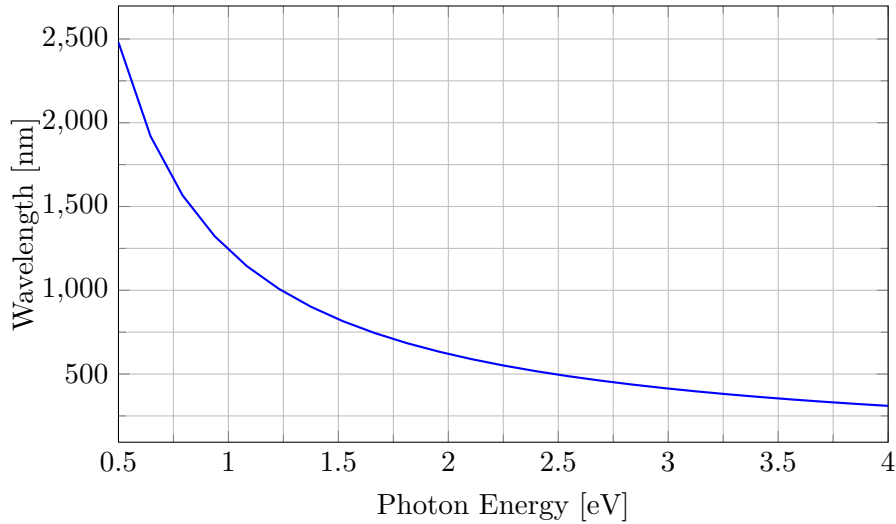


Figure 1: Photon energy versus vacuum wavelength of the electromagnetic wave.

2 Nomenclature

Frequently used physical quantities and notations are:

\mathbf{E}, \mathcal{E}	Electric field; time, frequency domain
\mathbf{H}, \mathcal{H}	Magnetic field; time, frequency domain
\mathbf{D}, \mathcal{D}	Electric displacement field; time, frequency domain
\mathbf{B}, \mathcal{B}	Magnetic flux density; time, frequency domain
$\varepsilon = \varepsilon_1 + i\varepsilon_2$	Complex permittivity
$\varepsilon_i, \varepsilon_e$	Permittivity in the interior and exterior of a scatterer
$n = n_1 + in_2$	Complex refractive index
μ	Permeability
μ_i, μ_e	Permeability in the interior and exterior of a scatterer
ω	Angular frequency
$\partial_t f(t), \frac{\partial f(t)}{\partial t}$	Partial derivative, in this example with respect to time
λ, λ_0	Wavelength, in vacuum
\mathbf{k}, \mathbf{k}_0	Wavevector, in vacuum
$\mathbf{e}_x, \mathbf{e}_y, \mathbf{e}_z$	Unit vectors in Cartesian coordinates
$x, y, z \in (-\infty, +\infty)$	Cartesian Coordinates
$\mathbf{e}_r, \mathbf{e}_\vartheta, \mathbf{e}_\varphi$	Unit vectors in spherical coordinates
$r \in [0, \infty)$	Spherical coordinate, distance to origin
$\vartheta \in [0, \pi]$	Spherical coordinate, angle between positive z-axis and \mathbf{e}_r
$\varphi \in [0, 2\pi)$	Spherical coordinate, angle between positive x-axis and \mathbf{e}_r
A^*	Complex conjugate of the quantity A
$\overleftrightarrow{\mathbf{G}}, \overleftrightarrow{\mathbf{I}}$	Dyadic quantities, Unit dyad

3 List of Abbreviations

ADE	Auxiliary Differential Equations, page 17
BEM	Boundary Element Method, page 50
CL	Cathodoluminescence, page 65
CLP	Cathodoluminescence Probability, page 69
CLS	Cathodoluminescence Spectroscopy, page 65
DDA	Discrete Dipole Approximation, page 49
DGTD	Discontinuous Galerkin Time-Domain Method, page 39
EEL	Electron Energy Loss, page 64
EELP	Electron Energy Loss Probability, page 68
EELS	Electron Energy Loss Spectroscopy, page 64
FD	Frequency-Domain, page 26
FDTD	Finite Difference Time Domain, page 49
FEM	Finite Element Method, page 48
LSP	Localized Surface Plasmons, page 24
LSRK	Low Storage Runge-Kutta, page 44
MMP	Multiple Multipole, page 49
NFM	Null-Field Method, page 35
NRA	No-Recoil Approximation, page 69
PEC	Perfect Electric Conductor, page 47
PML	Perfectly Matched Layers, page 48
QSA	Quasi-static Approximation, page 11
RK	Runge-Kutta methods, page 44
SF	Scattered-Field, page 46
SP	Surface Plasmon, page 23
SPP	Surface Plasmon Polariton, page 22
SRR	Split Ring Resonators, page 107
SVWF	Spherical Vector Wave Functions, page 30
SWF	Scalar Wave Functions, page 27
TD	Time-Domain, page 26
TFSF	Total-Field/Scattered-Field, page 46
UPML	uni-axial PML, page 48
VWF	Vector Wave Functions, page 29
ZLP	Zero-Loss Peak, page 65

1 Introduction

Plasmonics. Briefly, this rapidly growing field of research could be characterized as *optics with metals in the nano-regime*. Thus, plasmonics deals with the interaction of light with metallic nano-particles, particle systems or other structures. Among the first applications of Plasmonics might be the coloring of church windows. By adding certain materials during the production process, nano-particles form inside the glass giving rise to the beautiful colors. Of course, back then, this application was far from being well-understood. A deeper understanding required the mathematical theory of light given by J.C. Maxwell 1865 [1]. In Chapter 2 we will review some fundamentals from electrodynamics in both, time- and frequency-domain. The basic concepts in light scattering will be introduced. After that, we will discuss the optical properties of metals, which give rise to new phenomena, such as electromagnetic waves localized at metal-insulator interfaces - the so-called *Surface Plasmon*. They are crucial for the optics of metallic nano-particles. Another important milestone in the history of Plasmonics was the solution of the scattering problem for spherical particles given by G. Mie 1908 [2]. With this, it was possible to calculate the optical resonances of metallic nano-particles, which are in the visible regime for certain materials and due to the strong absorption near the resonance wavelengths can give rise to the color of windows, for example. We will discuss Mie theory in Chapter 3 of this Thesis which will allow us to discuss the optical properties of spherical metallic nano-particles. Going to more general particle shapes usually requires the use of numerical methods. We will introduce two other methods in more detail. The first method is the T-Matrix method, which can be considered as a generalization of Mie theory. It is a semi-analytical approximative method yielding accurate results with relatively low computational demands and can treat particles of more general shape. The second method is the Discontinuous Galerkin Time-Domain method. It is even more flexible, allowing particles of arbitrary shape. Being a time-domain method, it is potentially more flexible concerning the mathematical description of the material properties - a feature that is desirable since typical particle dimensions have reached length scales, where improved material models might be necessary. Furthermore, we will mention other methods that are commonly encountered in electrodynamics simulations and briefly characterize them.

The extensive use of numericals method to the problem of light-scattering by metallic nano-particles will be the topic of Chapter 4. It is known from experiments that spherical silver nano-particles in glass undergo a shape transformation when irradiated with laser pulses. The transformation process is believed to depend on the electric near-field at the particles. We will therefore be concerned with the calculation of the optical properties of silver nano-particles and first compare different numerical methods in terms of computation time and accuracy. Then, we calculate the properties related to the

1 Introduction

transformation process to see whether there is evidence to support the process model. While the experimental technique allows to tailor the optical properties of the particles to some extent, it is possible to do this in a more targeted manner.

With the recent decades' advances in nano-fabrication and with modern measurement equipment it is possible to manufacture and characterize nano-structures with unprecedented accuracy. This could facilitate the production of functional plasmonic structures. The typical time-scales are in the order of femtoseconds and due to the special properties of plasmonic structures, electromagnetic energy can be confined to sub-wavelength regions. This would not be possible with conventional photonic components, which usually require spatial dimensions of half a wavelength. Being metallic, fast and small, plasmonic structures could be combined into existing integrated circuits and are candidates for fast and efficient computing devices [3].

While such applications might be rather far from being realizable right now, there are already application of plasmonic particles, e.g. as highly sensitive sensors [4] or to increase the efficiency of photovoltaic systems [5]. Therefore it is important to investigate the properties of plasmonic systems and how they could potentially pave the way for further applications. Recently, Electron Microscopy was introduced as a tool to study plasmonic particles [6, 7] and since then, an ever increasing number of experiments is published. Two important experimental techniques that facilitate the study of the plasmonic properties of individual metallic nano-particles are Electron Energy Loss Spectroscopy and Cathodoluminescence Spectroscopy. In Chapter 5 we will introduce these two techniques, present results from the literature and will establish the relation between the experimental results and the simulation. With this as a prelude, we come to the main topic of this thesis, which is the modification of two existing numerical methods making possible the simulation of Electron Energy Loss Spectroscopy and Cathodoluminescence Spectroscopy. In Chapter 6 we will extend the T-Matrix method to be applicable for such simulations. We derive the necessary modifications, test the method for convergence and will present results for particle-shapes that are also frequently encountered in experiments.

In Chapter 7 we will extend the Discontinuous Galerkin Time-Domain method to be also applicable for such simulations. First, we will perform tests on simple particle shapes compare some of the results with T-Matrix results to see whether the time-domain and the frequency-domain method results are in agreement. We will see that the agreement is excellent and will make use of the flexibility regarding the particle shape to treat complicated geometries. Also, we will exploit the time-domain approach to study the time evolution of the electromagnetic fields.

Finally, we will conclude the Thesis and see that we have introduced two new frameworks to perform Electron Energy Loss and Cathodoluminescence Spectroscopy simulations, the one being very efficient, the other one being flexible regarding the particle geometry.

2 Electrodynamics

In this chapter we will present the mathematical preliminaries enabling us to describe the propagation of electromagnetic waves in matter with special focus on metals. The reasoning in this chapter follows standard text books. For electrodynamics in general, we refer the reader to the book by Jackson [8]. For an introduction to plasmonics, we recommend the book by Maier [9].

2.1 Maxwell's Equations

The propagation of electromagnetic waves in space and time is described by Maxwell's equations. The equations were published in Maxwell's famous 1865 paper *A dynamical Theory of the Electromagnetic Field* [10] and later in his *Treatise on Electricity and Magnetism* [1]. Originally given in quaternion notation, today they are usually given in vector form and read

$$\nabla \cdot \mathbf{B}(\mathbf{r}, t) = 0 \quad (2.1a)$$

$$\nabla \times \mathbf{H}(\mathbf{r}, t) = \frac{\partial \mathbf{D}(\mathbf{r}, t)}{\partial t} + \mathbf{J}_s(\mathbf{r}, t) \quad (2.1b)$$

$$\nabla \cdot \mathbf{D}(\mathbf{r}, t) = \rho_s(\mathbf{r}, t) \quad (2.1c)$$

$$\nabla \times \mathbf{E}(\mathbf{r}, t) = -\frac{\partial \mathbf{B}(\mathbf{r}, t)}{\partial t} \quad (2.1d)$$

where $\mathbf{E}(\mathbf{r}, t)$ is the *electric field*, $\mathbf{D}(\mathbf{r}, t)$ is the *electric displacement field*, $\mathbf{H}(\mathbf{r}, t)$ is the *magnetic field* and $\mathbf{B}(\mathbf{r}, t)$ is the *magnetic flux density*. $\mathbf{J}_s(\mathbf{r}, t)$ and $\rho_s(\mathbf{r}, t)$ represent an external current and charge distribution, respectively. These distributions act as sources to the fields, i.e. charges give rise to electric fields (Eq. (2.1c)) and currents give rise to magnetic fields (Eq. (2.1b)). In the following, we will often omit the arguments (\mathbf{r}, t) for convenience.

2.1.1 Material Properties — Constitutive Relations

Matter consists of charged particles and, under the effect of an electromagnetic field, may contribute to the charge density as well as the current density. From Eqns. (2.1b) and (2.1c) it is apparent that these additional charges and currents act as sources to the fields \mathbf{H} and \mathbf{D} , respectively. Therefore, these two fields can be regarded as auxiliary fields that take into account the influence of matter and are functions of the other fields

2 Electrodynamics

\mathbf{E} and \mathbf{B} , respectively, such that

$$\mathbf{D} = \mathbf{D}(\mathbf{E}), \quad (2.2a)$$

$$\mathbf{H} = \mathbf{H}(\mathbf{B}). \quad (2.2b)$$

The most general case would be $\mathbf{D} = \mathbf{D}(\mathbf{E}, \mathbf{B})$ and $\mathbf{H} = \mathbf{H}(\mathbf{B}, \mathbf{E})$, but this material class will not be considered here. It is convenient to introduce another two auxiliary fields such that

$$\mathbf{D} = \varepsilon_0 \mathbf{E} + \mathbf{P}, \quad (2.3a)$$

$$\mathbf{H} = \frac{1}{\mu_0} \mathbf{B} + \mathbf{M}, \quad (2.3b)$$

where we have introduced the *polarization* \mathbf{P} and the *magnetization* \mathbf{M} . Furthermore we have introduced the *vacuum permittivity* ε_0 and the *vacuum permeability* μ_0 . Often, Eq. (2.3b) is cast into a form similar to (2.3a) such that

$$\mathbf{B} = \mu_0 (\mathbf{H} + \mathbf{M}). \quad (2.4)$$

Materials can be classified according to the properties of \mathbf{P} and \mathbf{M} . In natural materials, the magnetic response at optical frequencies is usually small. For that reason, most textbooks use $\mathbf{B} = \mu_0 \mathbf{H}$ and we will also restrict ourselves to this class of materials and only consider the permittivity ε . However, artificially fabricated materials can show a considerable magnetic response at optical frequencies. One example of which are the so called *metamaterials* [11], which usually have a special microstructure, like Split Ring Resonators that we will encounter in Chap. 7. Therefore, the following classification of the permittivity ε also applies to the permeability μ .

Linear isotropic

For the description of many materials, a linear isotropic relationship is a good approximation, i.e.

$$\mathbf{D} = \varepsilon_0 \varepsilon \mathbf{E}. \quad (2.5)$$

One special linear material is the vacuum. Here, $\mathbf{D} = \varepsilon_0 \mathbf{E}$ and $\mathbf{B} = \mu_0 \mathbf{H}$.

Linear anisotropic

The atomic order of matter may play a role in the electromagnetic response. For example, in a crystal the response may depend on the direction of the applied field relative to the crystal lattice. Such a behaviour is taken into account by a tensorial permittivity

$$D_i = \varepsilon_0 \sum_{j=1}^3 \varepsilon_{ij} E_j. \quad (2.6)$$

Nevertheless, most solids are well described as isotropic media.

Nonlinear

We have introduced the polarization \mathbf{P} as the response of a material to a certain electric field \mathbf{E} . As \mathbf{P} can be considered as a function of \mathbf{E} , we can approximate it by a Taylor expansion

$$P_i(\mathbf{E}) = \sum_j \chi_{ij}^{(1)} E_j + \sum_{jk} \chi_{ijk}^{(2)} E_j E_k + \sum_{jkl} \chi_{ijkl}^{(3)} E_j E_k E_l + \dots \quad (2.7)$$

Here, the $\chi^{(i)}$ are called the *susceptibility tensors*. For small amplitudes of the applied field \mathbf{E} we obtain the linear relation that we have already introduced above. For higher amplitudes that can for example be generated with lasers, the higher order susceptibilities have to be taken into account. The nonlinearity gives rise to a number of interesting physical effects like, for example, higher harmonic generation [12]. However, it also renders the superposition principle invalid on which the frequency domain solution of Maxwell's equations is based (cf. Sec. 2.1.5). Thus, for non-linear materials one will in general have to solve Maxwell's equations in the time-domain.

Temporally dispersive, non-local in time

So far, the relations above have all been *local* and *instantaneous*, however, in general they can possess a non-local character. Non-locality in time means that the field values at a given time may depend on all past field values

$$\mathbf{D}(\mathbf{r}, t) = \int_{-\infty}^{+\infty} d\tau \varepsilon(\tau) \mathbf{E}(\mathbf{r}, \tau - t). \quad (2.8)$$

We will see in Sec. 2.1.5 that such a relationship results in a frequency dependent permittivity and is encountered, e.g., in metals.

Spatially dispersive, non-local in space

A non-locality in space is also possible, such that the field values at a given coordinate depend on those at other coordinates at the same time

$$\mathbf{D}(\mathbf{r}, t) = \int_{-\infty}^{+\infty} d^3\mathbf{r}' \varepsilon(\mathbf{r}, \mathbf{r}') \mathbf{E}(\mathbf{r}', t). \quad (2.9)$$

One example for such behaviour can be found in metals. We assume that a conduction electron is accelerated by an electric field at some position. Then, some instants later it will cause a field at its current position. This means that we have both, non-locality in space and time, originating from electronic transport. This also demonstrates that in real materials the different types of responses are not as well separated as in the discussion above. It is then important to find relations that give a reasonable approximation to

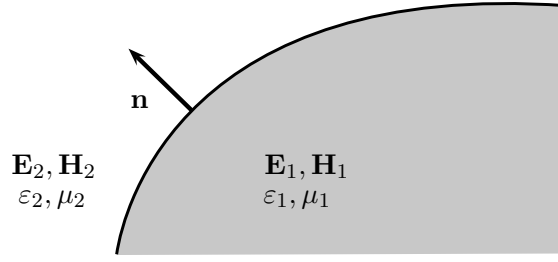


Figure 2.1: Boundary between two materials with properties ε_1, μ_1 and ε_2, μ_2 . \mathbf{n} is the unit vector normal to the interface.

reality, i.e. that show a good agreement with experiments.

2.1.2 The Wave Equation

Let us assume a linear medium with permittivity ε and permeability μ and the absence of any charges and currents. Then we can apply the curl operator to Eq. (2.1d) and obtain

$$\nabla \times \nabla \times \mathbf{E} = -\nabla \times \dot{\mathbf{B}}. \quad (2.10)$$

By using $\mathbf{B} = \mu_0\mu\mathbf{H}$, $\mathbf{D} = \varepsilon_0\varepsilon\mathbf{E}$ and Eq. (2.1b), we see that

$$\nabla \times \nabla \times \mathbf{E} = -\mu_0\mu\nabla \times \dot{\mathbf{H}} = -\mu_0\mu\varepsilon_0\varepsilon\ddot{\mathbf{E}}. \quad (2.11)$$

With the vector identity $\nabla \times \nabla \times \mathbf{E} = \nabla(\nabla \cdot \mathbf{E}) - \Delta\mathbf{E}$ and Eq. (2.1c) we finally obtain

$$\left(\Delta - \mu_0\mu\varepsilon_0\varepsilon \frac{\partial^2}{\partial t^2} \right) \mathbf{E} = 0. \quad (2.12)$$

This is the *wave equation* in vector form, which means that each and every component of \mathbf{E} satisfies the wave equation and the same equation can be derived for \mathbf{H} . In vacuum, the propagation speed of the waves is $c_0^2 = \frac{1}{\varepsilon_0\mu_0}$. We see that in matter the propagation speed is $c^2 = \frac{1}{\varepsilon_0\varepsilon\mu_0\mu} = \frac{c_0^2}{n^2}$ where we have introduced the *refractive index* $n = \sqrt{\varepsilon\mu}$.

2.1.3 Boundary Conditions

Material interfaces play a crucial role in electrodynamics. For example, they lead to reflection of electromagnetic waves and they can support a variety of surface waves [13], one special type of which is the surface plasmon that we will discuss in detail later in this chapter.

Assume a boundary between two materials, material 1 with permittivity and permeability (ε_1, μ_1) and material 2 with (ε_2, μ_2) as shown in Fig. 2.1. Then, the fields obey

2 Electrodynamics

the following boundary conditions at the interface

$$\mathbf{n} \cdot (\mathbf{B}_2 - \mathbf{B}_1) = 0, \quad (2.13a)$$

$$\mathbf{n} \times (\mathbf{H}_2 - \mathbf{H}_1) = \mathbf{J}_S, \quad (2.13b)$$

$$\mathbf{n} \cdot (\mathbf{D}_2 - \mathbf{D}_1) = \sigma_S, \quad (2.13c)$$

$$\mathbf{n} \times (\mathbf{E}_2 - \mathbf{E}_1) = 0, \quad (2.13d)$$

where \mathbf{j}_S and σ_S are surface current and charge densities and \mathbf{n} is the unit vector normal to the interface. The boundary conditions are a direct consequence of Maxwell's equations and any solution of Maxwell's equations for inhomogeneous materials must obey these conditions. Especially in Mie theory discussed in Sec. 3.1 and in the T-Matrix method discussed in Sec. 3.2 the boundary conditions are of importance for the determination of a solution.

2.1.4 Electrodynamic Potentials

The electric and magnetic fields are vector field quantities. A vector field is uniquely defined if its curl and divergence are known. Specifically, if the divergence of the field vanishes, it consists solely of a rotational part. Considering Eq. (2.1a), this means that we can write the magnetic flux density as

$$\mathbf{B} = \nabla \times \mathbf{A}, \quad (2.14)$$

where \mathbf{A} is the *vector potential*. Inserting this into Eq. (2.1d), we obtain

$$\nabla \times \left(\mathbf{E} + \frac{\partial \mathbf{A}}{\partial t} \right) = 0. \quad (2.15)$$

Because the rotation of a gradient field is always zero, we can rewrite the expression in brackets above as gradient of a scalar function φ , or likewise

$$\mathbf{E} = -\nabla\varphi - \frac{\partial \mathbf{A}}{\partial t}. \quad (2.16)$$

The function φ is called the *scalar potential*. The scalar and vector potential φ, \mathbf{A} are mathematical constructs that sometimes simplify the analysis. There is a certain freedom of choice, as we can always add the gradient of some function χ to the vector potential leaving the magnetic flux density invariant, because

$$\mathbf{B}' = \nabla \times \mathbf{A}' = \nabla \times (\mathbf{A} + \nabla\chi) = \nabla \times \mathbf{A} + \underbrace{\nabla \times \nabla\chi}_{=0} = \mathbf{B}. \quad (2.17)$$

Then, we see that choosing $\varphi' = \varphi - \partial_t\chi$ leaves \mathbf{E} invariant. This freedom of choice for \mathbf{A}, φ is called *gauge invariance*. The *Coulomb gauge* consists in choosing χ such that $\nabla \cdot \mathbf{A} = 0$. Another choice commonly encountered is the *Lorenz gauge* (often erroneously attributed to H.A. Lorentz [14]) which leads to $\nabla \cdot \mathbf{A} + \frac{1}{c^2}\dot{\varphi} = 0$. This choice

causes a decoupling of the equations governing the potentials. Furthermore this gauge is invariant under the Lorentz transformation and therefore often encountered in relativity calculations. In general, we will solve Maxwell's equations directly for the electric and magnetic field, however some calculations are more conveniently done for the potentials. We will use the potentials to calculate the field of a moving electron in Sec. 7.1.

2.1.5 Frequency Domain Electrodynamics

In this thesis, we will be concerned with linear materials and therefore, also the linear form of Maxwell's equations. With this, it is often convenient to perform a Fourier transform according to (1) on Page v with respect to time. Then, we are able to derive relations that are satisfied by the Fourier components of the fields. As noted in the preface we are going to use script letters for the Fourier components in order to avoid confusion when omitting the arguments (\mathbf{r}, ω) .

$$\nabla \cdot \mathcal{B}(\mathbf{r}, \omega) = 0 \quad (2.18a)$$

$$\nabla \times \mathcal{H}(\mathbf{r}, \omega) = -i\omega \mathcal{D}(\mathbf{r}, \omega) + \mathcal{J}_s(\mathbf{r}, \omega) \quad (2.18b)$$

$$\nabla \cdot \mathcal{D}(\mathbf{r}, \omega) = \rho_s(\mathbf{r}, \omega) \quad (2.18c)$$

$$\nabla \times \mathcal{E}(\mathbf{r}, \omega) = i\omega \mathcal{B}(\mathbf{r}, \omega) \quad (2.18d)$$

So basically the Fourier transform substitutes the time derivatives by the negative imaginary unit multiplied by the frequency $\partial_t \rightarrow -i\omega$, effectively turning the differential equation in time into an algebraic one.

By using the convolution theorem, we immediately see that the Fourier transform of the convolution of the electric field and the permittivity Eq. (2.8) turns out to be a product in frequency-domain, i.e.

$$\mathcal{D} = \varepsilon(\omega) \mathcal{E}. \quad (2.19)$$

Thus, a temporally dispersive material is described by a frequency-dependent permittivity.

2.1.6 Scale Invariance of Maxwell's equations

A special property of the homogeneous Maxwell's equations is the so-called scale invariance. Let $\mathcal{J}_s = \rho_s = 0$. Then we can introduce a scaling of the spatial coordinates with some factor a , i.e. $\mathbf{r}' = a\mathbf{r}$. We see that the equations (2.18) remain invariant if we rescale the frequency according to $\omega' = \omega/a$. If there are source terms, the equations remain invariant if we rescale the amplitude of the sources according to $\mathcal{J}'_s = \mathcal{J}_s/a$ and $\rho'_s = \rho_s/a$.

This scaling behaviour indicates that there is no typical length scale associated with Maxwell's equations.

2.1.7 Constraints on the Fourier Components

The relations between the Fourier components of the fields (2.18) follow directly from the time-dependent Maxwell equations (2.1). Beyond that, physical reasoning yields constraints on the Fourier components.

Physical Field are real-valued

Physical quantities like the electric and magnetic field in real space and time are required to be real-valued. To result in a real-valued field, the Fourier components of the fields must obey the relation

$$\mathcal{A}(\mathbf{r}, \omega) = \mathcal{A}(\mathbf{r}, -\omega)^* \quad (2.20)$$

where $\mathcal{A} \in \{\mathcal{E}, \mathcal{B}, \mathcal{H}, \mathcal{D}\}$.

Causality—Kramers-Kronig relations

The causality principle states that the cause always precedes the effect. In other words, a physical system is not influenced by its future states. Therefore, for temporally dispersive materials (2.8) the permittivity has to be a causal function, i.e. $\varepsilon(\tau) = 0 \forall \tau > 0$. It can be shown that the real and imaginary part of the Fourier components of causal function are not independent. Commonly, the relation between real and imaginary parts are written as the Kramers-Kronig relations [15].

1 *The real part of the Fourier components of the permittivity $\varepsilon = \varepsilon_1 + i\varepsilon_2$ can be expressed as a doubly infinite integral over the imaginary part and vice-versa*

$$\varepsilon_1(\omega_0) = \frac{1}{\pi} \mathcal{P} \int_{-\infty}^{+\infty} \frac{\varepsilon_2(\omega)}{\omega - \omega_0} d\omega \quad (2.21a)$$

$$\varepsilon_2(\omega_0) = -\frac{1}{\pi} \mathcal{P} \int_{-\infty}^{+\infty} \frac{\varepsilon_1(\omega)}{\omega - \omega_0} d\omega \quad (2.21b)$$

Here, \mathcal{P} denotes the principle value of the integral.

2.1.8 Waves in Frequency Domain — the Helmholtz Equation

From the equations governing the Fourier components of the fields (2.18) we can derive the *Helmholtz equation* in vectorial form

$$\nabla \times \nabla \times \mathcal{E} - k^2 \mathcal{E} = i\omega \mu_0 \mu \mathcal{J}, \quad (2.22)$$

with $k^2 = \omega^2 \varepsilon_0 \varepsilon \mu_0 \mu = \omega^2 / c^2$. It can be regarded as the frequency-domain equivalent of the wave equation. This equation can also be considered as an eigenvalue problem. To that end, we allow the medium to be inhomogeneous, i.e. $\varepsilon = \varepsilon(\mathbf{r})$ and assume no external charges and currents. Then, from Eqns. (2.18b) and (2.18d) we obtain

$$\nabla \times \frac{1}{\varepsilon(\mathbf{r})} \nabla \times \mathcal{H} = \frac{\omega^2}{c^2} \mathcal{H}. \quad (2.23)$$

2 Electrodynamics

Again, a similar equation can be derived for \mathcal{E} . The derivation must take the \mathbf{r} -dependence of ε into account. With this equation, it is possible to treat inhomogeneous media, one example of which are periodic dielectric structures, called photonic crystals [16, 17]. Another example of an inhomogeneous medium is a single particle embedded in a homogeneous medium. Such geometries will be considered throughout this thesis and we already discussed that the permittivity for metals is frequency-dependent. If we take the frequency dependence into account, the operator on the left-hand side depends on the eigenvalue. This makes the eigenvalue problem difficult to solve. The important consequence is, however:

2 *Any inhomogeneous medium, especially particles and particle systems, can sustain electromagnetic fields even in the absence of sources. These fields are the solutions of the eigenvalue problem (2.23) and are called eigenmodes of the system. Each eigenmode $\mathcal{H}_i, \mathcal{E}_i$ has an eigenfrequency ω_i associated to it.*

The notions *eigenmode* and *eigenfrequency* are crucial for the interpretation of the experiments we will discuss and the calculations we will perform in this thesis.

An alternative approach to particles and particle systems is to consider them as piecewise homogeneous materials. If we assume a homogeneous medium with no external currents and charges, the Helmholtz equation simplifies to

$$(\Delta + k^2) \mathcal{E} = 0. \quad (2.24)$$

Equally, the very same equation can be derived for \mathcal{H} . The general solutions of the Helmholtz equation in both, scalar and vector form will be discussed in more detail in Sec. 3.1. We can then use the general solution as an ansatz for the fields in each homogeneous part of the system and then use the boundary conditions (2.13) to determine the electromagnetic field in piecewise homogeneous media.

Green Function of the Helmholtz Equation

The Green function $g(x, x')$ of any linear operator L is defined as

$$L [g(x, x')] = \delta(x - x'), \quad (2.25)$$

where δ is the Dirac Delta distribution. It allows for a construction of particular solutions of inhomogeneous partial differential equations, i.e. $L[u(x)] = f(x)$. Then, the general solution can be written with the help of the Green function as

$$u(x) = u_0(x) + \int dx' g(x, x') f(x'), \quad (2.26)$$

where $u_0(x)$ is the general solution of the homogeneous equation $L[u_0(x)] = 0$.

3 The Green Function of the scalar Helmholtz equation in three dimensions is given by [8]

$$g(\mathbf{r}, \mathbf{r}') = \frac{e^{\pm ik|\mathbf{r}-\mathbf{r}'|}}{4\pi|\mathbf{r}-\mathbf{r}'|} \quad (2.27)$$

and has the form of a spherical outgoing (+) or incoming (-) wave.

The first one is called *retarded Green function*, the latter one *advanced Green function*. The exponential function in the numerator of (2.27) is the result of the finite propagation speed of electromagnetic waves and leads to so-called *retardation effects*.

In general, we will deal with the vector-valued electric and magnetic field and vector-valued currents can be the sources of the fields. To take this into account, we have to extend the concept of the scalar Green function to the *dyadic* Green function. A dyad can be considered as a second rank tensor that is formed by the juxtaposition of two vectors. Given two vectors \mathbf{a} and \mathbf{b} and orthonormal vectors $\mathbf{e}_1, \mathbf{e}_2, \mathbf{e}_3$, which satisfy $\mathbf{e}_i \cdot \mathbf{e}_j = \delta_{ij}$, we define the dyad

$$\overleftrightarrow{\mathbf{X}} = \mathbf{a} \circ \mathbf{b} = \sum_{i,j=1}^3 a_i b_j \mathbf{e}_i \circ \mathbf{e}_j. \quad (2.28)$$

We can right- and left-multiply a vector to a dyad, where the product acts on the right and left vector, respectively. Thus, such products reduce to the common vector-vector products. In the case of the scalar product between a vector and a dyad we obtain a vector, the cross product results in a dyad. A special dyad is the *unit dyad* defined by

$$\overleftrightarrow{\mathbf{I}} = \mathbf{e}_1 \circ \mathbf{e}_1 + \mathbf{e}_2 \circ \mathbf{e}_2 + \mathbf{e}_3 \circ \mathbf{e}_3 \text{ such that } \overleftrightarrow{\mathbf{I}} \cdot \mathbf{a} = \mathbf{a} \cdot \overleftrightarrow{\mathbf{I}} = \mathbf{a}. \quad (2.29)$$

With this, we can define the *dyadic Green function*, which is generated from the scalar one

$$\overleftrightarrow{\mathbf{G}}(\mathbf{r}, \mathbf{r}') = \left(\overleftrightarrow{\mathbf{I}} + \frac{1}{k^2} \nabla \circ \nabla \right) g(\mathbf{r}, \mathbf{r}'). \quad (2.30)$$

Therefore, the general solution of the vector Helmholtz Equation (2.22) can be written as For each component of \mathcal{J}_s , it gives the contribution to the three components of \mathcal{E} . With this, we know the electric and magnetic field

$$\mathcal{E} = \mathcal{E}_0 + i\omega\mu_0\mu \int d^3r' \overleftrightarrow{\mathbf{G}}(\mathbf{r}, \mathbf{r}') \mathcal{J}_s(\mathbf{r}, \mathbf{r}'), \quad (2.31)$$

$$\mathcal{H} = \mathcal{H}_0 + \int d^3r' \left[\nabla \times \overleftrightarrow{\mathbf{G}}(\mathbf{r}, \mathbf{r}') \right] \mathcal{J}_s(\mathbf{r}, \mathbf{r}'), \quad (2.32)$$

where $\mathcal{E}_0, \mathcal{H}_0$ are solutions of the homogeneous equation for the respective field.

Quasi-static Approximation

For certain problems the solution of the Helmholtz equation (2.24) can be quite involved. To simplify the analysis, sometimes the so-called Quasi-static Approximation (QSA) is

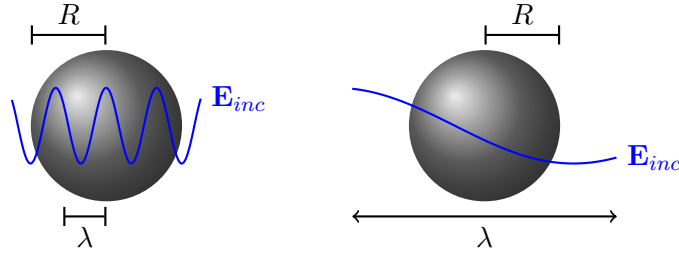


Figure 2.2: **Sketch of the Quasi-static approximation.** If the wavelength of the incident field inside the particle is much larger than the size of a considered particle, one may neglect the phase of the field and assume a homogeneous field instead. This simplifies the analysis where applicable.

employed. Let us assume a particle is irradiated with a plane wave of given wavelength λ as sketched on the left-hand side of Fig. 2.2. Then the fields inside the particle will oscillate and to actually calculate the field, we will have to solve the Helmholtz equation. If the radius of the particle is small as compared to the wavelength inside the particle $R \ll \lambda$ as sketched on the right-hand side of Fig. 2.2, we may neglect the variation of the phase $e^{i\mathbf{k}\cdot\mathbf{r}}$ over the particle and instead assume a homogeneous electric field as in electrostatics. Mathematically, this is equivalent of taking the limit $\lambda \rightarrow \infty$, or equivalently $|\mathbf{k}| = \frac{2\pi}{\lambda} \rightarrow 0$. In this limit, the Helmholtz equation becomes the Laplace equation. Physically, this means that we have instantaneous interaction, i.e. the speed of light goes to infinity, such that we do not have any retardation. Accordingly, the Green function in this case reduces to the Green function of the Laplace equation

$$g(\mathbf{r}, \mathbf{r}') = \frac{e^{\pm ik|\mathbf{r}-\mathbf{r}'|}}{4\pi|\mathbf{r}-\mathbf{r}'|} \rightarrow g_L(\mathbf{r}, \mathbf{r}') = \frac{1}{4\pi|\mathbf{r}-\mathbf{r}'|}. \quad (2.33)$$

The applicability of the QSA can be checked once results including full retardation are available and we will be concerned with such a comparison in Sec. 6.3.1.

2.2 Plane Waves

In addition to the Fourier transform with respect to time we have used in Sec. 2.1.5, we can likewise introduce a Fourier transform with respect to space according to

$$f(\mathbf{r}) = \int d^3k f(\mathbf{k}) e^{i\mathbf{k}\cdot\mathbf{r}} \quad (2.34)$$

$$f(\mathbf{k}) = \frac{1}{(2\pi)^3} \int d^3r f(\mathbf{r}) e^{-i\mathbf{k}\cdot\mathbf{r}}. \quad (2.35)$$

2 Electrodynamics

Any electromagnetic field $\mathbf{E}(\mathbf{r}, t)$ can then be formed as a superposition of components of the form

$$\mathbf{E}_{\mathbf{k},\omega}(\mathbf{r}, t) = \mathbf{E}_0 e^{i\mathbf{k}\cdot\mathbf{r} - i\omega t} \quad (2.36)$$

with some constant vector \mathbf{E}_0 . Here, \mathbf{k} is the *wave vector*, which we have already introduced in Sec. 2.1.8. Electromagnetic waves of the form (2.36) are called *plane waves*, because for any given time t , the iso-phase surfaces are planes according to $\mathbf{k} \cdot \mathbf{r} - \omega t = \text{const.}$ Also, the planes of constant phase move at constant velocity in direction of \mathbf{k} .

In order to satisfy the wave equation, ω and \mathbf{k} cannot be chosen arbitrarily. Plugging in the ansatz (2.36) into the wave equation leads to the equation

$$\left(k^2 - \frac{\omega^2}{c^2}\right) \mathbf{E}_{\mathbf{k},\omega} = 0 \quad (2.37)$$

This equation is always satisfied if the bracket on the left-hand side vanishes. This leads to the important relation between the wave vector \mathbf{k} and the frequency ω . Noticing that the speed of light is $c^2 = (\varepsilon_0 \varepsilon \mu_0 \mu)^{-1}$ we see that

4 The wave vector \mathbf{k} and the frequency ω have to satisfy the dispersion relation

$$\omega^2 = \frac{k^2}{\varepsilon_0 \varepsilon(\mathbf{k}, \omega) \mu_0 \mu(\mathbf{k}, \omega)} = \frac{c_0^2}{n^2} k^2 \quad (2.38)$$

The dispersion relation as given above is quadratic in ω and \mathbf{k} . Usually, the square root is taken to obtain the linear photon dispersion in a medium of refractive index n

$$\omega = \frac{c_0}{n} |\mathbf{k}|. \quad (2.39)$$

The slope of the dispersion is exactly the phase velocity in the medium.

We see that if ε and μ happen to be both negative, the above equations are not altered. With this postulated, Veselago investigated the properties of materials having both $\varepsilon < 0, \mu < 0$ and showed that such - back then hypothetical - materials show effects like negative refraction and phase velocity [18]. While such materials have not been found in nature, they can be created artificially, as so-called metamaterials [11].

2.3 Scattering Theory

As we will carry out electromagnetic scattering calculations in this thesis, we will review the most important concepts and terms. In general, the term *scattering* refers to different physical techniques. Commonly, one uses some sort of probe that interacts with a target and from the change of the physical state of the probe one draws conclusion on the physical properties of the target. The probe might be particles, as e.g. used by Rutherford to examine the scattering of alpha particles from a thin gold foil, which lead to the nucleus-electron picture of the atoms [19]. We are going to consider metallic nanoparticles that are probed with beams of light. One can imagine that due to the interaction

2 Electrodynamics

with the particle, parts of the beam will be deflected from the original trajectory and in addition, parts of the electromagnetic energy will be absorbed by the particle. The deflected fields will be called *scattered fields* \mathbf{E}_{scat} , \mathbf{H}_{scat} and we will see that the amount of scattered energy as well as the angular distribution allows us to draw conclusions about the scatterer. To quantify electromagnetic energy we introduce the *Poynting vector*. It is given by

$$\mathbf{S}(\mathbf{r}, t) = \mathbf{E}(\mathbf{r}, t) \times \mathbf{H}(\mathbf{r}, t) \quad (2.40)$$

and can be interpreted as the density of energy flow at a point in space, it has the unit of energy per area. In experiments, one will usually measure the time average of the electromagnetic energy, which for time harmonic fields evaluates to

$$\langle \mathbf{S} \rangle = \frac{1}{2} \Re(\mathcal{E} \times \mathcal{H}^*). \quad (2.41)$$

With this, we can construct a virtual sphere Ω enclosing the scatterer as sketched in Fig. 2.3 and assume that the embedding medium is non-absorbing, i.e. $\Im \varepsilon_e = 0$ ¹. Then we can integrate the Poynting vector on Ω to get the net energy flow

$$W_a = - \int_{\Omega} \mathbf{S} \cdot d\mathbf{n}, \quad (2.42)$$

where \mathbf{n} is the outward normal to Ω . If $W_a > 0$, this means that we have a net inflow, i.e. energy is absorbed inside Ω and as we have assumed $\Im \varepsilon_e = 0$, the energy must be absorbed by the particle. The field in the exterior of the particle is a superposition of scattered and incident field, therefore the Poynting vector is given by

$$\begin{aligned} \mathbf{S} &= (\mathbf{E}_{inc} + \mathbf{E}_{scat}) \times (\mathbf{H}_{inc} + \mathbf{H}_{scat}) \\ &= \underbrace{\mathbf{E}_{inc} \times \mathbf{H}_{inc}}_{=\mathbf{S}_{inc}} + \underbrace{\mathbf{E}_{scat} \times \mathbf{H}_{scat}}_{=\mathbf{S}_{scat}} + \underbrace{\mathbf{E}_{inc} \times \mathbf{H}_{scat} + \mathbf{E}_{scat} \times \mathbf{H}_{inc}}_{=\mathbf{S}_{ext}} \end{aligned} \quad (2.43)$$

The latter term can be understood as an interaction between the incident and the scattered field and is termed *extinction*. We can now consider the contributions of the above components to the energy flow

$$W_a = W_{inc} - W_{scat} + W_{ext}. \quad (2.44)$$

The negative sign of W_{scat} is because the scattered field originates from inside the contour Ω . If the surrounding medium is non-absorbing, the incident field does not contribute, i.e. $W_{inc} = 0$. We therefore see that the extinction W_{ext} is nothing else then the absorbed plus the scattered energy $W_{ext} = W_a + W_{scat}$. For an incident plane wave we can now introduce the *extinction cross section* and the *scattering cross section*, relating

¹Here, we fix the notion used in the following. We denote the permittivity in the *interior* and *exterior* of the particle as ε_i and ε_e , respectively

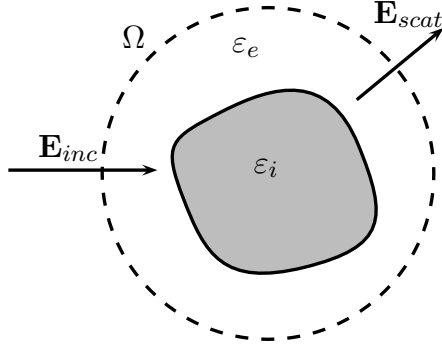


Figure 2.3: **Scattering of electromagnetic fields.** We assume an electromagnetic wave \mathbf{E}_{inc} that is incident on a scatterer which has the permittivity ε_i embedded in a medium with permittivity ε_e . The interaction of the incident field with the scatterer will give rise to a scattered field \mathbf{E}_{scat} . In a non-absorbing medium we can evaluate the energy balance on a virtual boundary Ω and determine the amount of scattered and absorbed electromagnetic energy as discussed in the text.

the respective energies to the incident field energy

$$C_{ext} = \frac{W_{ext}}{\frac{1}{2} \sqrt{\frac{\varepsilon_e}{\mu_e}} |\mathbf{E}_0|^2}, \quad (2.45)$$

$$C_{scat} = \frac{W_{scat}}{\frac{1}{2} \sqrt{\frac{\varepsilon_e}{\mu_e}} |\mathbf{E}_0|^2}. \quad (2.46)$$

Usually, the scattering and extinction cross-sections are normalized to the geometric cross-section of the scatterer A_s . This results in the *extinction and scattering efficiency*

$$Q_{ext} = \frac{C_{ext}}{A_s}, \quad (2.47)$$

$$Q_{scat} = \frac{C_{scat}}{A_s}. \quad (2.48)$$

Especially the extinction is a quantity accessible in experiments and will be used to establish the link between experiment and calculation in Chap. 4. Due to large laser spot-sizes, the extinction measured there is always an ensemble average. It is, however, even possible to measure the extinction of a single 200 nm gold particle in absolute units [20].

2.4 Optical Properties of Metals

As discussed in Sec. 2.1.1, the behaviour of materials in electric and magnetic fields is described by the permittivity ε and the permeability μ . One could say, that Maxwell outsourced the problem of describing the material response from his equations. For many materials a linear, non-dispersive response is a good approximation, however, this does not hold for metals. Their optical response is dominated by the conduction electrons that tend to follow an external electric field. Due to the finite (effective) mass of the electrons, we may expect the response to depend on the frequency of the external driving field. Using simple physical models, it is possible to find analytical expressions for the permittivity of a metal that show a good agreement with measurements of the permittivity from experiments.

2.4.1 Drude model - Permittivity of the free Electron Gas

We assume a homogeneous gas of electrons of number density n . The electrons of (effective) mass m are supposed to move freely against a fixed positive ion background. Under the influence of an external driving electric field $\mathbf{E}(t)$, the electrons are accelerated, while their motion is damped by collisions with the positive ions. The resulting equation of motion reads

$$m\ddot{\mathbf{x}}(t) + m\gamma\dot{\mathbf{x}}(t) = -e\mathbf{E}(t), \quad (2.49)$$

where the *collision frequency* γ is a measure for the damping. Electrons which are displaced against the positive background contribute to a macroscopic polarization $\mathbf{P}(t) = -nex(t)$, we therefore obtain the following differential equation for the polarization:

$$\ddot{\mathbf{P}}(t) + \gamma\dot{\mathbf{P}}(t) = \frac{ne^2}{m}\mathbf{E}(t). \quad (2.50)$$

By introducing the Fourier transforms of \mathbf{P} and \mathbf{E} in the above equation, we obtain the relationship between the Fourier components and obtain an explicit expression for \mathcal{P}

$$\mathcal{P} = -\frac{ne^2/m}{\omega^2 + i\gamma\omega}\mathcal{E}. \quad (2.51)$$

Together with $\mathcal{D} = \varepsilon_0\mathcal{E} + \mathcal{P}$, we have obtained

$$\mathcal{D} = \varepsilon_0 \left(1 - \frac{\omega_p^2}{\omega^2 + i\gamma\omega} \right) \mathcal{E}, \quad (2.52)$$

where we have introduced the *plasma frequency* $\omega_p^2 = \frac{ne^2}{\varepsilon_0 m}$. We see that there is a correspondence between a frequency-dependent permittivity and the polarization:

5 *If given by an analytical expression as above, a frequency-dependent permittivity can be expressed as a differential equation for the polarization $\mathbf{P}(t)$.*

2 Electrodynamics

This enables us to efficiently treat temporally disperse materials in time-domain calculations by solving Eq. (2.50) simultaneously with Maxwell's equations. This approach is called Auxiliary Differential Equations (ADE) method.

An alternative derivation for the Drude permittivity may be obtained by using Ohm's law

$$\mathcal{J} = \sigma(\omega) \mathcal{E}, \quad (2.53)$$

which states that an electric field causes a current parallel to the field with amplitude determined by the *conductivity* $\sigma(\omega)$. According to the Drude model (cf. [21]) the conductivity of a metal is given by

$$\sigma(\omega) = \frac{\sigma_0}{1 - i\omega\tau} \quad \text{with } \sigma_0 = \frac{ne^2\tau}{m} \quad (2.54)$$

where the *relaxation time* τ is the mean time between collision of the electrons with the positive ions. Together with Eq. (2.18b) we obtain

$$\begin{aligned} \nabla \times \mathcal{H} &= -i\omega\mathcal{D} + \mathcal{J} = -i\omega\varepsilon_0\mathcal{E} + \sigma(\omega)\mathcal{E} = -i\omega\varepsilon_0\mathcal{E} + \frac{ne^2\tau/m}{1 - i\omega\tau}\mathcal{E} \\ &= -i\omega\varepsilon_0 \left(1 - \frac{ne^2/(m\varepsilon_0)}{\omega^2 + i\omega\gamma} \right) \mathcal{E} = -i\omega\varepsilon_0 \left(1 - \frac{\omega_p^2}{\omega^2 + i\omega\gamma} \right) \mathcal{E} \end{aligned}$$

where we have used the collision frequency $\gamma = 1/\tau$. Again, we arrive at the Drude expression for the permittivity as in Eq. (2.52). This approach is redundant in the sense that the expression for $\sigma(\omega)$ is obtained by reasoning similar to above, where we have considered the free electron gas. However, an important consequence is that

6 *The description of the optical response of any material can be achieved by supplementing Maxwell's equations with an appropriate model for the current \mathbf{J} .*

2.4.2 Lorentz Model

The Drude model assumed a free electron gas. In addition, bound electrons might as well contribute to the response of a metal and can be taken into account by an additional restoring force in the equation of motion for the electrons. This results in

$$\ddot{\mathbf{P}}(t) + \gamma\dot{\mathbf{P}}(t) + \beta\mathbf{P}(t) = \frac{ne^2}{m}\mathbf{E}(t). \quad (2.55)$$

By the same reasoning as in the preceding section, we arrive at the *Lorentz model for the frequency-dependent permittivity*

$$\varepsilon(\omega) = 1 + \frac{\omega_L^2}{\omega_L^2 - i\gamma_L\omega - \omega^2} \quad (2.56)$$

Due to the linearity of Maxwell's equations, we are free to assume the response of the metal to be a linear combination of several Drude and Lorentz contributions. The

coefficients are usually chosen to yield a good approximation of measured datasets, which we will discuss in the next section.

2.4.3 Permittivity Measurements

Johnson and Christy [22] performed measurements on thin films of gold, silver and copper. From transmission and reflectance measurements they determine the permittivity. For gold and silver, the results are shown in Fig. 2.4. The measured data reveal an important characteristic of metals: The real part of the permittivity can be negative for certain wavelengths. Also, in the infrared part of the spectrum the absolute value of the real part can be as high as 150 and more.

Concerning the imaginary part of the permittivity, we see the onset of inter-band transitions for both noble metals. For gold this onset falls into the visible part of the electromagnetic spectrum around 500 nm wavelength. For silver we observe the rise in the imaginary part for shorter wavelengths around 300 nm, thus outside the visible part of the electromagnetic spectrum. Even though these measurements have been

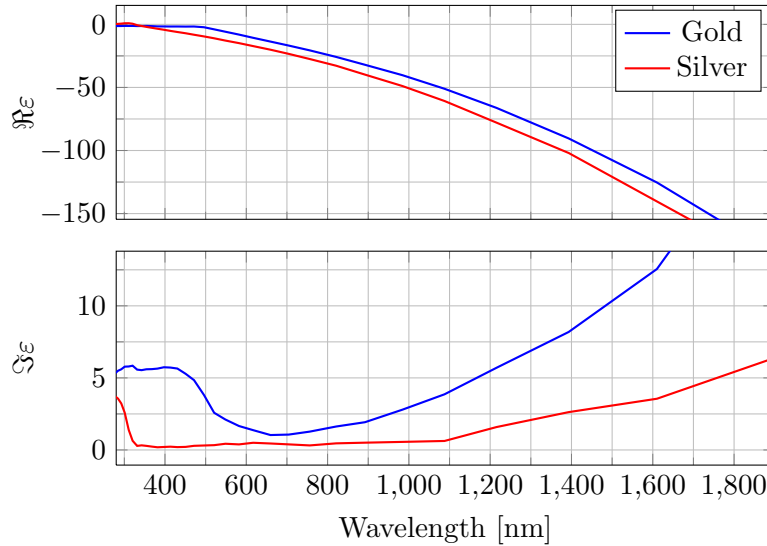


Figure 2.4: Measured data for the real (top) and imaginary (bottom) part of the permittivities of gold and silver as a function of the wavelength [22].

performed on films with 20 nm to 50 nm thickness, it has become customary to use these datasets for calculations involving nanometer-sized particles of, e.g., spherical shape. It is not obvious that the permittivity measured at thin films is applicable here, however, simulations involving the permittivity dataset show good agreement with experiments. It is desirable to have an approximation of the permittivity for the noble metals in terms of a Drude model for the use in time-domain calculations using the ADE method. Figure 2.5 shows a comparison of the permittivity data measured by Johnson and Christy [22] and a Drude model with parameters chosen to fit the measured data given in Tab. 2.1. The

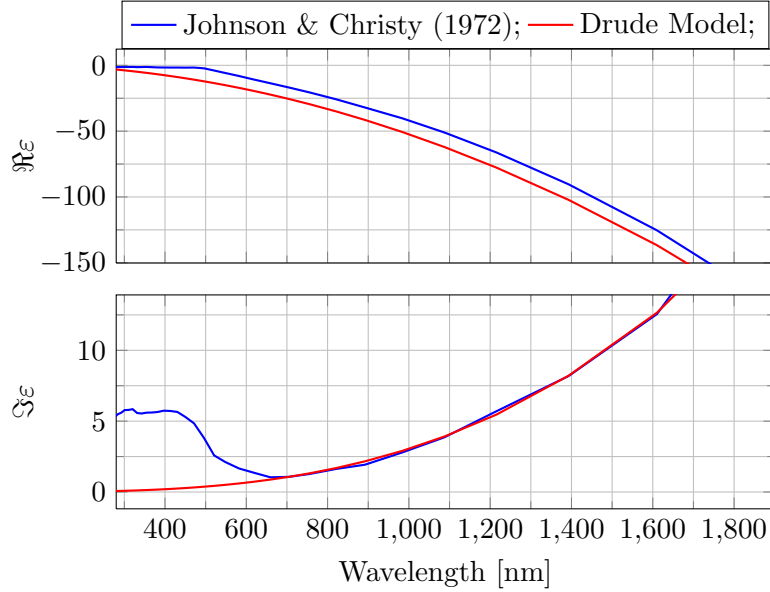


Figure 2.5: Comparison of the real and imaginary parts of the permittivity. The blue curves shows the measured data by Johnson and Christy [22] and the red curves are a Drude model with parameters chosen to approximate the measured data (cf. Tab. 2.1). While the agreement is good over a wide wavelength range, we see that the inter-band transitions below 500 nm are not taken into account by the Drude model.

overall agreement can be considered good over a wide range of wavelengths. The inter-band transitions that occur for gold below 500 nm and contribute to the imaginary part of the permittivity, however, are not taken into account by the Drude model. Therefore, we see clear deviations between the two permittivities below 500 nm. To take the inter-band transitions into account, we have to add a Lorentz-term to the permittivity. Again, the parameters are given in Tab. 2.1.

2.4.4 Permittivities used in this Thesis

For the calculations in this thesis, we will restrict ourselves to either experimental data or simple Drude or Lorentz models. The reason for this is two-fold. First, we will often be concerned with numerical methods and aim to see how accurate the numerical results are. Here, a well behaved analytical permittivity like a Drude model is more desirable because it results in well behaved spectra. Furthermore comparing the results of a time domain and a frequency domain method restricts us to such analytical permittivities as explained above. The second reason is, that using the Drude-Lorentz model given in Tab. 2.1, we see an excellent agreement between numerical results and experiments, the comparison of which will be shown in Sec. 7.7. Table 2.1 lists the permittivities that we will use in our calculations. Gold and silver are the favorite materials for plasmonic

Material	Source	Parameters (if applicable) (eV)
Gold	Experiment	Taken from [22]
Silver	Experiment	Taken from [23]
Gold	Drude	$\hbar\omega_p = 9.073, \hbar\gamma = 0.071$
Gold	Drude	$\hbar\omega_p = 8.794, \hbar\gamma_p = 0.066$
	+Lorentz	$\hbar\omega_L = 2.646, \hbar\gamma_L = 0.382$
Aluminum	Drude	$\hbar\omega_p = 15, \hbar\gamma_p = 0.6$

Table 2.1: Permittivity models used in this thesis.

nano-particles because their resonances are located around the visible wavelength range. In contrast to gold and silver, aluminum is a metal that is well described by a Drude model over a huge frequency range. While for the studies shown in this thesis the Drude and Lorentz model give good results, the applicability of these models is subject to an ongoing debate and effort towards more sophisticated description of the optical properties of metallic nano-particles exists. In the following we will shortly discuss the approaches for the sake of completeness.

2.4.5 Advanced Models

The Drude and Lorentz models were derived under simple assumptions about the electron dynamics. Nevertheless they show a good agreement with experiments and are the common choice to describe most experiments. However, with structures of nanometer sizes, that are available due to micro fabrication, one might expect that the naive classical picture has to be replaced by a quantum mechanical one or at least be supplemented with a semi-classical one. Concerning the Drude model, it was derived under the assumption that the mean time between electron-ion-collisions is the relaxation time τ . Assuming that the electrons propagate with the Fermi-velocity v_f , we are able to calculate the mean free path length. This length turns out to be in the order of 10 nm, which is in the order of the particle sizes. Thus, the conduction electrons might be scattered at the particle surface, which decreases the relaxation time τ and thus increases damping. A phenomenological extension of the Drude model is to include an additional damping term to take this effect into account.

Non-locality

As already mentioned in Sec. 2.1.1, electronic transport in a material can render the electromagnetic response non-local. Obviously, this could apply for metals, especially as the mean free path is in the order of 10 nm. In Fourier space, a spatially non-local permittivity is determined by a \mathbf{k} -dependent permittivity analogous to a temporally non-local permittivity leads to a frequency-dependent permittivity. A non-local correction to the permittivity was proposed by Mermin [24]. Recently, García de Abajo studied the influence of non-locality on the scattering cross-section of a dimer of 10 nm gold sphere

and showed that for distances larger than 1 nm influences are marginal [25]. Also recent experiments suggest that the local classical electrodynamic description is even valid for a dimer of nano-rods with only 1 nm distance².

Hydrodynamic Model

Another step towards an advanced description of the electromagnetic response of metallic nano-particles is the description of the particle's electrons as a fluid. Let ρ and \mathbf{j} be the particle density and the particle current, respectively. Then, the dynamics of the fluid is described by the Euler equations expressing the conservation of momentum

$$\frac{\partial \mathbf{j}}{\partial t} + \nabla \cdot \left(\frac{1}{\rho} \mathbf{j} \circ \mathbf{j} \right) = \frac{1}{m} (\mathbf{F}_{Lorentz} - \nabla p). \quad (2.57)$$

The hydrodynamic model can be mapped to a Drude model fixing all parameters except the pressure p . One choice for the pressure is the of a degenerate electron gas, the Thomas-Fermi pressure

$$p = \frac{(2\pi^2)^{2/3} \hbar^2}{5m} \rho^{5/3} \quad (2.58)$$

In addition, one has to determine the boundary conditions on the particle interface. Choices are the so-called no-slip boundaries where the particle current vanishes on the particle surface and the slip boundaries. Here, the normal component vanishes on the surface. The hydrodynamic model shows new effects for certain geometries. For example, shifts of the resonances have been observed for sphere dimers with small separations [26]. There are also linearized hydrodynamic approaches which can be solved in frequency-domain [27].

2.5 Plasmonics — Electrodynamics with Metals

In Sec. 2.4 we have seen, that the permittivity of metals can be negative in certain frequency ranges. This special property gives rise to a new kind of electromagnetic wave. These waves are called *Surface Plasmon Polaritons (SPP)* or, shorter, *surface plasmons*. We will start by considering a planar metal-insulator interface and then discuss the electromagnetic properties of metallic particles.

2.5.1 Surface Plasmon Polaritons at planar Interfaces

We postulate the existence of waves that are confined to a planar material interface and decay exponentially with increasing distance from the interface. Let the interface coincide with the x - y -plane and, without loss of generality, let the wave propagate in

²arXiv:1112.5008v1

2 Electrodynamics

x -direction with a wave vector component $k_x = \beta$. We denote the permittivity by

$$\varepsilon(z) = \begin{cases} \varepsilon_1 & z < 0 \\ \varepsilon_2 & z > 0 \end{cases} \quad (2.59)$$

Then we choose the following ansatz for the fields for $z > 0$

$$H_y(z) = A_2 e^{i\beta x} e^{-k_2 z} \quad (2.60a)$$

$$E_x(z) = iA_2 \frac{1}{\omega \varepsilon_0 \varepsilon_2} k_2 e^{i\beta x} e^{-k_2 z} \quad (2.60b)$$

$$E_z(z) = -A_2 \frac{\beta}{\omega \varepsilon_0 \varepsilon_2} e^{i\beta x} e^{-k_2 z} \quad (2.60c)$$

and for $z < 0$ we have

$$H_y(z) = A_1 e^{i\beta x} e^{k_1 z} \quad (2.61a)$$

$$E_x(z) = iA_1 \frac{1}{\omega \varepsilon_0 \varepsilon_1} k_1 e^{i\beta x} e^{k_1 z} \quad (2.61b)$$

$$E_z(z) = -A_1 \frac{\beta}{\omega \varepsilon_0 \varepsilon_1} e^{i\beta x} e^{k_1 z} \quad (2.61c)$$

Now we can use the boundary conditions (2.13) at the interface to obtain the conditions under which the above ansatz is a solution of Maxwell's equations, i.e.

$$A_1 = A_2 \quad (2.62a)$$

$$\frac{k_2}{k_1} = -\frac{\varepsilon_2}{\varepsilon_1} \quad (2.62b)$$

According to the above equations, $k_1 > 0$ and $k_2 > 0$ and therefore, we have the condition $\Re \varepsilon_1 < 0$ for $\varepsilon_2 > 0$. If we assume a metal-insulator interface, we see that this condition can be fulfilled in certain frequency ranges as the permittivity of the metal ε_1 can be negative. These waves sustained by metal-insulator interfaces are called surface plasmon polariton (SPP).

Figure 2.6 shows the norm of the electric field at a metal-insulator interface. We see that the electric field is confined to the surface. The decay length of the field depends on the material properties, however it is usually much shorter than the free-space wavelength at the respective frequency. This localization of the electromagnetic energy has paved the way for a lot of interesting applications, which we will discuss in the next section.

As plane waves in the preceding section, SPPs can be characterized by a dispersion relation.

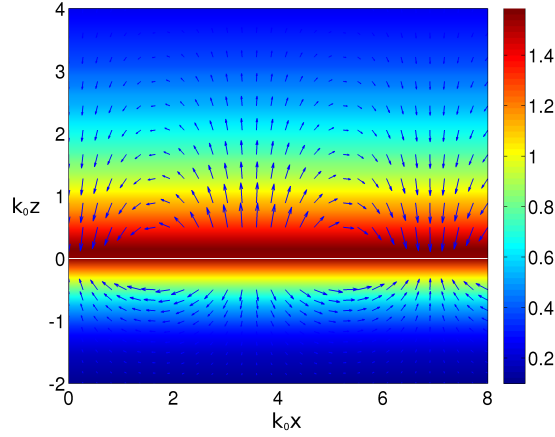


Figure 2.6: Color encoded norm and vector plot of the electric field at a metal-insulator interface. The metal is assumed to be a loss-less Drude metal.

7 The dispersion relation for surface plasmon polaritons is given by

$$\beta = k_0 \sqrt{\frac{\varepsilon_1(\omega) \varepsilon_2}{\varepsilon_1(\omega) + \varepsilon_2}} \quad (2.63)$$

where β is the component of the wave vector parallel to the interface and $k_0 = \omega/c$.

We plot the dispersion relation for two different metal-insulator interfaces in Fig. 2.7. We assume a Drude model for the metal permittivity and neglect losses, i.e. we set $\gamma = 0$. For the insulator we choose air (blue curves, $\varepsilon_2 = 1$) and glass (red curves, $\varepsilon_2 = 2.25$). In addition we plot the light-lines, i.e. the free photon dispersion, in the respective insulator as dotted lines. Solid lines correspond to the real part of the wave vector, dashed lines to the imaginary part. The solid lines below the light lines correspond to the bound surface plasmon polaritons. For frequencies above the plasma frequency ω_p , the real part of the permittivity of the metal becomes positive and no such bound modes exist. Therefore, the solid lines above the light line indicate propagating radiation. Between the two bands we have a region where the wave vector is purely imaginary prohibiting SPP propagation.

For frequencies approaching the *surface plasmon frequency*

$$\omega_{sp} = \frac{\omega_p}{\sqrt{1 + \varepsilon_2}} \quad (2.64)$$

the wave vector diverges. This situation corresponds to a coherent oscillation of the electrons where the group velocity v_g goes to zero. Strictly speaking, this mode is called Surface Plasmon (SP), a special case of the propagating surface plasmon polariton. It has, however, become customary to neglect this distinction and in general refer to both kinds of waves as *surface plasmons*.

The dispersion relation reveals another important characteristic of SPPs. Because their dispersion does not intersect with the light-line, SPPs cannot be directly excited with light in form of plane waves. Techniques like gratings or prism coupling have to be used in such cases [9].

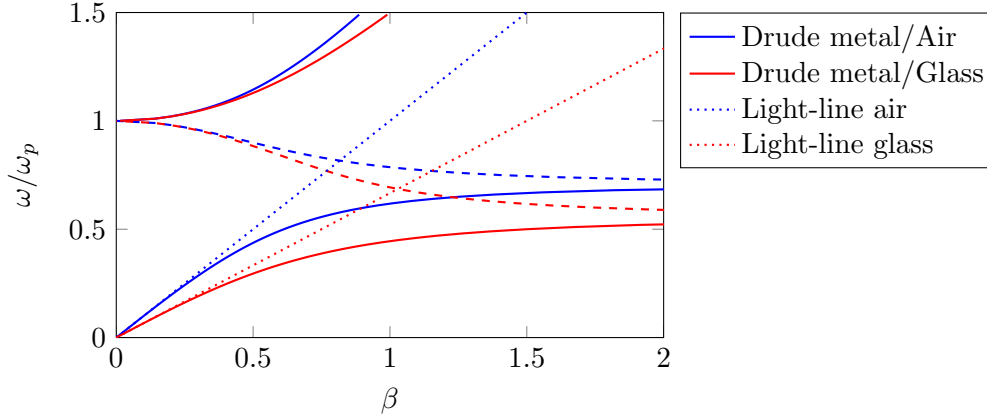


Figure 2.7: Dispersion of the Surface Plasmon Polariton (SPP). The blue curves show the SPP sustained by an infinite Drude metal-air interface, the red curves indicate the dispersion relation for a SPP at an Drude metal-glass interface. Losses are neglected here. The dotted lines are the free photon dispersion relations in vacuum (blue) and glass (red), respectively.

2.5.2 Localized Surface Plasmon Polaritons

After considering a plane metal-insulator interface, we now want to discuss another form of such an interface. As sketched in figure 2.8, a particle can also be considered as metal-insulator interface and we may expect it to also support surface plasmons. We will see that it indeed does and as these are bound to the particle, they are termed Localized Surface Plasmons (LSP) or *Particle Plasmons*. In contrast to the SPP at planar inter-

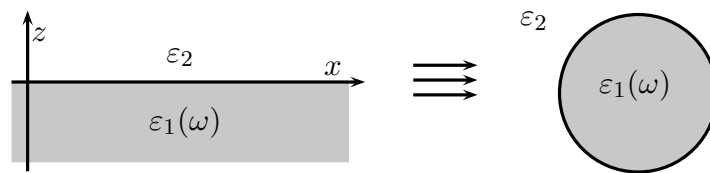


Figure 2.8: A particle regarded as metal-dielectric interface.

faces, LSPs can be excited with light. Figure 2.9 shows the electric field at a 10 nm sphere excited with a plane wave at the dipole resonance around 355 nm. The LSP has two interesting properties. First, as for the SPP, the LSP field is confined to the surface of the particle. The decay length of the field is much shorter than the free-space

2 Electrodynamics

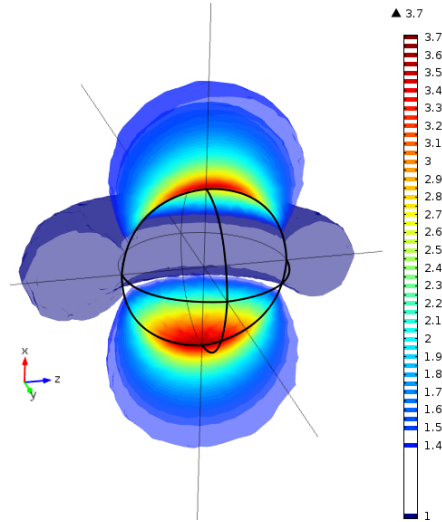


Figure 2.9: Cross-section through an iso-surface plot of the norm of the electric field at a 10 nm silver sphere with on-resonance irradiation. The incident plane wave is polarized along the x -axis and propagates along the z direction. Field amplitudes are normalized to the incident field amplitude. We see that the electric field is localized at the poles of the sphere and that the field values in the vicinity of the poles are up to four times larger than the incident field amplitude. These are two characteristics of Localized Surface Plasmons.

wavelength at the respective frequency. Thus, the electromagnetic energy is localized to sub-wavelength regions, which would not be possible with conventional diffraction-limited optics. The second important property is the so-called field-enhancement. When excited near the LSP resonance, the amplitude of the electric field at the particle surface can be larger than the amplitude of the incident field. Thus, LSP facilitate a very localized, very intense electric field. These characteristics have been exploited for a variety of applications. The strong confinement can be used to build waveguides from individual particles that are much smaller than conventional photonic waveguides. The latter ones usually require lateral dimension in the order of half a wavelength. Plasmonic waveguides [28, 29] require only a fraction of this. As typical electronic integrated circuits, such as the central processing unit of computers, have similar dimensions, interfacing electronics and plasmonics could yield faster processing technologies [3]. The LSP resonances are very sensitive to changes in their environment. This makes them suited to act as sensors [30, 4], which can be even used for virus-detection [31]. The field-enhancements have been used to enhance non-linear properties [32, 33].

With all these applications, understanding and tailoring the plasmonic properties of metallic nano-particles has become a major aim of plasmonics. To that end, both numerical and experimental methods have been developed and we will now continue to discuss numerical methods to calculate the plasmonic properties of metallic nano-particles.

3 Numerical Methods

In this chapter, we will introduce the numerical methods used in this thesis. Our focus will be on the solution of the scattering problem and we choose the scatterer to be a single metallic nano-particle - *the drosophila of plasmonics*, as W.L. Barnes put it [34]. For any given incident field and given scatterer, we have to calculate the scattered field using Maxwell's Equations. We assume that the scatterer has the permittivity and permeability ε_i, μ_i and the surrounding medium ε_e, μ_e , where the indices stand for *interior* and *exterior*, respectively. The situation is sketched in Fig. 3.1.

For spherical particles, the scattering problem is amenable to an analytical solution as shown in Sec. 3.1. More general particle shapes usually require other methods that approximate the exact solution. The methods are either based on the time-dependent

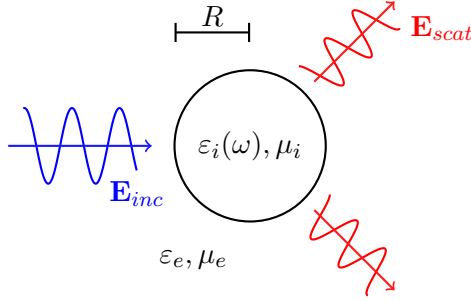


Figure 3.1: Sketch of the test scattering problem. The scatterer is a sphere of radius R situated at the origin with a frequency dependent permittivity $\varepsilon_i(\omega)$. For a given incident field \mathbf{E}_{inc} , we want to find the scattered field \mathbf{E}_{scat} that is caused by the interaction between the scatterer and the incident field.

Maxwell Equations (2.1) or the frequency-dependent Maxwell Equations (2.18), and hence termed *time-domain (TD)* and *frequency-domain (FD) methods*, respectively. For FD methods, we have to solve for the Fourier coefficients of the fields for every given frequency ω . Therefore, it is straight-forward to use experimentally measured values for the permittivity $\varepsilon(\omega)$. In contrast to that, taking these values into account in TD methods, would require the convolution of the time-dependent permittivity with the electric field as in Eq. (2.8), which would lead to prohibitive memory and computation time demands. However, we have seen in Sec. 2.4, that we can express a frequency-dependent permittivity by differential equations for the polarization, as long as they have a functional form as the Drude or Lorentz model or a linear combination of several terms. This is the usual way of treating a frequency dependent permittivity in TD codes

and it can also be used to fit a superposition of Drude-Lorentz terms to experimental datasets.

3.1 Mie Theory

The analytical solution of the electrodynamic scattering problem for spherical particles was solved by Gustav Mie [2] and is usually called Mie Theory or Lorenz-Mie Theory. It is a FD method based on the solution of the vector Helmholtz Equation (2.24) in spherical coordinates. The solutions can be generated from those of the scalar Helmholtz equation and we will first introduce the necessary functions before proceeding to the solution of the actual scattering problem. The discussion follows the one given by Bohren and Huffman [35], augmented by details discussed in the book by Stratton [36].

3.1.1 Scalar Wave Functions

The scalar wave functions (SWF), i.e. the solutions of the scalar Helmholtz equation, in spherical coordinates can be determined by the separation ansatz

$$\psi(r, \vartheta, \varphi) = R(r)\Theta(\vartheta)\Phi(\varphi). \quad (3.1)$$

Substituting the Laplacian in spherical coordinates

$$\Delta = \frac{1}{r^2} \frac{\partial}{\partial r} \left(r^2 \frac{\partial}{\partial r} \right) + \frac{1}{r^2 \sin \vartheta} \frac{\partial}{\partial \vartheta} \left(\sin \vartheta \frac{\partial}{\partial \vartheta} \right) + \frac{1}{r^2 \sin^2 \vartheta} \frac{\partial^2}{\partial \varphi^2} \quad (3.2)$$

in (2.24) and using the above separation ansatz, we arrive at differential equations for each factor.

Radial Part

For the radial part $R(r)$, we arrive at the following differential equation:

$$\frac{d}{dr} \left(r^2 \frac{dR}{dr} \right) + [k^2 r^2 - n(n+1)] R = 0 \quad (3.3)$$

Introducing the dimensionless variable $\rho = kr$ and substituting $Z = R\sqrt{\rho}$ we arrive at the Bessel Differential Equation

$$\rho \frac{d}{d\rho} \left(\rho \frac{dZ}{d\rho} \right) + \left[\rho^2 - \left(n + \frac{1}{2} \right)^2 \right] Z = 0, \quad (3.4)$$

3 Numerical Methods

the solutions of which are the Bessel functions of first kind J_ν and second kind Y_ν with the order $\nu = n + \frac{1}{2}$. Defining the *spherical Bessel functions* as

$$j_n(\rho) = \sqrt{\frac{\pi}{2\rho}} J_{n+1/2}(\rho) \quad (3.5)$$

$$y_n(\rho) = \sqrt{\frac{\pi}{2\rho}} Y_{n+1/2}(\rho) \quad (3.6)$$

we see that they are exactly the solutions for the radial part. While $j_n(\rho)$ is finite at the origin, the $y_n(\rho)$ diverge for $\rho \rightarrow 0$. This will be of importance when considering the expansions of the incident and scattered electric field later on.

The linear combinations

$$h^{(1)}(\rho) = j_n(\rho) + iy_n(\rho) \quad (3.7)$$

$$h^{(2)}(\rho) = j_n(\rho) - iy_n(\rho) \quad (3.8)$$

are called *spherical Hankel functions* of the first and second kind, respectively and are another linearly independent set of solutions of the Bessel equation. Their asymptotic expressions for $\rho \rightarrow \infty$ resemble those of incoming and outgoing waves, respectively, and therefore they are important in scattering theory.

Angular Part

For the φ -dependent factor of the angular part, we arrive at the differential equation

$$\frac{d^2\Phi}{d\varphi^2} + m^2\Phi = 0, \quad (3.9)$$

the solution of which is given by the phase factor $\Phi(\varphi) = e^{im\varphi}$. The ϑ -dependent parts leads to the more complicated equation

$$\frac{1}{\sin\vartheta} \frac{d}{d\vartheta} \left(\sin\vartheta \frac{d\Theta}{d\vartheta} \right) + \left[n(n+1) - \frac{m^2}{\sin^2\vartheta} \right] \Theta = 0. \quad (3.10)$$

The solution of this differential equation are the *associated Legendre Polynomials* P_n^m of order m and n . Together with $\Phi(\varphi)$ they form the well known *Spherical Harmonics*

$$Y_n^m(\vartheta, \varphi) = \Theta(\vartheta)\Phi(\varphi) = \alpha_{m,n} P_n^m(\cos\vartheta) e^{im\varphi}. \quad (3.11)$$

The definition of the normalization factor $\alpha_{m,n}$ differs in the literature. Unless mentioned otherwise, we use the basis given by Doicu *et al.* [37].

From Eqns. (3.9) and (3.10) we see that the spherical harmonics are the eigenfunctions of the angular part of the Laplacian (3.2). Further eigenvalue equations can be derived for the *angular momentum operator* $\hat{\mathbf{L}} = -i\mathbf{r} \times \nabla$. The spherical harmonics are the

3 Numerical Methods

eigenfunctions of the squared operator and the z -component

$$\hat{\mathbf{L}}^2 Y_n^m = n(n+1)Y_n^m, \quad (3.12a)$$

$$\hat{L}_z Y_n^m = mY_n^m. \quad (3.12b)$$

Finally, the radial part together with the angular part form the scalar wave functions.

8 The scalar wave functions (SWF), which are solutions of the scalar Helmholtz equation are given by

$$u_{mn}^{1,3}(k, \mathbf{r}) = z_n^{1,3}(kr)Y_{mn}(\vartheta, \varphi), \quad (3.13)$$

where $z_n^1 = j_n$ and $z_n^3 = h_n^{(1)}$.

Accordingly, u_n^1 is called *regular SWF* and u_n^3 is called *propagating SWF*. As the angular momentum operator $\hat{\mathbf{L}}$ only operates on the angular part, the eigenvalue equations (3.12) also hold for the SWF. In Sec. 6.1 we will see that using the angular momentum operator formalism simplifies calculations involving the wave functions.

3.1.2 Vector Wave Functions

The solutions of the vector Helmholtz equation (2.24) can be generated from solutions of the scalar Helmholtz equation. Let ψ be a solution of the scalar Helmholtz Equation. Then we define

$$\mathcal{L} = \nabla\psi \quad (3.14)$$

$$\mathcal{M} = \nabla \times (\mathbf{a}\psi) \quad (3.15)$$

$$\mathcal{N} = \frac{1}{k}\nabla \times \mathcal{M} \quad (3.16)$$

where \mathbf{a} is a constant vector of unit length. All of the three vector functions above, which we call Vector Wave Functions (VWF), satisfy the vector Helmholtz Equation (2.24) and, in addition, have the following properties

$$\begin{aligned} \nabla \cdot \mathcal{L} &= -k^2\psi & \nabla \cdot \mathcal{M} &= 0 & \nabla \cdot \mathcal{N} &= 0 \\ \nabla \times \mathcal{L} &= 0 & \nabla \times \mathcal{M} &= k\mathcal{N} & \nabla \times \mathcal{N} &= k\mathcal{M} \end{aligned}$$

i.e. \mathcal{M}, \mathcal{N} are solenoidal, while \mathcal{L} is purely longitudinal.

For each solution of the scalar Helmholtz equation $\psi = u_{mn}^i, i = 1, 3$, we can construct corresponding VWF that we denote with $\mathcal{L}_{mn}^i, \mathcal{M}_{mn}^i, \mathcal{N}_{mn}^i$. We see that the functions $\mathcal{M}_{mn}^i, \mathcal{N}_{mn}^i$ are appropriate for the representation of the electric and magnetic field \mathcal{E}, \mathcal{H} , as they are solenoidal and proportional to the curl of each other. Indeed, the discussion of the VWF is often limited to these two, for example in the book of Bohren and Huffman [35], because the usual scattering problem involves no free charges. However, the representation of a vector function with non-vanishing divergence requires the inclusion of \mathcal{L}_n .

3 Numerical Methods

In the discussion above, we limited the choice of the vector \mathbf{a} to a constant one of unit length. In the case of spherical coordinates, however, choosing $\mathbf{a} = \mathbf{r}$ yields independent solutions as well with the advantage of being tangential or normal over the entire surface of a sphere of given radius [36]. In the basis used by Doicu *et al.* [37], this results in the explicit expressions for the Spherical Vector Wave Functions (SVWF)

$$\mathcal{M}_{nm}^{1,3}(\mathbf{kr}) = \frac{1}{\sqrt{2n(n+1)}} \nabla u_{nm}^{1,3}(\mathbf{kr}) \times \mathbf{r}, \quad (3.17)$$

$$\mathcal{N}_{nm}^{1,3}(\mathbf{kr}) = \frac{1}{k} \nabla \times \mathcal{M}_{nm}^{1,3}(\mathbf{kr}), \quad (3.18)$$

$$u_{nm}^{1,3}(\mathbf{kr}) = z_{nm}^{1,3}(kr) P_n^{(|m|)}(\cos \theta) e^{jm\phi}, \quad (3.19)$$

$$z_{nm}^{1,3}(kr) = \begin{cases} j_n(kr) & \text{for } z_n^1(kr) \\ h_n^{(1)}(kr) & \text{for } z_n^3(kr) \end{cases}, \quad (3.20)$$

$$P_n^m(\cos \theta) = \sqrt{\frac{2n+1}{2} \frac{(n-m)!}{(n+m)!}} \hat{P}_n^m(\cos \theta), \quad (3.21)$$

$$\hat{P}_n^m(x) = \frac{1}{2^n n!} (1-x)^{\frac{m}{2}} \frac{\partial^{n+m}}{\partial x^{n+m}} (x^2-1)^n, \quad (3.22)$$

An elegant way of dealing with the SVWFs is the use of the angular momentum operator $\hat{\mathbf{L}}$ we have already introduced above. With this, we can write

$$\mathcal{M}_{nm}^{1,3}(\mathbf{kr}) = \frac{i}{\sqrt{2n(n+1)}} \hat{\mathbf{L}} u_{nm}^{1,3}(\mathbf{kr}), \quad (3.23)$$

$$\mathcal{N}_{nm}^{1,3}(\mathbf{kr}) = \frac{i}{k\sqrt{2n(n+1)}} \nabla \times \hat{\mathbf{L}} u_{nm}^{1,3}(\mathbf{kr}). \quad (3.24)$$

Thus, the angular momentum operator generates the SVWF from the scalar wave functions.

3.1.3 Field Expansion

Having the mathematical tools at hand, we are now able to represent the electric field as a linear combination of SVWFs. Neglecting the longitudinal modes \mathcal{L} , we obtain:

$$\mathcal{E} = \sum_{n=1}^{\infty} \sum_{m=-n}^n a_{mn} \mathcal{M}_{mn}^1 + b_{mn} \mathcal{N}_{mn}^1 + f_{mn} \mathcal{M}_{mn}^3 + g_{mn} \mathcal{N}_{mn}^3 \quad (3.25)$$

If the field \mathcal{E} is finite at the origin, the coefficients f_{mn} and g_{mn} must be zero, because \mathcal{M}_{mn}^3 and \mathcal{N}_{mn}^3 contain the Bessel functions of second kind $y_n(\rho)$ that diverge at the origin. Therefore, the incident field \mathcal{E}_{inc} must have an expansion of the form

$$\mathcal{E}_{inc} = \sum_{n=1}^{\infty} \sum_{m=-n}^n a_{mn} \mathcal{M}_{mn}^1 + b_{mn} \mathcal{N}_{mn}^1. \quad (3.26)$$

3 Numerical Methods

The same holds for the electric field inside the scatterer

$$\mathcal{E}_{int} = \sum_{n=1}^{\infty} \sum_{m=-n}^n c_{mn} \mathcal{M}_{mn}^1 + d_{mn} \mathcal{N}_{mn}^1. \quad (3.27)$$

The scattered field, in contrast, can be assumed to consist of outgoing waves in large distance from the scatterer. Due to the asymptotic expressions of $h_n^{(1)}$, the expansion must have the form

$$\mathcal{E}_{scat} = \sum_{n=1}^{\infty} \sum_{m=-n}^n f_{mn} \mathcal{M}_{mn}^3 + g_{mn} \mathcal{N}_{mn}^3. \quad (3.28)$$

The expansion of the magnetic field can be calculated from the electric field according to Eq. (2.18d)

$$\mathcal{H} = -\frac{i}{\omega\mu} \nabla \times \mathcal{E} \quad (3.29a)$$

$$= -\frac{i}{\omega\mu} \sum_{n=1}^{\infty} \sum_{m=-n}^n a_{mn} \nabla \times \mathcal{M}_{mn} + b_{mn} \nabla \times \mathcal{N}_{mn} \quad (3.29b)$$

$$= -\frac{ik}{\omega\mu} \sum_{n=1}^{\infty} \sum_{m=-n}^n a_{mn} \mathcal{N}_{mn} + b_{mn} \mathcal{M}_{mn}. \quad (3.29c)$$

3.1.4 Solution of the Scattering Problem

The task now is to calculate the scattered field for a given incident field. Usually, the incident field is given by a plane wave, a Gaussian beam or, in the case of Electron Energy Loss Spectroscopy discussed in Chap. 5, the field caused by a moving electron. At any rate, we assume that we can expand the incident field in terms of the SVWF as in Eq. (3.26) with known expansion coefficients a_{mn}, b_{mn} . We then calculate the expansion coefficients of the scattered field f_{mn}, g_{mn} with the help of the internal field \mathcal{E}_{int} by enforcing the boundary conditions at the scatterer surface. In the spherical case, it coincides with the iso-coordinate surface $S = \{(r, \vartheta, \varphi) : r = R\}$, which simplifies the analysis. The field outside the scatterer is given by $\mathcal{E}_{inc} + \mathcal{E}_{scat}$, while inside the scatterer we only have \mathcal{E}_{int} . The boundary conditions (2.13) on the surface S for the tangential components of the fields read

$$\mathbf{e}_r \times (\mathcal{E}_{inc} + \mathcal{E}_{scat}) = \mathbf{e}_r \times \mathcal{E}_{int} \quad (3.30)$$

$$\mathbf{e}_r \times (\mathcal{H}_{inc} + \mathcal{H}_{scat}) = \mathbf{e}_r \times \mathcal{H}_{int} \quad (3.31)$$

From these equations, together with the expansions (3.26)-(3.29), we obtain a system of equations to determine the expansion coefficients of the scattered field f_{mn}, g_{mn} for given incident field coefficients a_{mn}, b_{mn} .

3.1.5 Incident Plane Wave

Plane waves (cf. Sec. 2.2) are a common way to model monochromatic irradiation, e.g. by laser beams. The plane wave

$$\mathbf{E} = \mathcal{E}e^{-i\omega t} = \mathbf{E}_0 e^{i\mathbf{k}\cdot\mathbf{r} - i\omega t} \quad (3.32)$$

can be expanded in terms of SVWFs and the expansion coefficients are well known. For a x -polarized plane wave, propagating in z -direction i.e. $\mathbf{E}_0 = E_0 \mathbf{e}_x$ and $\mathbf{k}\cdot\mathbf{r} = kr \cos \vartheta$, the expansion coefficients are well known and in the basis used by Doicu et al. [37] read:

$$a_{1n} = -a_{-1n} = i^{n-1} \sqrt{2n+1}, \quad (3.33)$$

$$b_{1n} = b_{-1n} = i^{n-1} \sqrt{2n+1}. \quad (3.34)$$

3.1.6 Scattering from a Spherical Particle

With the incident field known and an expansion ansatz for the scattered and internal fields, we can enforce the boundary conditions Eq. (3.30) on the sphere surface, which we assume to have the radius R . With this we can express the scattered field in terms of the incident field coefficients

$$f_{mn} = T_n^1 a_{mn}, \quad (3.35)$$

$$g_{mn} = T_n^2 b_{mn}. \quad (3.36)$$

with the coefficients

$$T_n^1 = -\frac{[m_r A_n(m_r x) + \frac{n}{x}] j_n(x) - j_{n-1}(x)}{[m_r A_n(m_r x) + \frac{n}{x}] h_n^{(1)}(x) - h_{n-1}^{(1)}(x)}, \quad (3.37)$$

$$T_n^2 = -\frac{[\frac{A_n(m_r x)}{m_r} + \frac{n}{x}] j_n(x) - j_{n-1}(x)}{[\frac{A_n(m_r x)}{m_r} + \frac{n}{x}] h_n^{(1)}(x) - h_{n-1}^{(1)}(x)}. \quad (3.38)$$

Here we have introduced the dimension-less *size parameter* $x = kR$, with k being the wave number. Furthermore we have used the logarithmic derivative of j_n

$$A_n(x) = \frac{d}{dx} [\ln(x j_n(x))] = \frac{[x j_n(x)]'}{x j_n(x)} \quad (3.39)$$

and the relative refractive index $m_r = \sqrt{\varepsilon_i/\varepsilon_e}$. We are now able to evaluate the scattered field expansion coefficients and thus, we can calculate the scattering and extinction cross-section for a spherical particle. We obtain

$$C_{ext} = -\frac{\pi}{k_e^2} \sum_{n,m} \Re \{ f_{mn} a_{mn}^* + g_{mn} b_{mn}^* \} \quad (3.40)$$

3 Numerical Methods

$$C_{scat} = \frac{\pi}{k_e^2} \sum_{n,m} |f_{mn}|^2 + |g_{mn}|^2. \quad (3.41)$$

This enables us to discuss the optical properties of spherical particles. We will now consider a 10 nm sphere of silver in the visible part of the spectrum. The permittivity for silver is taken from Johnson and Christy [22]. To actually calculate the scattering and extinction efficiencies, we will have to truncate the SVWF expansion of the field at some maximum value N_r . Of course, this parameter is crucial for convergence. For plane waves incident on spherical particles, an a priori estimate for the minimum value of N_r as a function of the size parameter $x = kR$ was given by Wiscombe [38]. For our values of λ and R , x is between 0.07 and 0.3. The estimate is then given by

$$N_{r,W} = \lceil x + 4x^{1/3} + 1 \rceil. \quad (3.42)$$

For the values of x mentioned above, $N_{r,W}$ evaluates to $2 \dots 3$. We choose $N_r = 5$ for the following calculation. With an implementation of Mie theory in Mathematica, we are able to evaluate the extinction and scattering cross-sections according to the equations above. Figure 3.2 shows the result for our test particle situated in vacuum and in glass

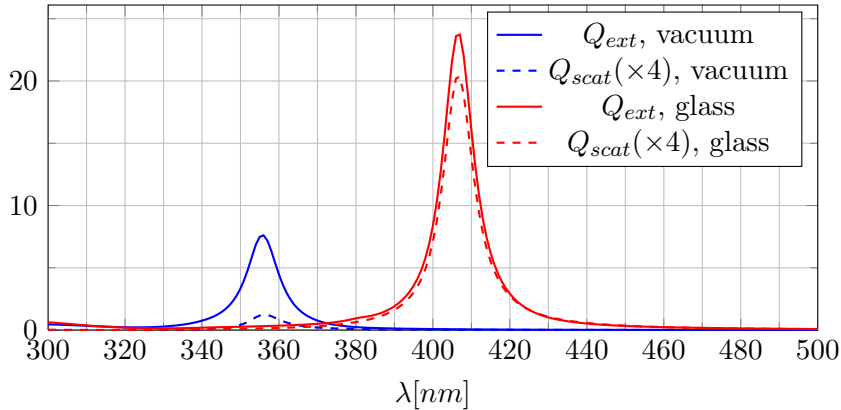


Figure 3.2: Scattering and extinction efficiencies (dashed and solid lines, respectively) for a 10 nm silver sphere in vacuum (blue) and in glass (red). For metallic particles, the absorption is dominant. With increasing refractive index of the surrounding medium, the particle resonance shifts to the red.

(with the permittivity $\varepsilon = 2.25$). For both situations, we see a single resonance peak in the spectra which is dominated by the absorption ($extinction = scattering + absorption$, cf. Sec. 2.3), therefore we scale the scattering efficiency by a factor of 4.

Here, we have the opportunity to study the influence of the surrounding medium on the LSP resonance. First, we see that the increased refractive index causes the resonance to shift to longer wavelengths. Second, the efficiencies are larger for the particle in glass. Intuitively, this can be considered as a result of the decreased propagation velocity of the light in the medium, i.e. the light has "more time" to interact with the particle and

to be absorbed.

3.1.7 Remarks

We conclude this section by noting that the separation ansatz (3.1) can in principle be used in all 17 coordinate systems in which the Laplacian is separable [39], including spheroidal coordinates. We have seen that the analysis is simplified if the scatterer surface coincides with an iso-coordinate surface. Therefore, when we will have to solve the scattering problem for spheroids in Chap. 4, a Mie-like analytical solution would be preferred over a numerical one. In practice, however, the evaluation of the spheroidal harmonics [40] is a computationally expansive task, especially for complex values of the wave vector k that occur in plasmonics due to the non-vanishing imaginary part of the permittivity. While results have been reported for non-absorbing particles [41] and approximative solutions for absorbing particles have been obtained [42], an efficient method to directly evaluate the spheroidal harmonics for plasmonic particles is still missing [43].

3.2 T-Matrix and Null-Field Method

The T-Matrix method can be considered as an extension of Mie Theory introduced in the preceding section and allows to treat scatterers of more general shape. The theory of the method was introduced by Waterman [44], detailed reviews and studies can be found in the books by Mishchenko [45] and Doicu *et al.* [37] and also in the reviews by Mishchenko *et al.* [46], [47]. Again, we expand the incident field \mathcal{E}_{inc} and the scattered field \mathcal{E}_{scat} in terms of the SVWFs defined in Section 3.1.2:

$$\mathcal{E}_{inc} = \sum_{n=1}^{\infty} \sum_{m=-n}^n a_{mn} \mathcal{M}_{mn}^1 + b_{mn} \mathcal{N}_{mn}^1, \quad (3.43a)$$

$$\mathcal{E}_{scat} = \sum_{n=1}^{\infty} \sum_{m=-n}^n f_{mn} \mathcal{M}_{mn}^3 + g_{mn} \mathcal{N}_{mn}^3. \quad (3.43b)$$

We now allow for a more general dependence between incident and scattered field as compared to Mie theory

$$\begin{pmatrix} f_{mn} \\ g_{mn} \end{pmatrix} = \underline{\mathbf{T}} \begin{pmatrix} a_{mn} \\ b_{mn} \end{pmatrix} = \begin{pmatrix} \underline{\mathbf{T}}^{1,1} & \underline{\mathbf{T}}^{1,2} \\ \underline{\mathbf{T}}^{2,1} & \underline{\mathbf{T}}^{2,2} \end{pmatrix} \begin{pmatrix} a_{mn} \\ b_{mn} \end{pmatrix}, \quad (3.44)$$

where we have introduced the *Transition Matrix (T-Matrix)*

$$\underline{\mathbf{T}} = \begin{pmatrix} \underline{\mathbf{T}}^{1,1} & \underline{\mathbf{T}}^{1,2} \\ \underline{\mathbf{T}}^{2,1} & \underline{\mathbf{T}}^{2,2} \end{pmatrix}. \quad (3.45)$$

For a given expansion of the incident field, the T-Matrix yields the expansion coefficients of the scattered field. It might therefore be considered as a property of the scatterer and

3 Numerical Methods

contains all information on the scattering process except the incident field. In practice, the order of the expansions (3.43) has to be finite, of course, such that we have

$$\sum_{n=1}^{\infty} \sum_{m=-n}^n \cdot \mapsto \sum_{n=1}^{N_{rank}} \sum_{m=-\min(M_{rank},n)}^{\min(M_{rank},n)} \cdot. \quad (3.46)$$

The upper bounds must be chosen sufficiently large to obtain converged results. But before discussing the numerical aspects, we will first sketch how to obtain the elements of the T-Matrix. The standard procedure to determine the T-Matrix elements is the so-called Null-Field Method (NFM). This method is described in detail in the book of Doicu *et al.* [37] and we will follow the discussion given there.

3.2.1 Representation Theorems for Electromagnetic Fields

The Null-Field Method (NFM) relies on representation theorems for the electromagnetic fields based on the equations given by Stratton and Chu [48]. They express electromagnetic fields outside a given volume in terms of integrals over the volume's surface.

Let our scatterer occupy a charge- and current-free volume V enclosed by the surface $S = \partial V$. Then we can represent the scattered electric field with the help of the Green function $g(k, \mathbf{r}, \mathbf{r}')$ (cf. Sec. 2.1.8) by

$$\begin{aligned} & \nabla \times \int_S \boldsymbol{\mathcal{E}}_{scat}^T(\mathbf{r}') g(k_e, \mathbf{r}, \mathbf{r}') dS(\mathbf{r}') \\ & + \frac{i}{k_0 \varepsilon_e} \nabla \times \nabla \times \int_S \boldsymbol{\mathcal{H}}_{scat}^T(\mathbf{r}') g(k_e, \mathbf{r}, \mathbf{r}') dS(\mathbf{r}') = \begin{cases} \boldsymbol{\mathcal{E}}_{scat}(\mathbf{r}) & \text{for } \mathbf{r} \notin V \\ 0 & \text{for } \mathbf{r} \in V \end{cases} \end{aligned} \quad (3.47)$$

where $\boldsymbol{\mathcal{H}}_{scat}^T = \mathbf{n} \times \boldsymbol{\mathcal{H}}_{scat}$ and $\boldsymbol{\mathcal{E}}_{scat}^T = \mathbf{n} \times \boldsymbol{\mathcal{E}}_{scat}$ are the tangential components of the magnetic and electric field on S , respectively, with \mathbf{n} being the outward normal to S . A similar equation holds for $\boldsymbol{\mathcal{H}}_{scat}$. This means that we are able to express the scattered fields outside the scatterer in terms of their tangential components on the scatterer surface S . In a similar manner the field inside the scatterer can be represented as

$$\begin{aligned} & \nabla \times \int_S \boldsymbol{\mathcal{E}}_{int}^T(\mathbf{r}') g(k_i, \mathbf{r}, \mathbf{r}') dS(\mathbf{r}') \\ & + \frac{i}{k_0 \varepsilon_i} \nabla \times \nabla \times \int_S \boldsymbol{\mathcal{H}}_{int}^T(\mathbf{r}') g(k_i, \mathbf{r}, \mathbf{r}') dS(\mathbf{r}') = \begin{cases} -\boldsymbol{\mathcal{E}}_{int}(\mathbf{r}) & \text{for } \mathbf{r} \in V \\ 0 & \text{for } \mathbf{r} \notin V \end{cases}. \end{aligned} \quad (3.48)$$

On the scatterer surface S the boundary conditions (2.13) read

$$\boldsymbol{\mathcal{E}}_{int}^T = \boldsymbol{\mathcal{E}}_{scat}^T + \boldsymbol{\mathcal{E}}_{inc}^T, \quad (3.49)$$

$$\boldsymbol{\mathcal{H}}_{int}^T = \boldsymbol{\mathcal{H}}_{scat}^T + \boldsymbol{\mathcal{H}}_{inc}^T, \quad (3.50)$$

3 Numerical Methods

which, along with the two representations above, yield the *Huygens principle* for $\mathbf{r} \notin V$

$$\begin{aligned} \mathcal{E}_{scat}(\mathbf{r}) &= \nabla \times \int_S \mathcal{E}_{int}^T(\mathbf{r}') g(k_e, \mathbf{r}, \mathbf{r}') dS(\mathbf{r}') \\ &+ \frac{i}{k_0 \varepsilon_e} \nabla \times \nabla \times \int_S \mathcal{H}_{int}^T(\mathbf{r}') g(k_e, \mathbf{r}, \mathbf{r}') dS(\mathbf{r}') \quad \text{for } \mathbf{r} \notin V, \end{aligned} \quad (3.51)$$

and the general Null-field equation for $\mathbf{r} \in V$

$$\begin{aligned} -\mathcal{E}_{inc}(\mathbf{r}) &= \nabla \times \int_S \mathcal{E}_{int}^T(\mathbf{r}') g(k_e, \mathbf{r}, \mathbf{r}') dS(\mathbf{r}') \\ &+ \frac{i}{k_0 \varepsilon_e} \nabla \times \nabla \times \int_S \mathcal{H}_{int}^T(\mathbf{r}') g(k_e, \mathbf{r}, \mathbf{r}') dS(\mathbf{r}') \quad \text{for } \mathbf{r} \in V, \end{aligned} \quad (3.52)$$

which relate the tangential components of the internal fields $\mathcal{H}_{int}^T = \mathbf{n} \times \mathcal{H}_{int}$ and $\mathcal{E}_{int}^T = \mathbf{n} \times \mathcal{E}_{int}$ with the scattered field \mathcal{E}_{scat} and the incident field \mathcal{E}_{inc} , respectively. The Huygens principle (3.51) states that the scattered field is caused by the tangen-

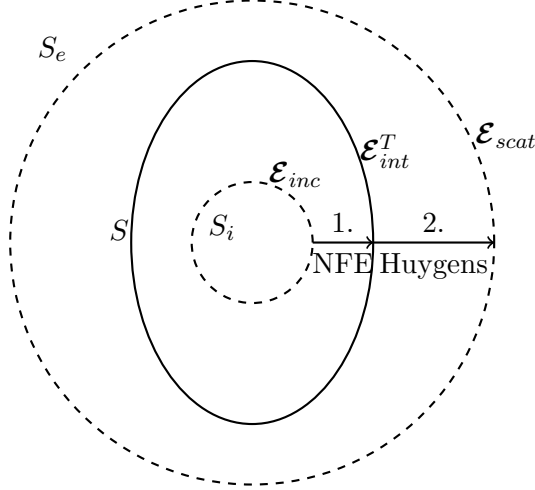


Figure 3.3: **Sketch of the Null-Field Method (NFM).** Two auxiliary spherical surfaces S_i and S_e are introduced inside and outside the scatterer. On S_i , the null-field equation is used to obtain a SVWF representation for the internal surface fields. Then, the Huygens principle is used to calculate the scattered field on any spherical surface outside the scatterer S_e .

tial components of the internal fields $\mathcal{E}_{int}^T, \mathcal{H}_{int}^T$ on the surface S . The null-field equation (3.52) shows that inside the scatterer, the radiation caused by the same tangential fields extinguishes the incident wave.

3.2.2 The Null-Field Method

Figure 3.3 sketches the steps taken in the Null-Field Method. Two auxiliary spherical surfaces S_i and S_e inside and outside the scatterer, respectively, are necessary. Assuming that the incident field \mathcal{E}_{inc} is given in the form of a SVWF expansion (3.43), we can plug it in the null-field equation (3.52). Expanding the dyad $g\mathbf{I}$ in terms of SVWF is also possible and if we restrict \mathbf{r} to lie on the surface S_i , we may exploit the orthogonality of the SVWF [37] to obtain

$$\begin{aligned} \frac{ik_e^2}{\pi} \int_{S_i} \mathcal{E}_{int}^T(\mathbf{r}') \cdot \begin{pmatrix} \mathcal{M}_{\bar{\nu}}^3(k_e \mathbf{r}') \\ \mathcal{N}_{\bar{\nu}}^3(k_e \mathbf{r}') \end{pmatrix} \\ + i \sqrt{\frac{\mu_e}{\varepsilon_e}} \mathcal{H}_{int}^T(\mathbf{r}') \cdot \begin{pmatrix} \mathcal{N}_{\bar{\nu}}^3(k_e \mathbf{r}') \\ \mathcal{M}_{\bar{\nu}}^3(k_e \mathbf{r}') \end{pmatrix} dS(\mathbf{r}') = - \begin{pmatrix} a_\nu \\ b_\nu \end{pmatrix}, \quad \nu = 1, 2, \dots \end{aligned} \quad (3.53)$$

where we have used a compact vector notation and a multi-index $\nu = (m, n)$, $\bar{\nu} = (-m, n)$ with $\nu = 1, 2, \dots$ meaning $n = 1, 2, \dots$ with $m = -n \dots n$. This infinite set of integral equations will be referred to as the null-field equations. They relate the surface fields of the internal fields $\mathcal{E}_{int}^T, \mathcal{H}_{int}^T$ on the scatterer surface S with the incident field coefficients a_ν, b_ν .

Now we choose a truncated SVWF expansion as an ansatz for the surface fields

$$\begin{pmatrix} \mathcal{E}_{int}^{T,N} \\ \mathcal{H}_{int}^{T,N} \end{pmatrix} = \sum_{\mu=1}^N c_\mu^N \begin{pmatrix} \mathbf{n}(\mathbf{r}') \times \mathcal{M}_\mu^1(k_i \mathbf{r}') \\ -i \sqrt{\frac{\varepsilon_i}{\mu_i}} \mathbf{n}(\mathbf{r}') \times \mathcal{N}_\mu^1(k_i \mathbf{r}') \end{pmatrix} + d_\mu^N \begin{pmatrix} \mathbf{n}(\mathbf{r}') \times \mathcal{N}_\mu^1(k_i \mathbf{r}') \\ -i \sqrt{\frac{\varepsilon_i}{\mu_i}} \mathbf{n}(\mathbf{r}') \times \mathcal{M}_\mu^1(k_i \mathbf{r}') \end{pmatrix} \quad (3.54)$$

where N is a truncation multi-index. Inserting the expansion (3.54) into the null-field equations (3.53) yields equations that can be written in matrix form as

$$\underline{\mathbf{Q}}^{31}(k_e, k_i) \begin{pmatrix} c_\nu^N \\ d_\nu^N \end{pmatrix} = - \begin{pmatrix} a_\nu \\ b_\nu \end{pmatrix}. \quad (3.55)$$

The matrix $\underline{\mathbf{Q}}^{31}$ relates the expansion coefficients of the surface fields c_ν^N, d_ν^N on S with those of the incident field a_ν, b_ν .

On any sphere S_e that completely encloses the scatterer V , we can use the Huygens principle (3.51) to calculate the scattered field from the surface fields on S . Assuming that the scattered field can be expressed in terms of a SVWF expansion (3.43), the coefficients f_ν, g_ν are given by an integral over the scatterer surface S

$$\begin{aligned} \frac{ik_e^2}{\pi} \int_{S_i} \mathcal{E}_{int}^T(\mathbf{r}') \cdot \begin{pmatrix} \mathcal{M}_{\bar{\nu}}^1(k_e \mathbf{r}') \\ \mathcal{N}_{\bar{\nu}}^1(k_e \mathbf{r}') \end{pmatrix} \\ + i \sqrt{\frac{\mu_e}{\varepsilon_e}} \mathcal{H}_{int}^T(\mathbf{r}') \cdot \begin{pmatrix} \mathcal{N}_{\bar{\nu}}^1(k_e \mathbf{r}') \\ \mathcal{M}_{\bar{\nu}}^1(k_e \mathbf{r}') \end{pmatrix} dS(\mathbf{r}') = \begin{pmatrix} f_\nu \\ g_\nu \end{pmatrix}, \quad \nu = 1, 2, \dots \end{aligned} \quad (3.56)$$

We have obtained an approximation of the surface fields on S in (3.54) with the coefficients c_ν, d_ν being determined by Eq. (3.55). Plugging the expansion into the

3 Numerical Methods

above equation (3.56), we again arrive at a matrix equation, now relating the scattered field coefficients with the surface field coefficients

$$\begin{pmatrix} f_\nu \\ g_\nu \end{pmatrix} = \underline{\mathbf{Q}}^{11}(k_e, k_i) \begin{pmatrix} c_\nu^N \\ d_\nu^N \end{pmatrix} \quad (3.57)$$

Combining this equation with Eq. (3.55) and comparing it with the form of the definition of the T-Matrix (3.45), we see that the T-Matrix is given by

$$\underline{\mathbf{T}} = -\underline{\mathbf{Q}}^{11}(k_e, k_i) [\underline{\mathbf{Q}}^{31}(k_e, k_i)]^{-1}, \quad (3.58)$$

where the elements of the matrices

$$\underline{\mathbf{Q}}^{pq}(k_e, k_i) = \begin{pmatrix} (Q^{pq})_{\nu\mu}^{11} & (Q^{pq})_{\nu\mu}^{12} \\ (Q^{pq})_{\nu\mu}^{21} & (Q^{pq})_{\nu\mu}^{22} \end{pmatrix} \quad (3.59)$$

are given by

$$\begin{aligned} (Q^{pq})_{\nu\mu}^{11} &= \int_S \left\{ [\mathbf{n}(\mathbf{r}') \times \mathcal{M}_\mu^q(k_i \mathbf{r}')] \cdot \mathcal{N}_\nu^p(k_e \mathbf{r}') \right. \\ &\quad \left. + \sqrt{\frac{\varepsilon_i}{\varepsilon_e}} [\mathbf{n}(\mathbf{r}') \times \mathcal{N}_\mu^q(k_i \mathbf{r}')] \cdot \mathcal{M}_\nu^p(k_e \mathbf{r}') \right\} dS(\mathbf{r}') \end{aligned} \quad (3.60a)$$

$$\begin{aligned} (Q^{pq})_{\nu\mu}^{12} &= \int_S \left\{ [\mathbf{n}(\mathbf{r}') \times \mathcal{N}_\mu^q(k_i \mathbf{r}')] \cdot \mathcal{N}_\nu^p(k_e \mathbf{r}') \right. \\ &\quad \left. + \sqrt{\frac{\varepsilon_i}{\varepsilon_e}} [\mathbf{n}(\mathbf{r}') \times \mathcal{M}_\mu^q(k_i \mathbf{r}')] \cdot \mathcal{M}_\nu^p(k_e \mathbf{r}') \right\} dS(\mathbf{r}') \end{aligned} \quad (3.60b)$$

$$\begin{aligned} (Q^{pq})_{\nu\mu}^{21} &= \int_S \left\{ [\mathbf{n}(\mathbf{r}') \times \mathcal{M}_\mu^q(k_i \mathbf{r}')] \cdot \mathcal{M}_\nu^p(k_e \mathbf{r}') \right. \\ &\quad \left. + \sqrt{\frac{\varepsilon_i}{\varepsilon_e}} [\mathbf{n}(\mathbf{r}') \times \mathcal{N}_\mu^q(k_i \mathbf{r}')] \cdot \mathcal{N}_\nu^p(k_e \mathbf{r}') \right\} dS(\mathbf{r}') \end{aligned} \quad (3.60c)$$

$$\begin{aligned} (Q^{pq})_{\nu\mu}^{22} &= \int_S \left\{ [\mathbf{n}(\mathbf{r}') \times \mathcal{N}_\mu^q(k_i \mathbf{r}')] \cdot \mathcal{M}_\nu^p(k_e \mathbf{r}') \right. \\ &\quad \left. + \sqrt{\frac{\varepsilon_i}{\varepsilon_e}} [\mathbf{n}(\mathbf{r}') \times \mathcal{M}_\mu^q(k_i \mathbf{r}')] \cdot \mathcal{N}_\nu^p(k_e \mathbf{r}') \right\} dS(\mathbf{r}') \end{aligned} \quad (3.60d)$$

In summary, we have exploited the null-field equation and the Huygens principle along with the orthogonality of the SVWF on spherical surfaces to obtain the T-Matrix. It is given in terms of a product of two matrices (one direct, one inverse) containing integrals involving the SVWFs over the scatterer surface S .

3.2.3 Remarks

From the steps taken above, especially the application of the Huygens Principle, it is clear that the scattered field expansion relies on the orthogonality of the SVWF on the spherical surface S_e . This can be chosen to be the smallest circumscribing sphere, however there might be a remaining volume between the scatterer surface S and S_e , in which the field cannot be evaluated directly.

9 *The TM is only valid outside the smallest sphere circumscribing the scatterer.*

However, it is possible to compute the near-field. To that end, one has to expand the field in the intermediate region in terms of both, radiating and propagating SVWF [49].

The integrals (3.60) that define the elements of the matrices $\underline{\mathbf{Q}}^{pq}$ can be evaluated numerically by different methods. In the case of an available parametrization of the scatterer surface, one can use them to evaluate the normal vector \mathbf{n} and evaluate the integrals. An alternative approach is the approximation of the scatterer surface by triangular patches. With this, the evaluation of the integrals for scatterers of almost arbitrary shape is possible.

Furthermore, we have only discussed the most simple case in the above derivation. The method can be extended to inhomogeneous, anisotropic and also layered particles. The treatment of strongly elongated particles is also possible using the Null-field Method with Discrete Sources. There, the representation of the internal field is done by several SVWF expansions with different origins [37]. With this, the method is applicable to a large variety of scatterers. The method is also applicable to systems of particles using a multiple scattering formalism. We will discuss this later in Chap. 6.

Finally, we note that in case of a spherical scatterer, the T-Matrix method actually reduces to Mie Theory [50]. We will discuss T-Matrix results for non-spherical particles in the following two chapters and therefore omit the discussion at this point.

3.3 Discontinuous Galerkin Time-Domain Method

The Discontinuous Galerkin Time-Domain Method (DGTD) is a versatile technique and more general than the T-Matrix method described in the preceding section. It relies on a discretization in space and time.

The DGTD originates from simulations of neutron transport [51] and in 2002 Hesthaven and Warbourton [52] demonstrated the application of the method to Maxwell's equations. An extensive review on the application to photonics was published recently [53] and our discussion will follow this paper. A more detailed account on the method can be found in the book by Hesthaven and Warbourton [54].

To apply the method, we bring Maxwell's equations (2.1) in the form of a conservation law. To that end, we define the *material matrix*

$$\underline{\mathbf{D}} = \begin{pmatrix} \varepsilon(\mathbf{r}) & 0 \\ 0 & \mu(\mathbf{r}) \end{pmatrix}, \quad (3.61)$$

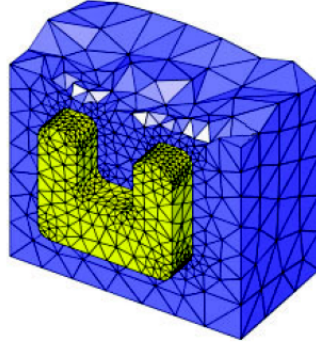


Figure 3.4: Split-ring resonator discretized with a tetrahedral mesh. This picture demonstrates the variation of the element size (*h-refinement*) to resolve structural features. Taken from [53].

the *state vector*

$$\vec{q}(\mathbf{r}, t) = \begin{pmatrix} \mathbf{E}(\mathbf{r}, t) \\ \mathbf{H}(\mathbf{r}, t) \end{pmatrix}, \quad (3.62)$$

and the *flux*

$$\vec{F}(\mathbf{r}, t) = \begin{pmatrix} \vec{F}_x(\vec{q}) \\ \vec{F}_y(\vec{q}) \\ \vec{F}_z(\vec{q}) \end{pmatrix} \quad \text{with} \quad \vec{F}_i(\vec{q}) = \begin{pmatrix} -\mathbf{e}_i \times \mathbf{H}(\mathbf{r}, t) \\ \mathbf{e}_i \times \mathbf{E}(\mathbf{r}, t) \end{pmatrix}. \quad (3.63)$$

Here, the notation $\vec{\cdot}$ has been introduced to distinguish vectors with more than three components from the physical vectors as, e.g. \mathbf{E} . With these definitions, we can write Maxwell's equations in the form of a conservation law

$$\underline{\mathbf{D}} \partial_t \vec{q}(\mathbf{r}, t) + \nabla \cdot \vec{F}(\vec{q}) = 0. \quad (3.64)$$

Obviously, the divergence equations (2.1c) and (2.1a) are explicitly left out of the analysis. It can easily be shown that in time-domain the divergence of the initial fields is conserved. Thus, choosing solenoidal initial fields, they remain solenoidal as long as there are no free charges.

3.3.1 Tessellation of the Computational Domain

The computational domain is divided into a number of small volumes, the *elements*. Although there is a certain freedom of choice, tetrahedral elements are typically chosen. The size of the elements is not fixed but allowed to vary. This allows for a local refinement (called *h-refinement*) of the mesh to improve the representation where necessary as demonstrated in Fig. 3.4.

On each element Δ , the electric and magnetic fields, summarized in the state vector $\vec{q}(\mathbf{r}, t)$, have to satisfy the conservation equation (3.64). For a numerical approximation of the solution, \vec{q}^N , this will in general not be true, instead there will be some residuum

given by

$$\underline{\mathbf{D}}\partial_t\vec{q}(\mathbf{r},t) + \nabla \cdot \vec{F}(\vec{q}) = res. \quad (3.65)$$

Given a set of basis functions $\{L_i\}$ that spans a finite function space, the residuum has to be orthogonal to that space to guarantee the best approximation possible, i.e.

$$\int_{V_\Delta} \left(\underline{\mathbf{D}}\partial_t\vec{q}^N(\mathbf{r},t) + \nabla \cdot \vec{F}(\vec{q}^N) \right) \cdot L_i(\mathbf{r}) d^3r = \int_{V_\Delta} res \cdot L_i(\mathbf{r}) d^3r \equiv 0 \quad (3.66)$$

for all test functions $L_i(\mathbf{r})$. So far, the above equation is completely local, i.e. there is no coupling between the elements. However, electromagnetic waves propagate and therefore, the elements need to be coupled in order to get a meaningful solution on the entire computational domain. This is done via the numerical flux as described in the next section.

3.3.2 Inter-element Coupling

One way to connect the individual elements to one another would be to impose boundary conditions on each element and enforce the physical boundary conditions (2.13) on neighbouring element boundaries. An alternative is to absorb the boundary conditions into modifications of the physical equations. To that end, we integrate (3.66) by parts and obtain

$$\int_{V_\Delta} \left(\underline{\mathbf{D}}\partial_t\vec{q}^N(\mathbf{r},t) \cdot L_i(\mathbf{r}) - \vec{F}(\vec{q}^N) \cdot \nabla L_i(\mathbf{r}) \right) d^3r = - \int_{\partial V_\Delta} \left(\hat{\mathbf{n}} \cdot \vec{F}(\vec{q}^N) \right) \cdot L_i(\mathbf{r}) d^2r \quad (3.67)$$

The right-hand side of the above equation is an integral over the element boundary containing the outward normal $\hat{\mathbf{n}}$ of unit length. The flux \vec{F} will now be replaced with what is called the *numerical flux* \vec{F}^* . Before giving the definition of \vec{F}^* , we will first undo the integration by parts to arrive at the *strong variational formulation of Maxwell's equations*

$$\int_{V_\Delta} \left(\underline{\mathbf{D}}\partial_t\vec{q}^N(\mathbf{r},t) + \nabla \cdot \vec{F}(\vec{q}^N) \right) \cdot L_i(\mathbf{r}) d^3r = \int_{\partial V_\Delta} \hat{\mathbf{n}} \cdot \left(\vec{F}(\vec{q}^N) - \vec{F}^*(\vec{q}^N) \right) \cdot L_i(\mathbf{r}) d^2r \quad (3.68)$$

Still, the right-hand side of this equation is an element-local expression, unless the numerical flux \vec{F}^* is chosen to introduce the coupling to the neighbouring element. The proper choice of the numerical flux is crucial for the convergence of the numerical scheme. Hesthaven and Warburton [52] have shown that a so-called upwind flux leads to a stable and convergent scheme, at least for a nodal scheme, that we will discuss in the next section. The numerical flux is given by

$$\hat{\mathbf{n}} \cdot \left(\vec{F}(\vec{q}^N) - \vec{F}^*(\vec{q}^N) \right) = \left(\frac{1}{Z^+ + Z^-} (\alpha[\delta\mathbf{E} - \hat{\mathbf{n}}(\hat{\mathbf{n}} \cdot \delta\mathbf{E})] + Z^+ \hat{\mathbf{n}} \times \delta\mathbf{H}) \right) \quad (3.69)$$

$$\left(\frac{1}{Y^+ + Y^-} (\alpha[\delta\mathbf{H} - \hat{\mathbf{n}}(\hat{\mathbf{n}} \cdot \delta\mathbf{H})] - Y^+ \hat{\mathbf{n}} \times \delta\mathbf{E}) \right)$$

with the impedance

$$Z^\pm = \sqrt{\frac{\epsilon^\pm}{\mu^\pm}}, \quad (3.70)$$

and the conductance

$$Y^\pm = \frac{1}{Z^\pm} \sqrt{\frac{\mu^\pm}{\epsilon^\pm}}. \quad (3.71)$$

The superscript $-$ and $+$ indicate field and material properties of the local and neighbouring element, respectively, and the differences are

$$\delta\mathbf{E} = \mathbf{E}^+ - \mathbf{E}^- \text{ and } \delta\mathbf{H} = \mathbf{H}^+ - \mathbf{H}^- \quad (3.72)$$

Furthermore, the definition (3.69) contains one free parameter α , the so-called *upwind parameter*. It was shown, that choosing $\alpha \in [0, 1]$ leads to a convergent scheme. For $\alpha = 0$, the flux is central, while for $\alpha = 1$ it is purely upwind. The latter choice leads to the best convergence rates [52].

3.3.3 Semi-discretization of the Problem

We now represent the electric field on an element Δ in terms of an expansion. Using the same function space for the expansion and the test functions is called the *Galerkin choice*. Doing so, e.g. the x -component of the electric field is given by

$$E_x^\Delta(\mathbf{r}, t) = \sum_{j=1}^n \tilde{E}_{x,j}^\Delta(t) L_j(\mathbf{r}). \quad (3.73)$$

Here, we have defined the vector $\tilde{E}_x^\Delta(t)$ which contains the time-dependent expansion coefficients. In general, it will contain only the time-dependent expansion coefficients of the field and the physical field has to be reconstructed by evaluating the above sum. However, if the Lagrange polynomials $L_j(\mathbf{r})$ are chosen as basis functions, the components $\tilde{E}_{x,j}^\Delta(t)$ turn out to be exactly the field values at the node of $L_j(\mathbf{r})$. The reason for this is the defining property of the Lagrange polynomials

$$L_i(\mathbf{r}_j) = \delta_{i,j} = \begin{cases} 0 & \text{for } i \neq j \\ 1 & \text{for } i = j \end{cases} \quad (3.74)$$

for some given nodes \mathbf{r}_i . With this, we see that at node \mathbf{r}_i , the electric field evaluates to

$$E_x^\Delta(\mathbf{r}_i, t) = \sum_{j=1}^n \tilde{E}_{x,j}^\Delta(t) L_j(\mathbf{r}_i) = \tilde{E}_{x,i}^\Delta(t). \quad (3.75)$$

3 Numerical Methods

Therefore, this choice of basis functions leads to what is called a *nodal scheme*. In general, we have

$$L_j(\mathbf{r}) = \sum_{k,l,m=0}^{k+l+m \leq p} a_{k,l,m}^{(j)} x^k y^l z^m \quad (3.76)$$

The coefficients $a^{(j)}$ are determined by the position of the nodes \mathbf{r}_i and Eq. (3.74). The distribution of the nodes over the element has influence on the accuracy. For one-dimensional systems, analytical formulae exists for the optimal choice. For two- and three-dimensional elements, node sets can be generated from the one-dimensional sets by the Warp and Blend technique [55]. They are not the optimal choice, however in practise give reasonable accuracy. Increasing the maximum expansion order p will allow for a local improvement of the accuracy, hence called *p-refinement*.

Defining the mass, stiffness and face mass matrices

$$(\mathbf{M})_{ij} = \int_{V_\Delta} d^3r L_i(\mathbf{r}) \cdot L_j(\mathbf{r}) \quad (3.77)$$

$$(\mathbf{S}_k)_{ij} = \int_{V_\Delta} d^3r L_i(\mathbf{r}) \cdot \partial_k L_j(\mathbf{r}) \quad k = x, y, z \quad (3.78)$$

$$(\mathbf{F})_{ij} = \int_{\partial V_\Delta} d^2r L_i(\mathbf{r}) \cdot L_j(\mathbf{r}) \quad (3.79)$$

we obtain an explicit expression for the time derivatives

$$\partial_t \tilde{\tilde{E}}^\Delta = \frac{1}{\varepsilon^\Delta} (\mathbf{M})^{-1} \cdot \left(\tilde{\mathbf{S}}^\Delta \times \tilde{\tilde{H}}^\Delta + \mathbf{F}_f^\Delta \cdot \frac{\alpha \left[\delta \tilde{\tilde{E}}_f^\Delta - \mathbf{n} \left(\mathbf{n} \cdot \delta \tilde{\tilde{E}}_f^\Delta \right) \right]}{\bar{Z}} + Z^+ \mathbf{n} \times \delta \tilde{\tilde{H}}_f^\Delta \right) \quad (3.80)$$

$$\partial_t \tilde{\tilde{H}}^\Delta = \frac{1}{\mu^\Delta} (\mathbf{M})^{-1} \cdot \left(\tilde{\mathbf{S}}^\Delta \times \tilde{\tilde{E}}^\Delta + \mathbf{F}_f^\Delta \cdot \frac{\alpha \left[\delta \tilde{\tilde{H}}_f^\Delta - \mathbf{n} \left(\mathbf{n} \cdot \delta \tilde{\tilde{H}}_f^\Delta \right) \right]}{\bar{Y}} + Y^+ \mathbf{n} \times \delta \tilde{\tilde{E}}_f^\Delta \right) \quad (3.81)$$

Here, we have introduced the vector of stiffness matrices $\tilde{\mathbf{S}}^\Delta = (\mathbf{S}_x, \mathbf{S}_y, \mathbf{S}_z)^T$ and the difference vectors of the expansion coefficients across the face f $\delta \tilde{\tilde{E}}_f^\Delta, \delta \tilde{\tilde{H}}_f^\Delta$. In practise, one does not store the entire matrices above for each element. Instead, a standard element is introduced for which the matrices are calculated. Then, only the 3×3 Jacobian of the mapping to the standard element have to be stored.

3.3.4 Time Stepping

Having discretized the problem in space leaves us with a time dependent system of ordinary differential equations

$$\partial_t \vec{y} = \vec{f}(t, \vec{y}), \quad (3.82)$$

3 Numerical Methods

an approach usually called the *method of lines*. For the time integration different methods exist and they can be classified as explicit and implicit methods. Both rely on discrete (not necessarily equidistant) time steps t_i and we have the discrete values $\vec{y}_n = \vec{y}(t_n)$. For implicit methods, the updated solution is given by $\vec{y}_{n+1} = \vec{\varphi}(\vec{y}_{n+1}, \vec{y}_n, \vec{y}_{n-1}, \dots)$, which means that we have to solve a system of equations every time step and the function $\vec{\varphi}$ is determined by the specific method. In contrast to that, explicit methods allow for a direct computation of the updated solution and we will focus on one-step methods where only the last time step is required for updating, i.e. $\vec{y}_{n+1} = \vec{\varphi}(\vec{y}_n, \vec{y}_{n-1}, \dots) = \vec{\varphi}(\vec{y}_n)$. More specifically, we use explicit Runge-Kutta methods (RK) for the time integration, the general updating scheme of which reads

$$\vec{y}_{n+1} = \vec{y}_n + \sum_{i=1}^s b_i \vec{k}_i \quad (3.83)$$

$$\vec{k}_i = \vec{f} \left(t_n + c_i \Delta t, \vec{y}_n + \Delta t \sum_{j=1}^s a_{ij} \vec{k}_j \right) \quad (3.84)$$

where for explicit schemes $a_{ij} = 0, j \geq i$ and s defines the number of *stages*. Consistency requires $c_i = \sum_{j=1}^s a_{ij}$ and thus, the choice of a_{ij}, b_i defines the Runge-Kutta scheme. The classical RK requires the storage of $(s+1) \cdot N$ floats, where N is the number of unknowns, which is typically in the order of several 10.000. To reduce the storage requirements, Low Storage Runge-Kutta (LSRK) methods have been introduced [56]. The algorithm reads

$$\begin{aligned} \vec{k}_0 &= \vec{y}_n \\ \vec{p}_i &= A_i \vec{p}_{i-1} + \Delta t \vec{f} \left(t_n + c_i \Delta t, \vec{k}_{i-1} \right) \\ \vec{k}_i &= \vec{k}_{i-1} + B_i \vec{p}_i \\ \vec{y}_{n+1} &= \vec{k}_s \end{aligned}$$

The LSRK only requires to store $2 \cdot N$ floats, no matter how many stages are used. The accuracy is defined by the *order* p of the scheme and requires the numerical error to scale with the time step size as $|\vec{y}_{exact}(t_n) - \vec{y}_n| = \mathcal{O}(h^p)$. The stability is a crucial point, we will shortly discuss it here. A RK method is said to be stable, if for the test equation

$$y' = \lambda y \quad \Re \lambda \leq 0 \quad (3.85)$$

the numerical solution shows the same behaviour as the analytical one, i.e. $|y(t_m + \Delta t)| \leq |y(t_m)| \forall \Delta t > 0$ and $\lim_{\Delta t \Re \lambda \rightarrow -\infty} y(t_m + \Delta t) = 0$. The test equation was introduced 1963 by Dahlquist [57] and can be motivated in the following way. Let $\underline{\mathbf{J}}_{ij} = \partial_j f_i$ be the Jacobian matrix of \vec{f} in Eq. (3.82). If it varies only slowly, we can approximate it as constant matrix and diagonalize it. Then we obtain a set of differential equations of the form (3.85) with λ being the eigenvalues of the Jacobian. We introduce the parameter

3 Numerical Methods

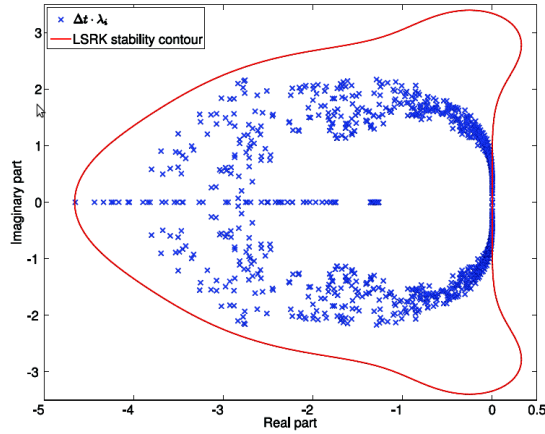


Figure 3.5: Stability contour (red line) of the LSRK by Kennedy and Carpenter [56] and eigenvalues scaled by the time step (blue crosses) for a metallic cavity. Stability requires all scaled eigenvalues to lie within the stability contour. This can be achieved by either adjusting the time step size or modifying the stability contour. Taken from [53].

$z = \Delta t\lambda$. Then we can derive the characteristic polynomial for a Runge-Kutta method

$$R_0(z) = \frac{\det(\mathbf{I} - z\mathbf{A} + z\vec{1}b^T)}{\det(\mathbf{I} - z\mathbf{A})} \quad \text{with } \vec{1} = (1, 1, 1, \dots)^T \quad (3.86)$$

which is a polynomial in z with order s . The necessary condition for stability is given by

$$R_0(\Delta t\lambda) \leq 1. \quad (3.87)$$

The region in the complex plane, where this criterion is fulfilled is always bound for explicit methods, this is the price one pays for not solving a system of equations every time step as in implicit methods. We see that two factors must be brought together

1. The stability contour $R_0(z) = 1$ given by the specific scheme
2. The eigenvalues of the Jacobian scaled with the time step size $\Delta t\lambda$

Stability requires all scaled eigenvalues to lie within the stability contour. This suggests to find a scheme with a stability contour that matches the spectrum of the Jacobian best as done by Diehl *et al.* [58]. Fitting the spectrum into the contour can also be facilitated by choosing the time step sufficiently small. This, however, increases the computational cost, which, of course, is not desirable. An alternative approach is to tailor the stability contour of the specific scheme. Degrees of freedom for this tailoring can be gained by setting the number of stages larger than the order of the scheme $s > p$. With this approach efficiency increases of as high as 50% have been reported [59].

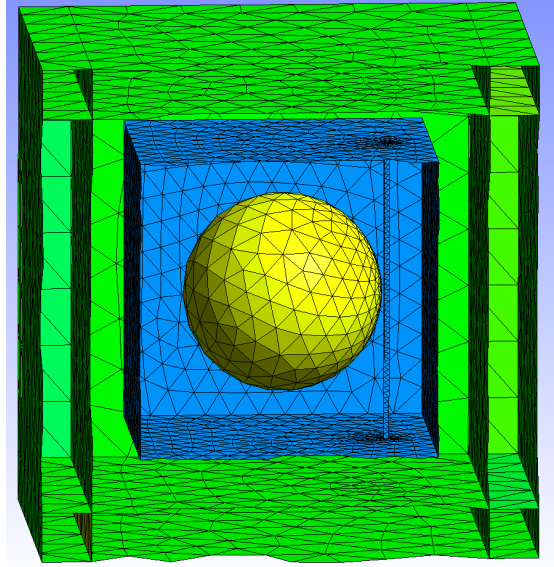


Figure 3.6: Sketch of the geometry for EELS calculation in the Total-Field/Scattered-Field formalism. Inside the blue contour, where the scatterer is located, the total field is propagated. On the other side of the contour, the scattered field is propagated.

3.3.5 Extensions

The above technique allows us to propagate electromagnetic waves in the time-domain, so far, however, nothing was said about how to model excitations and physical systems to facilitate a simulation of real world experiments. We will focus on three aspects that are of special importance.

Modeling Excitations

One possible way to realize excitations in the simulations would be the incorporation of currents and charges that act as sources in Maxwell's equations. This, however, leads to problems, e.g. for point charges, the charge density of which diverge at the charge position. Therefore it would be desirable to have the possibility to inject any given field $\mathbf{E}_{inc}(t)$, $\mathbf{H}_{inc}(t)$ into the computational domain and have it, e.g. interacting with a scatterer. Two approaches to this problem exist, the Total-Field/Scattered-Field (TF/SF) and the Scattered-Field (SF) Formalism. The TF/SF formalism requires a virtual boundary that is introduced in the computational domain. Figure 3.6 shows an example, where we have the TF/SF boundary depicted in blue and the scatterer in yellow. Inside the TF/SF boundary, we want to propagate the total fields, which are the (known) incident field plus the scattered field caused by the interaction of the scatterer with the incident field

$$\mathbf{E}_{total} = \mathbf{E}_{inc} + \mathbf{E}_{scat}. \quad (3.88)$$

3 Numerical Methods

Outside the boundary, we only want to propagate the scattered field

$$\mathbf{E}_{scat} = \mathbf{E}_{total} - \mathbf{E}_{inc}. \quad (3.89)$$

Because we assumed that the incident fields are known, we can simply subtract the incident field when going from inside to outside the TFSF boundary.

The alternative SF approach consists of propagating only the scattered field in the entire domain. We know that the total field satisfies Maxwell's equations. Plugging in $\mathbf{E}_{total} = \mathbf{E}_{inc} + \mathbf{E}_{scat}$ and solving for \mathbf{E}_{scat} , we get explicit equations for the propagation of the scattered field

$$\mu \frac{\partial \mathbf{H}_{scat}}{\partial t} = -\nabla \times \mathbf{E}_{scat} - \sigma^* (\mathbf{H}_{inc} + \mathbf{H}_{scat}) - (\mu - \mu_0) \frac{\partial \mathbf{H}_{inc}}{\partial t}, \quad (3.90a)$$

$$\varepsilon \frac{\partial \mathbf{E}_{scat}}{\partial t} = \nabla \times \mathbf{H}_{scat} - \sigma (\mathbf{E}_{inc} + \mathbf{E}_{scat}) - (\varepsilon - \varepsilon_0) \frac{\partial \mathbf{E}_{inc}}{\partial t}. \quad (3.90b)$$

Here, σ and σ^* are conductivities associated to the imaginary part of ε and μ , respectively. We see that the time derivative of the incident fields act as sources in those regions that have different material properties ε, μ than the material that the incident fields are assumed to propagate in.

Dispersive Materials

Of course, we want to be able to do time-domain calculations for dispersive materials, i.e. those with a frequency-dependent permittivity like metals. We have already mentioned the auxiliary differential equation approach in Sec. 2.4.1. There we have seen that a frequency-dependent permittivity translates to a differential equation for a time-dependent current in time-domain, provided that the permittivity is given by an analytical expression, e.g. a Lorentz-Drude model. As a consequence, for time-domain simulations, we will have to approximate the permittivity by a superposition of Drude and Lorentz terms. Each term gives rise to a current $\mathbf{J}_p(t)$ with $p = 1 \dots N$, the sum of which enters Maxwell's equations. For each element with metallic permittivity, we have to include the differential equation for \mathbf{J} in the time integration, which increases the number of degrees of freedom. Nevertheless, this approach is more efficient than a direct evaluation of the convolution according to Eq. (2.8).

Absorbing boundaries

With finite memory and computation time, a simulation will only be possible for a finite volume and finite time. This means that we will have to terminate the computational domain with a boundary. One special choice are the so-called Perfect Electric Conductor (PEC) boundary conditions, which read

$$\mathbf{E}|_{\partial V} = 0, \quad (3.91)$$

where ∂V is the boundary of the computational domain. This condition would be fulfilled at the interface of a metal with infinitely high conductance, hence the name.

For the simulation of most experiments, a free-space like behaviour would be desirable, i.e. there should be no reflections from the boundaries of the computational domain. One way to achieve this is terminating the domain by an unphysical absorptive material, the impedance of which is matched to the element at the boundary of the physical computational domain to avoid reflections. Then, the waves are absorbed inside the so-called Perfectly Matched Layers (PML). On the outer boundaries, one can choose PEC boundary conditions. Here, the reflected waves are further absorbed inside the PML and only smallest fractions re-enter the physical domain. PMLs were proposed by Berenger [60] and have been successfully applied in free-space-like simulations. An equivalent formulation are the so-called uni-axial PML (UPML) [61], however, they are easier to implement. While Berenger's formulation consisted of splitting certain field components into separate parts, the UPML approach leaves the field untouched but fills the boundaries with an anisotropic material.

Further details can be found in the paper on the specific implementation of the DGTD used in this thesis [62].

3.4 Finite Element Method

The Finite Element Method (FEM) has a lot in common with the DGTD method and we will not discuss it in too much detail. The reason for this is that in contrast to the methods discussed so far, we will not extend the FEM in the following Chapters for EELS as we will do with the T-Matrix and the DGTD method. We will merely employ it in common scattering calculations and therefore not describe details of the method, but merely the aspects crucial for an accurate application to electromagnetic scattering.

Originating from Engineering, the FEM is nowadays used for the solution of all kinds of problems, ranging from structural mechanics to fluid dynamics and of course electrodynamics. We will discuss the commercially available COMSOL Multiphysics as we are going to employ it in our calculations in Chap. 4. A general account on the FEM for the solution of Maxwell's equations is given in [63]. In contrast to the DGTD method, we will use the FEM in frequency-domain but the methods have a lot in common. The discretization of the computational domain relies on a mesh commonly consisting of tetrahedral elements, exactly like discussed in Sec. 3.3.1 for the DGTD method. Also, the choice for the basis functions is the same as for the DGTD, i.e. Lagrange polynomials are used. The coupling between the elements is now done in a straight-forward way by applying the boundary conditions to the face nodes between neighbouring elements. This sort of coupling leads to a system of equations that has to be solved for each frequency. Because each element only couples to its neighbours, the coefficient matrix of the resulting system of equation is sparse, i.e. most of the entries are equal to zero. For moderate systems with 10000 unknowns, the solution can be calculated using direct solvers. They typically require a huge amount of memory but are fast. One particular solver that is used in COMSOL Multiphysics is the *MUltifrontal Massively*

*Parallel Solver (MUMPS)*¹. For larger systems of equations iterative solvers can be used. One particular example is the *Generalized Minimal RESidual (GMRES)* algorithm [64] which is also available in COMSOL. It reformulates the problem in terms of a minimization problem, where the minimum corresponds to the solution of the linear system. Such solvers require more computation time, but less memory, facilitating the solution of large linear systems even on regular desktop computers.

3.5 Other Methods

We finally want to name some other methods that are frequently used in electrodynamics calculations and have not been mentioned yet. The list is by no means complete, but will focus on methods that are typically used for the problems we will discuss in later chapters, especially electron energy loss spectroscopy simulations.

3.5.1 Time Domain Methods

Maybe the most prominent TD method in electrodynamics is the Finite Difference Time Domain (FDTD) method. It directly discretizes the derivatives in Maxwell's equations with finite differences

$$\frac{\partial E}{\partial t} \approx \frac{E(t_{n+1}) - E(t_n)}{\Delta t}, \quad (3.92)$$

which, together with a cleverly chosen equidistant grid introduced by Yee [65], leads to a second order accurate scheme. Due to the simplicity it is widely used, however it has some conceptual weaknesses. The choice of an equidistant grid leads to the so-called staircase approximation of round surfaces. This may result in phase-errors at bend surfaces [66] as well as unphysical enhanced field values at the interface [67].

3.5.2 Frequency Domain Methods

The Multiple Multipole (MMP) method uses multipole expansions to approximate the electric and magnetic field. In contrast to the T-Matrix method, the MMP uses several multipole expansions with different origin. Matching the resulting fields at a boundary leads to a overdetermined system of equations for the expansion coefficients. The boundary conditions also yield an estimate for the numerical error. A prominent implementation is MMP3D and its successors `MaX-1` [68] and `Openmax` developed by Hafner. The method in principle is efficient, however its accuracy strongly depends on the correct choice for the multipole origins with respect to, e.g., a scatterer surface, which requires some experience.

The Discrete Dipole Approximation (DDA) can be considered as a special case of the MMP method. Here, the scatterer is approximated by an equidistant array of dipoles (i.e. multipole expansions of maximum order 1) with polarizability $\alpha(\omega)$. Each dipole feels the electric field of all other dipoles plus the incident field and a self consistent

¹<http://graal.ens-lyon.fr/MUMPS/>

3 Numerical Methods

solution is found. The method was introduced by Purcell and Pennypacker [69] and is also termed *Coupled Dipole Model*. An implementation called `DDScat` was written by Draine and Flatau [70] and is freely available on the internet [71]. While conceptually simple, the method requires massive computational resources to yield accurate results as we will see in Chap. 4 as well as found by other authors [72].

The Boundary Element Method (BEM) [73] transfers Maxwell's equations into a set of integral equations over the particle surface. The integrals involve equivalent surface charges and currents that occur due to the step in the permittivity at the particle surface. The set of integral equations has to be solved self-consistently for the scalar and vector potential inside and outside the particle, and the related surface charges and currents. A discretization of the surface can be used leading to a system of equations with a dense coefficient matrix with dimension $8N$, where N is the number of points in the surface discretization. This makes the method flexible regarding the particle shape, but computationally expansive. Nevertheless, it has been used to obtain a variety of results as we will see in Chap. 5.

4 Shape Transformation of Silver Nano-Particles in Glass

In Sec. 2.5.2 we have discussed the special properties of surface plasmons localized at metallic nano-particles, which include significant near-field enhancements and strong absorption. These properties make metallic nano-particles an interesting candidate for technical applications.

Samples containing ensembles of particles can be produced chemically, e.g. by ion-exchange techniques. This usually results in spherical particles which are distributed randomly inside the sample and show a narrow size distribution. To fabricate micro- or nanoscale devices from these composite materials, improved control of the local particle properties is desirable. One way of achieving this is postprocessing the samples with laser irradiation, i.e. femtosecond laser pulses. The remaining degrees of freedom are the intensity, number of pulses and the wavelength.

Qiu *et al.* [74] have reported the space selective creation of silver nano-particles from ion-doped glass by laser irradiation with a wavelength near the plasmon resonance and subsequent annealing, showing that particles form near the focus of the beam inside the sample. In a subsequent work [75] they have shown that it is also possible to selectively create gold nano-particles inside the sample.

Jiang *et al.* [76] have demonstrated that a selective destruction of gold particles in glass is possible by focussing the laser pulses inside the sample. The authors have demonstrated the capability of their technique by preparing a complex 3d structure in glass [75]. As the created particles are reported to be stable at room temperature, this technique could be used for permanent data storage.

Beyond the creation and destruction of metallic nano-particles in glass, it has been shown that if contained in glass, they undergo a shape transformation if the pulse intensity is chosen carefully [77]. Such experiments were done in the Optics Group of the Martin Luther University Halle-Wittenberg and a model explaining the transformation process was developed, but it is yet subject to debate. In this chapter, we will present the experiments and results that were obtained as well as the model of the process, which is based on the near-field enhancement at the particles. We will use different numerical methods to compute the near-field of the particles and compare the results. Finally, we will perform calculations that, as we will show, support the process model.

4.1 Samples and Experimental Setup

The samples considered here consist of spherical silver nano-particles contained in a soda-lime glass matrix. The samples were produced using a sodium-silver ion exchange

4 Shape Transformation of Silver Nano-Particles in Glass

in a $\text{NaNO}_3/\text{AgNO}_3$ melt, subsequent annealing at 560°C leads to the formation of silver particles [78]. The size of the particles increases with the depth inside the glass [79], such that by removing the topmost layers, particles of certain sizes can be obtained. Extinction measurements with linearly polarized light on thus prepared samples shows no dichroism, therefore the particles are assumed to have a spherical shape [77]. The volume filling factor of the samples is in the order of $f = 10^{-3}$. The extinction spectra of such samples show a strong peak at the frequency of the localized surface plasmon (LSP) resonance (cf. Secs. 2.5.2 and 3.1), which for silver particles of $r = 15$ nm radius in glass is around 410 nm and redshifts with increasing particle size. Upon irradiating the samples with linearly polarized femtosecond laser pulses, a persistent shape transformation of the particles can be induced [77]. It was found that for a fixed wavelength of $\lambda = 400$ nm and a pulse duration of $\tau = 150$ fs, the final shape depends on the intensity and number of pulses applied to the sample. For a single pulse with high intensity of 3.5 TW/cm², oblate spheroids are formed, while for several 1000 pulses with lower intensity, prolate spheroids are obtained. In both cases, the symmetry axis of the particles is parallel to the laser polarization direction. The shape information was deduced from a detailed study of the extinction spectra [80]. Figure 4.1 shows the direction in which the extinction was measured. The polarization of the incident pulses was parallel (a) to the y -axis and (b) the x -axis. The resulting extinction measurements shows two distinct peaks that occur at different wavelengths and for different polarization, which is typical for spheroidal particles. Intuitively, this can be understood if one considers the plasmon

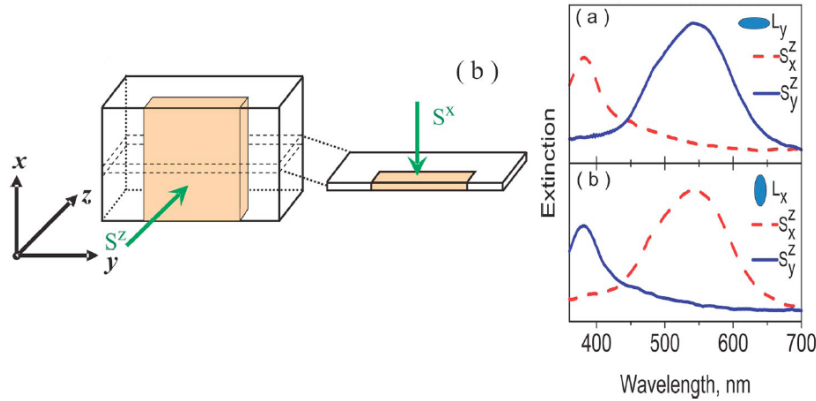


Figure 4.1: Obtaining the full shape information requires extinction measurements in several directions denoted by $S^{x,z}$. The polarization of the incident pulses was parallel to the y -axis (a) and x -axis (b). The measurements indicate that prolate spheroidal particles have formed, with their high symmetry axis parallel to the polarization direction. Adapted from [80].

to be a standing wave on the particle surface. Different circumferences lead to different wavelengths, longer ones leading to a red shift in the resonance. Therefore, a polarization along the long semi-axes of the spheroid (p -polarization) yields a longer LSP wavelength than for polarization parallel to the short semi-axes (s -polarization).

4 Shape Transformation of Silver Nano-Particles in Glass

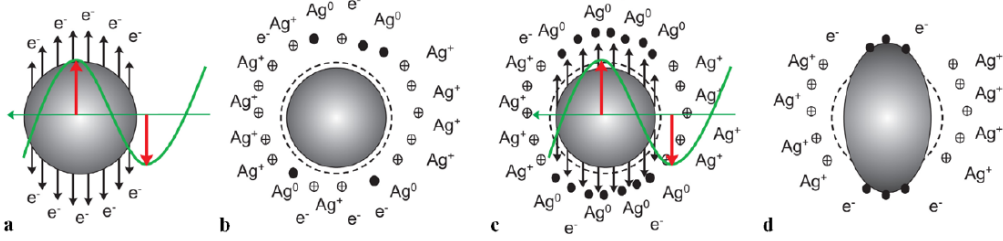


Figure 4.2: Sketch of the processes leading to shape transformation. From [81].

Macroscopically, the microscopic shape transformation manifests itself as dichroism, i.e. a polarization-dependent transmission. Therefore, irradiated samples can be used as wavelength-dependent polarizers [78] and already are commercially available. As the wavelengths where the respective absorption bands are located depend on the aspect ratio of the particles, understanding the transformation process will allow for a tailoring of the spectral properties of such polarizers. Also, many applications, like e.g. optical signal transmission for communication, work in the near-infrared part of the spectrum, such that high aspect ratios are desirable.

It was shown that irradiation near the LSP resonance wavelength yields a spectral gap of 180 nm between the maxima of absorption for s- and p-polarization [81]. Further irradiation with the same wavelength leads to a decreased absorption that is attributed to a (partial) destruction of the particles. Using off-resonant irradiation, it is possible to achieve even larger spectral gaps. In detail, for a sample containing particles of $r = 15$ nm radius, corresponding to a LSP resonance at 410 nm, spectral gaps of up to 620 nm have been reported when using an irradiation wavelength of $\lambda = 550$ nm [82]. It was recently shown that using two wavelengths simultaneously, even higher aspect ratios of up to 4 can be obtained [M1].

4.2 Shape Transformation

To explain the deformation process, a model has been proposed [81]. We will discuss it in order to show the suggested role of electric near-field in the transformation of spherical particles to prolate spheroidal ones. As shown in Fig. 4.2 (a), the electrons in the particle will follow the driving field with virtually no delay, for the electron dynamics happens on femtosecond time-scales [83]. Electrons that are emitted into the glass matrix get trapped there. Here, the near-field shape determines the preferred direction of emission. Then, as sketched in Fig. 4.2 (b), the ionized particle is likely to emit positive silver ions in statistical directions that meet the trapped electrons, the concentration of which is proportional to the electric near-field. After some picoseconds, the heat flow from the particle increases the electron and ion mobility and they can recombine forming silver atoms which finally diffuse back and deposit at the particle surface or form small clusters. For electrons emitted by subsequent pulses (Fig. 4.2 (c)) the remaining silver ions may act as traps and they also recombine to silver atoms. The iteration of this

process leads to a step-by-step transformation of the particles in the direction of the near-field (Fig. 4.2 (d)). In the experiments the final shape of the particles was proven to be spheroidal and we would therefore expect the near-field to be localized at the poles of the sphere or spheroid, respectively. According to the model just outlined, this would exactly yield the obtained shape. Also, there must be a lower threshold for the near-field intensity such that a sufficient number of electrons are emitted in the first place. In the following section we will undertake a numerical simulation of the experiment to see whether theory supports all these assumptions.

4.3 Simulating the Experiment

4.3.1 Modeling the Experiment

From what we know about the experiments so far, we will now try to find an accurate way to simulate the experiments outlined above. In principle, a sequence of pulses with 150 fs duration, approx. $100 \mu\text{m}$ spot size (which also has a Gaussian intensity profile) irradiates the sample containing silver nano-particles with approx. $r = 15 \text{ nm}$ radius. The first attempt would be to model the entire sample and discretize it. Not only would this require the knowledge of the shape and position of all particles in the sample, which is not feasible at all, but a resolution fine enough to accurately represent the electric near-field would lead to prohibitive memory requirements. Therefore we need to simplify the modeling to the essential ingredients. It is known that the volume filling factor of

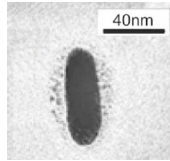


Figure 4.3: Transmission Electron Microscope picture of a silver nano-particle after irradiation with low-intensity femtosecond laser pulses. Adapted from [81].

the sample is $f = 10^{-3}$, so the distance between the particles is huge. The enhanced near-field of the particle plasmon is localized at the particle surface, so it does not affect adjacent particles. Any radiated scattered field undergoes multiple scattering, but decays with increasing distance as $\mathcal{O}\left(\frac{1}{r}\right)$. Therefore, we may regard the particles as isolated.

As we only assume linear material properties here, Maxwell's Equations are linear as well. Therefore, we are able to normalize all fields to the incident field amplitude and directly obtain the field enhancement factor in our calculations.

The pulse duration is $\tau = 150 \text{ fs}$ in the experiment. In vacuum, the spatial extend of the pulse is $d = c\tau \approx 4.5 \cdot 10^{-5} \text{ m}$. Assuming typical wavelengths between 400 nm and 500 nm means that we have around 100 optical cycles interacting with the particle. Therefore, the pulses are long enough to model them with the stationary plane wave illumination. We will determine the dimensions of the spheroids that are formed under the assumption of volume conservation. From Transmission Electron Microscope images

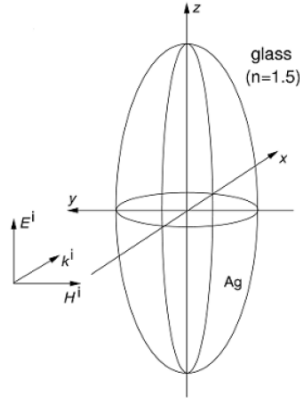


Figure 4.4: Sketch of the test setup. The prolate spheroidal particle has an aspect ratio of 2.4, with semi-axes $r_x = r_y = 11.2$ nm and $r_z = 26.9$ nm. The polarization of the incident electric field is chosen parallel to the long semi-axis. Taken from [M2].

as shown in Fig. 4.3 it is known that even for low intensities a halo around the particle is formed. It is assumed to consist of silver ions. However, the exact properties of this halo are not known and therefore we will neglect it in our calculations.

4.3.2 Comparison of Numerical Methods

As described in Sec. 4.2, the electric field enhancement at the silver nano-particles is claimed to be responsible for the anisotropic emission of electrons that recombine with trapped silver ions leading to the shape transformation. Therefore, in this section, the near-field of the particle will be calculated. While such calculations are frequently encountered in the literature and a wide variety of numerical methods for this task exist, systematic comparisons of such methods in terms of accuracy and efficiency are scarce. In this section, we will carry out such a comparison. According to the aim of this chapter we choose our test system to be a prolate spheroidal particle and assume the excitation by an incident plane wave of a given wavelength. This scattering problem can in principle be solved with a variety of electromagnetic solvers. For spherical particles, the analytical Mie theory, cf. Sec. 3.1, can be used. In spite of the similar well behaved shape, spheroidal particles require the use of numerical methods (the reason for this is discussed in section 3.1.7). As we aim at comparing our results with experimental data, we prefer using experimental permittivity data over approximative analytical models (cf. Sec. 2.1.1) and employ the data for silver from Lynch and Hunter [23]. This rules out time-domain methods from the list of candidates. Among the remaining frequency-domain methods, we have chosen methods that are typically encountered. These methods and the respective implementations are the T-Matrix method, which is described in detail in Sec. 3.2, specifically the Null-Field Method with Discrete Sources (NFM-DS) code by Doicu *et al.* [37]. The Multiple Multipole method as implemented by

4 Shape Transformation of Silver Nano-Particles in Glass

Method	Computation Time (s)
FEM (COMSOL)	20
T-Matrix (NFM-DS 400)	0.2
MMP3D	44
DDScat ($20 \times 20 \times 48$)	20
DDScat ($80 \times 80 \times 192$)	1750

Table 4.1: Computation time for the scattering efficiency for a single wavelength obtained on a standard 4 core desktop computer operating at 2.4 GHz.

Hafner [68], called MMP3D. Furthermore, the Discrete Dipole Approximation code DDScat [70]. Both methods are briefly described in Sec. 3.5.2. Finally, we also employ the Finite Element Method that is presented in Sec. 3.4 and implemented in the software package Comsol Multiphysics. All but the last method are available from the internet free of charge.

The geometric setup for the test calculations is sketched in Fig. 4.4 and inspired by the experiments outlined above. We choose a prolate spheroidal particle with aspect ratio of 2.4 and the same volume as a sphere with 15 nm radius. This results in a long semi-axis length of $r_z = 26.9$ nm and short semi-axes with length $r_x = r_y = 11.2$ nm. The polarization of the incident electric field is chosen parallel to the long semi-axis.

We compare the results for the near-fields and for the scattering efficiency, which is determined by the far-field. Therefore, we expect our comparison to show the accuracy of both near- and far-field regions.

4.3.3 Scattering Efficiency

We first compare the results for the scattering efficiency (cf. Eq. (2.48) in Sec. 2.3) obtained with the different methods. Figure 4.5 shows the scattering efficiency vs. the incident wavelength in a logarithmic plot. The overall shape of the curve is reproduced well by all methods. Deviations occur at the scattering peak around 610 nm, where DDScat with a $20 \times 20 \times 48$ grid of dipoles fails to reproduce both, the amplitude and the spectral position of the peak. Also, there are further deviations for longer wavelength. To obtain results comparable to the other methods, one has to increase the number of dipoles as much as to a $80 \times 80 \times 192$ grid of dipoles, which leads to a computational cost that renders the method rather inefficient. The T-Matrix method is very efficient here because it exploits the symmetry of the problem. For bodies of revolution, the integrals over the scatterer surface Eqns. (3.60) reduce to integrals over the generatrix of scatterer. These integrals have been discretized with 50 and 400 points for comparison. Table 4.1 shows the computation time of the individual methods. These values are to be understood not as a strict benchmark, but merely as a rough estimate of the computational cost.

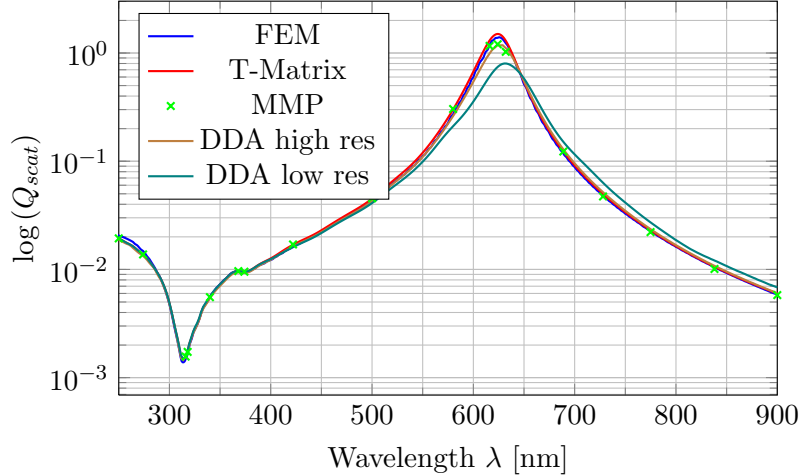


Figure 4.5: Comparison of the scattering efficiencies results for the different numerical methods. All methods expect the low-res `DDScat` yield agreeing results. Adapted from [M2].

4.3.4 Near-field Distribution

The near-field of the spheroid is calculated at two wavelengths for comparison. We choose $\lambda_1 = 310$ nm and $\lambda_2 = 688$ nm corresponding to off- and near-resonance excitation. Before comparing the field distributions in more detail, we plot the near-field to get an impression of the general shape and the correspondence between the methods. For $\lambda_1 = 318$ nm Fig. 4.6 shows that the field intensity attains a minimum at the tip of the spheroid. This behaviour as well as the overall shape of the exterior near-field are reproduced by all methods. Regarding the interior field, `DDScat` fails to produce an accurate field distribution but shows unphysical oscillations inside the spheroid. This stems from the fact that in order to evaluate the fields inside particle, the contribution of the dipole closest to the point of evaluation is neglected to disguise the divergence at the position of the dipole.

For a more quantitative comparison of the results, we introduce a measure for the numerical error in the near-field computation. Due to the lack of an analytical reference solution, we have to choose one numerical solution as reference. Our choice falls to the `MMP3D` solution for two reasons. First, it is semi-analytical and so is the T-Matrix method. Second, however, the `MMP3D` is more general in terms of the expansions that are used to approximate the solution. Where the T-Matrix method only allows multipole expansions, the `MMP3D` supports other solutions of Maxwell's equations as well, like e.g. plane waves, and with the necessary experience in placing the expansions, yields accurate results. With this, we define first the ℓ_ϵ^2 -norm of the discretized electric field

$$\|\mathcal{E}\|_{\ell_\epsilon^2} = \sum_{x_j^2/a^2 + z_j^2/b^2 > \epsilon^2} |\mathcal{E}(x_j, z_j)|^2 \quad 1 < \epsilon < 3. \quad (4.1)$$

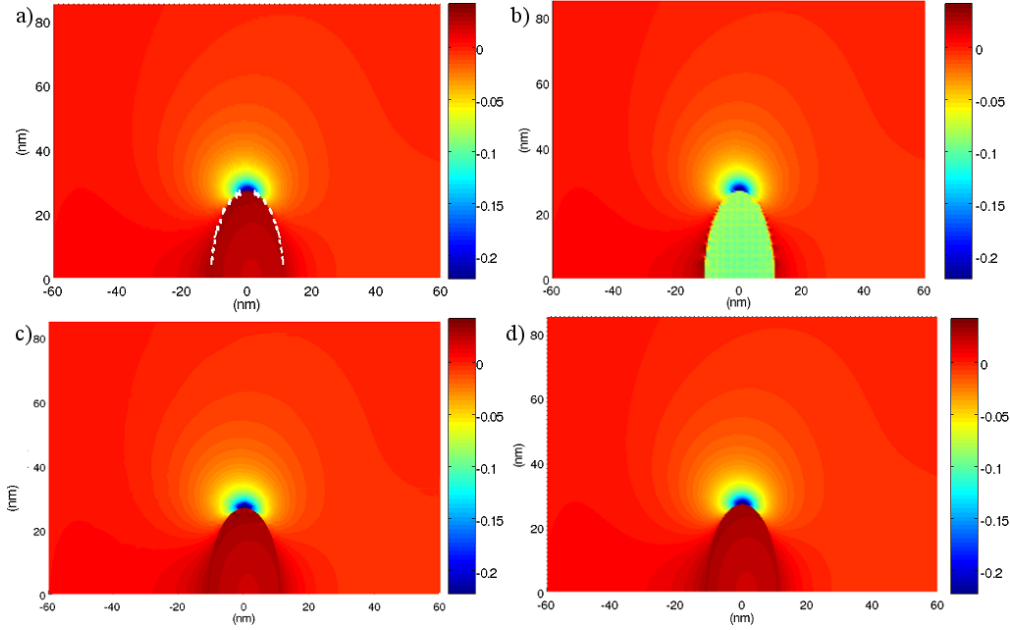


Figure 4.6: Comparison of the near-field norm $|\mathcal{E}|$ in the xz -plane for the different numerical method at $\lambda_1 = 318$ nm. a) T-Matrix, b) DDA (high res), c) FEM, d) MMP. Taken from [M2].

For $\varepsilon = 1$, we are at the immediate vicinity of the particle, increasing ε corresponds to summing over all points that are located between the particle surface and an ellipse with semi-axes $a, b = 2.4a$ in the $x - z$ -plane.

Then, the near-field error with respect to the *MMP3D* solution is defined as

$$\delta(\varepsilon) = \frac{\|\mathcal{E} - \mathcal{E}_{MMP}\|_{\ell_\varepsilon^2}}{\|\mathcal{E}_{MMP}\|_{\ell_\varepsilon^2}}. \quad (4.2)$$

Figures 4.8 and 4.9 show the error $\delta(\varepsilon)$ as a function of the parameter ε for $\lambda_1 = 318$ nm and $\lambda_2 = 688$ nm, respectively.

In both cases, the error increases as we approach the surface of the particle, i.e. as ε approaches one. All methods yield reasonable accuracy for both wavelengths, however the results are generally better for the off-resonance excitation λ_1 . The NFM-DS was used with 50 and 400 integration points on the generatrix of the spheroid. For larger distance from the surface, the NFM-DS results show a very good agreement with the reference MMP3D solution, however approaching the surface, only the high-resolution result shows a good agreement. For DDScat the resolution, which was crucial for correct far-field results, does not show a dramatic influence on the near-field results, however on approaching the particle surface, accuracy decreases. COMSOL shows moderate accuracy over the entire distance range.

The main conclusion from these two figures is that the near-field in the very vicin-

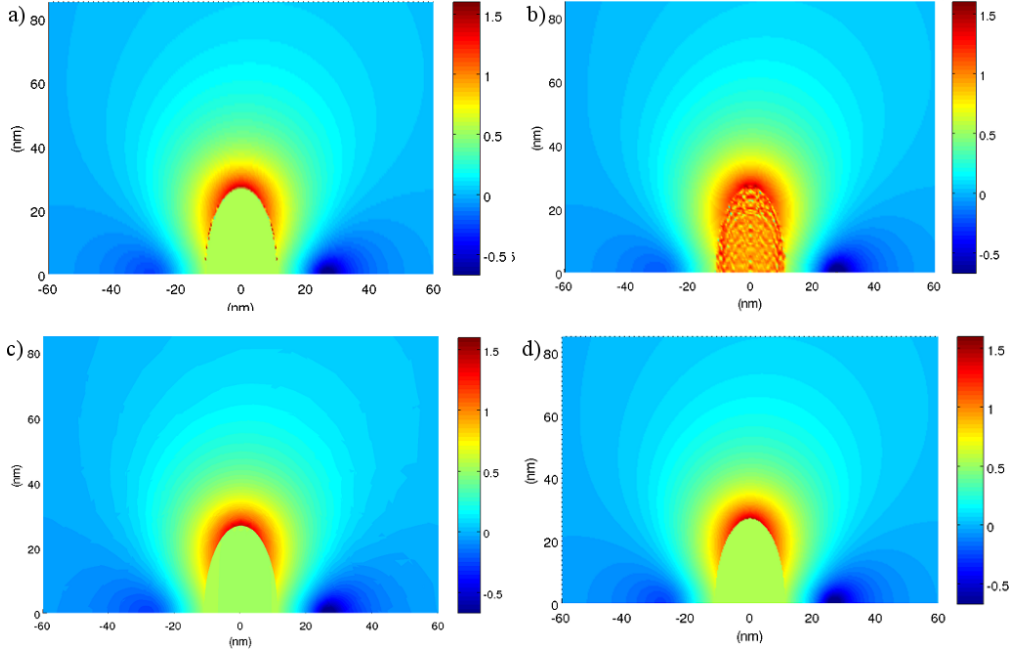


Figure 4.7: Comparison of the near-field norm $|\mathcal{E}|$ in the xz -plane for the different numerical method at $\lambda_2 = 688$ nm. a) T-Matrix, b) DDA (high res), c) FEM, d) MMP. Taken from [M2].

ity shows differences up to 10% and this has to be considered when calculating field-enhancement values.

4.3.5 Field Enhancement as a Function of Aspect Ratio

In the preceding section we have seen that all methods yield accurate results concerning the near-field and the extinction efficiency. Therefore, we are free to choose one method to perform our calculations for the experimental situation as described in section 4.3.1. Our choice falls to the FEM, i.e. COMSOL Multiphysics, because it has shown to give accurate results plus it comes with several postprocessing possibilities like integrating, averaging, etc. that will be useful in the following.

As outlined in Sec. 4.2, the local field enhancement is assumed to be the reason for the anisotropic deformation process. From experiments we know that for single wavelength irradiation there is a maximum aspect ratio that can be obtained before the particles are destroyed. Furthermore, this maximum aspect ratio increases for longer irradiation wavelengths and can be further increased by two wavelength irradiation.

The first fact that supports the model of the transformation process is the shape of the near-field computed in section 4.3.2. The maximum enhancement is observed at the poles of the spheroid as required for the anisotropic emission of electron from the particle (cf. Sec. 4.2). To further elucidate the process, we investigate the field enhancement. To

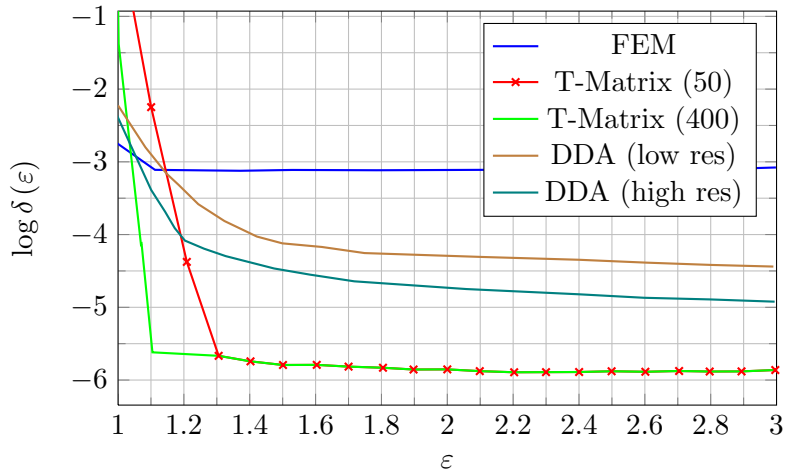


Figure 4.8: Near-field error for off-resonance excitation of the spheroid at $\lambda_1 = 318$ nm as a function of the parameter ε , which determines the distance from the scatterer surface. The errors for different numerical methods are shown in comparison with the MMP result. Adapted from [M2].

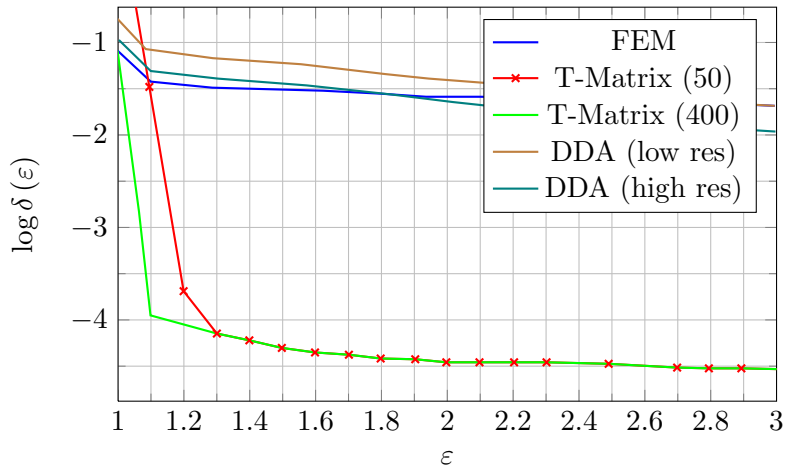


Figure 4.9: Near-field error for on-resonance excitation of the spheroid at $\lambda_2 = 688$ nm as a function of the parameter ε , which determines the distance from the scatterer surface. The errors for different numerical methods are shown in comparison with the MMP result. Here, the error is larger than for the off-resonance excitation. Adapted from [M2].

4 Shape Transformation of Silver Nano-Particles in Glass

that end we define the surface average of the electric field as

$$F_n = \int_{\text{Surface}} \frac{|\mathbf{n} \cdot \boldsymbol{\mathcal{E}}|}{|\boldsymbol{\mathcal{E}}_0|} dA, \quad (4.3)$$

where $\boldsymbol{\mathcal{E}}_0$ is the incident field amplitude. Figure 4.10 shows the field enhancement F_n as a function of the aspect ratio of the particle for different excitation wavelengths. Beside the wavelength used in the experiment ($\lambda_1 = 532 \text{ nm}$ and $\lambda_2 = 800 \text{ nm}$), we have also depicted the enhancement for wavelengths 10 nm above and below these values to show the sensitivity. The enhancement values are normalized to the value observed at a spherical particle at the respective wavelength. As it was demonstrated that the aspect ratio increases with the number of pulses in the experiment [82], we can consider the x -axis of Fig. 4.10 to roughly correspond to the time axis of the transformation process.

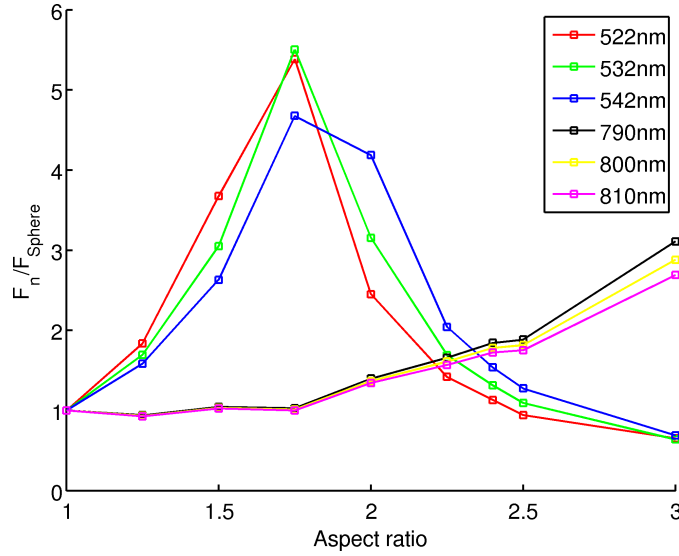


Figure 4.10: Field enhancement as a function of aspect ratio for different excitation wavelengths. We see that using irradiation wavelengths around 532 nm results in huge field enhancements for aspect ratios of up to ≈ 2.4 . For longer wavelength irradiation significant field enhancements can be obtained for larger aspect ratios as well.

The results can then be interpreted in the following way. Assume the particle is irradiated with a single wavelength $\lambda_1 = 532 \text{ nm}$. Then, from the experiment we know that the particle starts to deform to a spheroid. This means that the electric field enhancement at the particle is sufficiently high. Upon further irradiation, the aspect ratio starts to increase, i.e. we are moving along the x -axis and observe huge field enhancements. When reaching an aspect ratio of around 2.2, the field enhancement drops below the initial value and continues to decrease with higher aspect ratio. This is agreement with the experiment, where the maximum aspect ratio obtained is 2.2 – 2.4. Now consider the simultaneous irradiation with two wavelengths $\lambda_1 = 532 \text{ nm}$ and $\lambda_2 =$

800 nm. For the λ_1 pulse, the above reasoning applies again. However, reaching aspect ratios larger than 2, the λ_2 pulse causes a field enhancement above the initial value and thus, the above mechanism of electron and silver ion emission leading to a shape transformation applies for the spheroidal particle with large aspect ratio in the same way as we have explained it for the initially spherical particle above. This would explain the continuation of the deformation process in two wavelength irradiation experiments and also is compatible with the model of the shape transformation process.

4.4 Conclusion

In conclusion, we have seen that it is possible to induce a shape transformation of silver nano-particles in glass by laser irradiation. We have examined the multi-shot low intensity regime, where prolate spheroidal particles are formed. The enhancement of the near-field of the particles is claimed to induce anisotropic electron emission. In combination with isotropically emitted silver ions, this leads to anisotropic material deposition and thus a shape transformation. The near-field patterns were calculated with different numerical methods, showing that all methods yield accurate results, however in the case of the Discrete Dipole Approximation, a huge number of dipoles was required and unphysical features in the internal field occurred. The near-field patterns show huge enhancements at positions that are in agreement with the model of the transformation process. Calculation of the field enhancements for different irradiation wavelengths and aspect ratios are in agreement with both, the finding of a maximum aspect ratio of 2.2 – 2.4 for single wavelength irradiation and larger aspect ratio of up to 4 with two wavelength irradiation. Therefore, the calculations were shown to be reliable and the results support the explanation of the transformation process.

5 Electron Microscopy on Metallic Nano-Particles

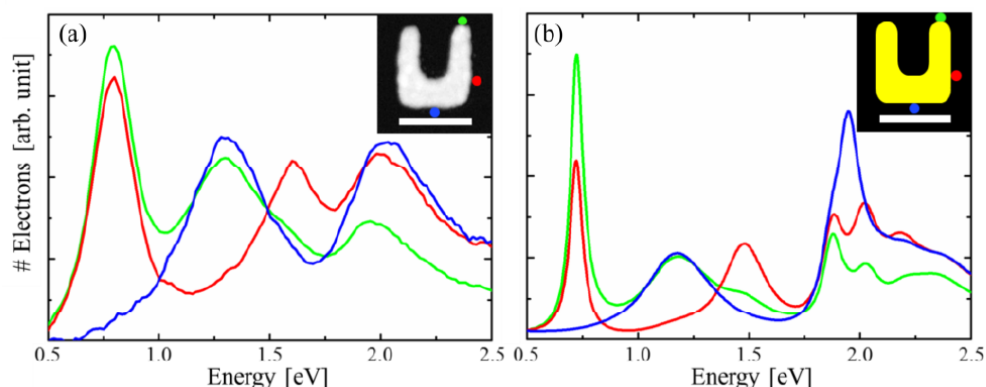


Figure 5.1: Example for Electron Energy Loss spectra for a gold split-ring resonator (inset) as obtained experimentally (left) and numerically (right). The scale bars in the inset are 200 nm. Adapted from [M3]. In this chapter, the interpretation and calculation of such spectra will be discussed.

In the preceding chapter we have discussed the optical properties of metal nano-particles that were probed using laser irradiation. In such experiments, usual laser spot sizes are quite large compared to the particles, such that in general the response is averaged over a large region and consequently over an ensemble of particles. It is, however, also possible to probe single metallic nano-particles in a very precise manner. To that end, the probe *light* has to be replaced by a much finer probe, i.e. electrons in our case. Electron microscopy offers nano-meter spatial resolution and has facilitated the study of single metal nano-particles [84]. Electron Energy Loss Spectroscopy has evolved to a common tool to study the plasmonic properties of metallic nano-particles, because it combines high spatial with reasonable energetic resolution. In such experiments, a tightly focused beam of electrons is directed at the target particle. After interaction with the target, the energy of the electrons is measured. Typical spectra show the count of electrons that suffered a certain energy loss. Due to the high spatial resolution, such spectra can be obtained for different positions of the particle. Figure 5.1 shows spectra for a gold split ring resonator obtained numerically (right) and experimentally (left).

In another flavour of electron microscopy, the beam of electrons is used to excite the

target particle, but here, instead of the electron energy loss, the electromagnetic radiation emitted from the particle is collected. This technique, called Cathodoluminescence Spectroscopy, can be used to characterize the excited plasmonic modes of the target particle.

The aim of this chapter is to introduce the reader to the experimental techniques, give an overview on the particles studied in experiments and finally to show how such spectra can be calculated numerically in the framework of classical electrodynamics. This will enable us to fully understand and interpret Fig. 5.1. In the following two chapters, we will show how we can use the T-Matrix method and the Discontinuous Galerkin Time-Domain method for the calculation of such spectra.

5.1 Electron Energy Loss Spectroscopy

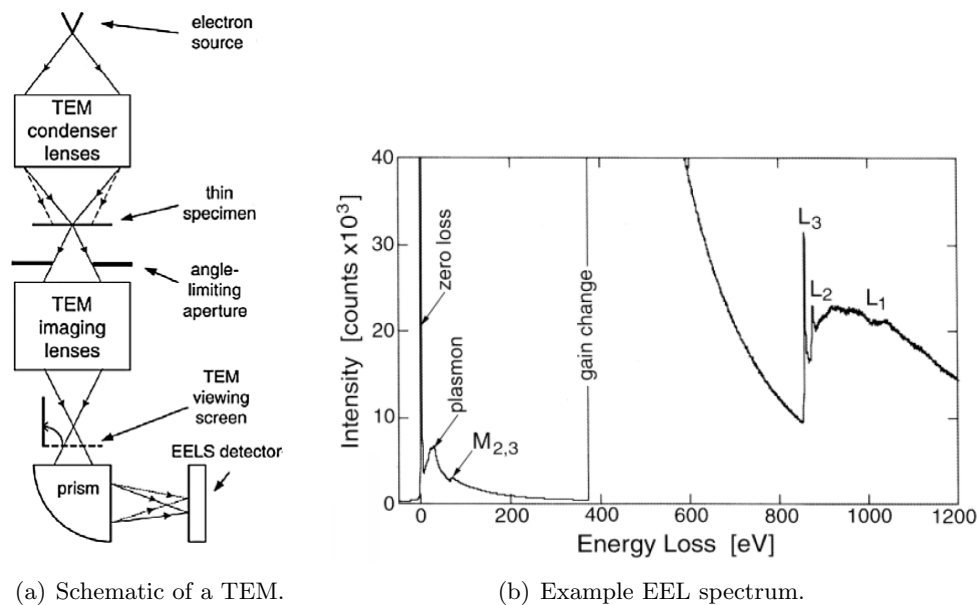


Figure 5.2: (a) Schematic picture of a transmission electron microscope. Taken from [85]
 (b) Example EEL spectrum for nickel. The spectrum shows from left to right the zero-loss peak, a bulk plasmon, the Ni M-edge, a detector gain change, and the Ni L-edges. Taken from [86].

Electron Energy Loss Spectroscopy (EELS) is an experimental technique to examine targets with the help of electrons, usually carried out in a Transmission Electron Microscope (TEM), a schematic of which is shown in Fig. 5.2(a). A tightly focused beam of electrons with well defined initial kinetic energy of typically 50 keV to 300 keV is directed at a target. After interacting with the target, the electrons are filtered by an aperture. This aperture defines the so-called *collection angle*, which is in the order of several milliradians. Finally, the energy of the beam-electrons is measured. Typical EEL

spectra plot the count of electrons that suffered a certain energy loss versus the amount of lost energy. An example spectrum for nickel is shown in Fig. 5.2(b). Assuming energy conservation, all energy losses must be caused by excitations in the target. An important contribution is given by the excitation of bound electrons, the so-called *core loss events*. In the spectra they yield a sharp edge at the ionization energy of the corresponding excitation. For Ni we see the M and L edges in the spectrum. For this reason, EELS can be used for chemical analysis of the target assuming that the atomic energy levels are known. For metallic target particles, another important contribution to the losses is due to the excitation of plasmons - both volume and surface plasmons¹. In the spectra they show up as a more or less symmetric peak around the corresponding plasmon energy, where the width of the peak is proportional to the lifetime of the plasmons. For the particle sizes and materials typically used in the experiments (cf. Tab. 5.1) the plasmon lifetimes are in the order some femtoseconds.

The largest contribution to the spectra, is the so-called zero-loss peak (ZLP). It is caused by the elastically scattered electrons and ideally, it would only give a contribution at exactly zero loss. In the measured spectra, however, it has a finite width of typically some 0.1 eV and thus this width is taken as a measure for the energy resolution in the experiments. If the peak width is too large, it might superimpose low-energy losses. In that case, one can either measure the ZLP without target particle and subtract it from the particle spectrum, or post-processing of the acquired data is necessary. This can be done by deconvolution, e.g. according to Richardson and Lucy [87, 88].

In Energy Filtered EELS, the beam is raster-scanned across the particle and only electrons within a narrow energy window are collected. This leads to a high signal at positions, where the electrons lose a certain amount of energy. Such images, called *EELS maps*, have become an important tool to study the plasmonic properties of metallic nanoparticles, too and we will discuss the correspondence between the EELS maps and the plasmonic eigenmodes of the target particles later on.

5.2 Cathodoluminescence Spectroscopy

A technique closely related to EELS is the so-called Cathodoluminescence Spectroscopy (CLS). In general, *luminescence* is the emission of electromagnetic radiation from a physical system on relaxation from an excited to the ground state. It is termed Cathodoluminescence (CL) if the excitation is done with an electron beam. Conventionally, the term refers to the excitation of solids where the luminescence originates from electronic transitions. In our context this term means the emission of electromagnetic radiation from a metal nano-particle excited by a beam of fast electrons. It is important to notice that in our case the radiation does not directly originate from electronic transitions but the particle facilitates a coupling of the electron's localized field to the far-field. This is also called *radiative decay* of surface plasmons. Thus, the particle effectively acts like an antenna. CL experiments can even yield the angular distribution and the polarization of

¹When the particle size approaches the mean free path of the electrons, as it is the case for the particles we are going to consider, this distinction is not strictly valid anymore.

the emitted radiation. To that end, the radiation emitted from the particle is collected by a parabolic mirror and analysed. In the next section, we will discuss examples of both, EELS and CL measurements for metallic nano-particles.

5.3 Electron Microscopy on Metal Nano-Particles — A Literature Survey

Geometry	Mat.	Size d nm	E_0 keV	ΔE eV	Δx nm	Range eV	Calc.	Comments
Sphere, Rod [89]	Au	25	100	0.25	2 – 3	1 – 4	–	
Triangles [6]	Ag	20 – 300	100	1	–	1 – 5	BEM	
Rod [90]		75 × 400	200	0.17	–	0.5 – 3.5	BEM	
Bulk particle [91]	Ag	30	200	0.6	0.2	3 – 10	Mie in QSA	Particle shape obtained by tomography
Holes in film [92]	Ag	160	–	0.2	–	0.4 – 3.5	–	
Sphere dimers [93]	Ag	10 – 15	300	0.2	0.3	1 – 6	FEM	Dark modes are studied
Spherical, chains of [94]	Ag	20	100	0.27	0.5	2.4 – 4	DDA, optical	
Sphere, Rod, dimers of [95]	Au	20 – 80	200	0.22	2	0.5 – 5	BEM	Dark and bright modes
Triangle [96]	Ag	100	15	–	10	1.5 – 3	FDTD	CL measurement
SRR [M3]	Au	0 – 0	0	0	0	5	DGTD	Babinet's principle
Chain of rods [7]	Au	100	30	–	10	1.5 – 3	Dipole model	CL measurement

Table 5.1: Selected EEL and CL measurements from the recent literature. The particle geometry and material is listed along with experimental parameters if stated explicitly. The *Size* column gives typical length scales of the respective particles. Furthermore we list the initial energy E_0 of the electrons, the energy resolution ΔE , and the spatial resolution Δx . The *Calc.* column indicates the method that was used to calculate spectra (if any).

While EELS is a versatile technique and can be performed in many different ways, we will now focus on the experiments relevant for this work and that is EELS on metallic nano-particles. Table 5.1 lists such measurements selected from the recent literature. Considering the parameters, we see that the initial energy of the beam-electrons is in the range of $E_0 = 10 \text{ keV} \dots 300 \text{ keV}$, which corresponds to velocities of $v = 0.29 \dots 0.9c$, where c is the vacuum speed of light. The considered energy losses range from 0.4 eV to 10 eV and these energies are typical for the plasmon losses. The energy and spatial resolution ΔE and Δx vary but can be as small as $\Delta E = 0.1 \text{ eV}$ and $\Delta x = 0.2 \text{ nm}$. Given this, we see that it is possible to investigate particles with typical sizes of 10 nm and larger. In the experiments listed in Tab. 5.1 mostly chemically synthesized particles are used possessing a more or less spherical shape. Interestingly, Chu *et al.* [91] have used electron tomography to accurately determine the 3D shape of their particle.

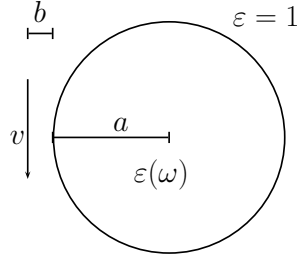


Figure 5.3: Sketch of the general setup for EELS calculations. We assume a metallic particle of size a with permittivity $\varepsilon(\omega)$. The electron hits the particle with an impact parameter b at velocity v .

Unfortunately, they cannot exploit this information for their calculations because they compare their measurements with spectra for spherical particles within the quasi-static approximation, cf. Sec. 2.1.8. Beside chemically synthesized particles, also structures that were fabricated by Focused Ion Beam techniques and Electron Beam Lithography in [92] and [M3], respectively, are used. This opens up the opportunity to fabricate functional plasmonic structures, the properties of which can be examined by EELS. Beyond single particle experiments, several authors use particle systems to study the coupling between the particles, be it sphere dimers [93], chains of spherical particles [94] or an array of holes in a silver film [92]. Sphere dimers are especially well suited for studying the inter-particle coupling and we will discuss them in Sec. 6.3.3 and Sec. 7.4 in more detail.

5.4 The Loss- and Cathodoluminescence-Probability

We will now be concerned with the question how loss spectra as introduced in the preceding section can be calculated from electrodynamics. As depicted in Fig. 5.3, let us consider a single electron that is incident on the target particle with an impact parameter $b > 0$, such that the electron trajectory does not penetrate the particle. Upon approaching the particle, the field of the electron will interact with the electrons in the particle causing charge fluctuations. These charge fluctuations will result in some induced electric field \mathbf{E}^{ind} . This field now acts back onto the electron and therefore, the electron will suffer an energy loss

$$\Delta E = e \int_{-\infty}^{+\infty} dt \dot{\mathbf{r}}_e(t) \cdot \mathbf{E}^{ind}(\mathbf{r}_e(t), t), \quad (5.1)$$

where $\mathbf{r}_e(t)$ and e denote the trajectory and charge of the electron, respectively.

If we define the probability that the electron loses a certain amount of energy $\hbar\omega$

as $P(\omega)$, we can also express the overall energy loss as an integral over this probability

$$\Delta E = \hbar \int_0^{+\infty} d\omega \omega P(\omega). \quad (5.2)$$

We will call $P(\omega)$ electron energy loss probability (EELP). To obtain an explicit expression for the EELP, we can bring Eq. (5.1) in a form similar to Eq. (5.2). To that end, we introduce the Fourier Transform of the induced field and exploit the symmetry property of the Fourier components of real fields (2.20):

$$\begin{aligned} \Delta E &= e \int_{-\infty}^{+\infty} dt \dot{\mathbf{r}}_e(t) \cdot \mathbf{E}^{ind}(\mathbf{r}_e(t), t) \\ &= e \int_{-\infty}^{+\infty} d\omega \int_{-\infty}^{+\infty} dt \dot{\mathbf{r}}_e(t) \cdot \mathcal{E}^{ind}(\mathbf{r}_e(t), \omega) e^{-i\omega t} \\ &= e \int_{-\infty}^0 d\omega \dots \mathcal{E}^{ind}(\mathbf{r}_e(t), \omega) e^{-i\omega t} + e \int_0^{+\infty} d\omega \dots \mathcal{E}^{ind}(\mathbf{r}_e(t), \omega) e^{-i\omega t} \\ &= e \int_0^{+\infty} d\omega \dots \mathcal{E}^{ind}(\mathbf{r}_e(t), -\omega) e^{i\omega t} + e \int_0^{+\infty} d\omega \dots \mathcal{E}^{ind}(\mathbf{r}_e(t), \omega) e^{-i\omega t} \\ &\stackrel{(2.20)}{=} e \int_0^{+\infty} d\omega \dots \left\{ \mathcal{E}^{ind}(\mathbf{r}_e(t), \omega) e^{-i\omega t} \right\}^* + e \int_0^{+\infty} d\omega \dots \mathcal{E}^{ind}(\mathbf{r}_e(t), \omega) e^{-i\omega t} \\ &= 2e \int_0^{+\infty} d\omega \int_{-\infty}^{+\infty} dt \Re \left\{ \dot{\mathbf{r}}_e(t) \cdot \mathcal{E}^{ind}(\mathbf{r}_e(t), \omega) e^{-i\omega t} \right\}, \end{aligned}$$

By comparing the above expression with Eq. (5.2) we obtain an explicit expression for the loss probability $P(\omega)$. This expression, however, would include the equation of motion of the electron that moves along the particle, because $\dot{\mathbf{r}}_e(t)$ is contained in the above equation. To solve this problem, we would have to take into account the interaction between the induced electric and magnetic field and the electron given by the Lorentz force. In order to simplify things, we will make use of an approximation and assume that the electron moves along a straight-line trajectory. We have seen in Tab. 5.1 that typical initial electron energies are in the order of 100 keV and the losses are in the order of several electron volts, i.e. the losses are negligible compared to the initial energy. Furthermore, the collection angle in EELS experiments is in the order of several milliradians. Thus the momentum component of the electron transverse to the straight-line trajectory is small compared to the parallel component and therefore also negligible.

10 We assume that the momentum of the electron remains unchanged during the excitation of the target particle, i.e. $\mathbf{v}_e = \text{const}$. This is called the no-recoil approximation (NRA).

Besides simplifying the analysis of the energy losses, the NRA makes a solution of the problem in frequency domain possible in the first place as we will see in Chap. 6. If we assume that $\dot{\mathbf{r}}_e(t) = \mathbf{v}_e = \text{const}$ we get the following result.

11 Within the no-recoil approximation (NRA) the electron energy loss probability (EELP) evaluates to

$$P(\omega) = \frac{2e}{\hbar\omega} \int_{-\infty}^{+\infty} dt \Re \left\{ \mathbf{v}_e \cdot \boldsymbol{\mathcal{E}}^{ind}(\mathbf{r}_e(t), \omega) e^{-i\omega t} \right\}. \quad (5.3)$$

Thus, the EELP is determined by the projection of the induced electric field Fourier component $\boldsymbol{\mathcal{E}}^{ind}$ on the electron trajectory. If we assume that the electron trajectory is parallel to the z -axis, i.e. $\mathbf{v}_e = v_e \mathbf{e}_z$, which is always possible without loss of generality, because we can compensate this by an appropriate rotation of the target particle, then only the z -component of the electric field contributes to the losses. This means that EELS can be used to map the z -component of the excited eigenmodes of the particle with high precision and we will demonstrate this in Sec. 7.7. Also, the EELP is related to the photonic density of states [97], although not necessarily in a straight-forward manner [98].

As discussed above, it is also possible, that the excited particle emits radiation. The energy emitted by the particle in terms of radiating electromagnetic fields is given by the integral over the Poynting vector (2.40) over a closed surface S , which for the sake of simplicity shall be spherical, around the particle

$$\Delta E_{rad} = \int_S d(\vartheta, \varphi) \int dt r^2 \mathbf{e}_r \cdot [\mathbf{E} \times \mathbf{H}]. \quad (5.4)$$

We have already encountered this expression in Sec. 2.3 where we have discussed the scattering cross-section. Thus, the energy ΔE_{rad} is a measure for the coupling of the excited eigenmodes to the far-field. Again, expressing this in terms of a probability, we have

$$\Delta E_{rad} = \int_S d(\vartheta, \varphi) \int \omega d\omega P_{rad}(\omega, \vartheta, \varphi). \quad (5.5)$$

By similar reasoning as above we obtain the probability of an emission of radiation with frequency ω in the direction (ϑ, φ)

$$P_{rad}(\omega, \vartheta, \varphi) = \frac{r^2}{\omega} \Re \{ [\boldsymbol{\mathcal{E}}(\omega, \vartheta, \varphi) \times \boldsymbol{\mathcal{H}}^*(\omega, \vartheta, \varphi)] \cdot \mathbf{e}_r \}. \quad (5.6)$$

As this quantity is measured in CL experiments, we are going to call this the Cathodoluminescence Probability (CLP). If we choose the spherical surface S to be infinitely

large, we can replace the electric and magnetic field in Eq. (5.6) by appropriate far-field expressions. Every propagating electromagnetic wave has the asymptotic form of an outgoing spherical wave

$$\mathcal{E}(\mathbf{r}, \omega) = \frac{e^{ikr}}{r} \left\{ \mathcal{E}_\infty(\vartheta, \varphi) + \mathcal{O}\left(\frac{1}{r}\right) \right\}, r \rightarrow \infty, \quad (5.7a)$$

$$\mathcal{H}(\mathbf{r}, \omega) = \frac{e^{ikr}}{r} \left\{ \mathcal{H}_\infty(\vartheta, \varphi) + \mathcal{O}\left(\frac{1}{r}\right) \right\}, r \rightarrow \infty, \quad (5.7b)$$

where $\mathcal{E}_\infty, \mathcal{H}_\infty$ are the so called far-field patterns that determine the far-field amplitude in a given direction. In addition, the far-field is purely transverse, i.e.

$$\mathcal{H}_\infty = \sqrt{\frac{\varepsilon_e}{\mu_e}} \mathbf{e}_r \times \mathcal{E}_\infty, \quad (5.8)$$

$$\mathbf{e}_r \cdot \mathcal{H}_\infty = \mathbf{e}_r \cdot \mathcal{E}_\infty = 0. \quad (5.9)$$

With this, we can express the CL probability (5.6) as

$$P_{rad}(\omega, \vartheta, \varphi) = \frac{1}{\omega} \sqrt{\frac{\varepsilon_e}{\mu_e}} |\mathcal{E}_\infty(\vartheta, \varphi)|^2. \quad (5.10)$$

The angular distribution of the radiation can be used to characterize the corresponding eigenmode of the particle and we will discuss this in more detail when presenting numerical results for different particles in the following two chapters.

5.4.1 Analytical and Numerical Results

The EELP within the NRA can be evaluated once the induced field \mathcal{E}^{ind} is known. As discussed in Sec. 2.1.8, one can make use of the quasi-static approximation (QSA) and solve the Laplace instead of the Helmholtz equation. This simplifies the analysis and indeed, analytical results for the loss probability have been obtained for a number of particle systems like spheres [99], spheres embedded in a substrate [100] and spheroids [101]. Also, results for sphere dimers were obtained by solving the Laplace equation in bi-focal spherical coordinates [102]. All these results neglect retardation effects because they were derived under the QSA. The first result including full retardation was reported by García de Abajo for spherical particles [103]. With this, the influence of retardation effects can be studied and we will show example calculations in Sec. 6.3.1 showing that already for small particles retardation effects have to be taken into account. Thus it is necessary to go beyond the QSA.

Concerning numerical results, we have already mentioned the methods commonly used in Tab. 5.1. Frequency-domain methods that have been used to simulate electron microscopy experiments are the Finite Element Method (FEM), the Boundary Element Method (BEM) and the Discrete Dipole Approximation (DDA), cf. Sec. 3.5.2. All methods are flexible concerning the scatterer shape, however the BEM is computationally more expensive than the FEM due to the self-consistent solution. The DDA was used

for simulations, however an enormous number of dipoles is necessary to get converged results [72], which renders the method rather inefficient.

Concerning time-domain methods, so far only the FDTD method has been used to simulate CL spectra [96]. In these simulations the electron beam is modeled as a series of dipoles, each with a phase delay corresponding to the electron velocity. A detailed discussion of this approximation and its accuracy is not given. We will see later in Chap. 7 that a time-domain approach without this approximation is possible and also facilitates the simulation of EELS experiments.

5.4.2 Loss Probability in Experiments

In typical experiments, the currents in the TEM are so small, that only a single electron is in the instrument at a time. Taking the classical derivation of the EELP serious would require each single electron to lose exactly the same amount of energy ΔE from Eq. (5.1). As evident from the measured spectra, this is not the case. Nevertheless the classically obtained EELP is commonly used for the interpretation of EELS experiments and shows a very good agreement.

5.4.3 Dimensionless Units

In the following two chapters we will present calculations for the loss probability and photon emission probability for metallic nano particles. We want to briefly comment on the units we use in the calculations.

In Sec. 2.1.6 we have seen that Maxwell's equations are scale invariant. As the typical size of our particles is in the nano-meter range, we are going to specify all lengths in units of $a = 1$ nm. This can be compensated for by rescaling all frequencies accordingly. Furthermore, we set the following constants to unity: the vacuum speed of light c , the elementary charge e , Planck's constant \hbar .

These units will be used for both, the T-Matrix calculations in Chap. 6 as well as for the DGTD calculations in Chap. 7, thus we are able to directly compare the results.

6 The T-Matrix Method for Electron Microscopy

In this chapter, we will apply the T-Matrix Method to the calculation of the electron energy loss probability (5.3) and the cathodoluminescence probability (5.6). In the preceding Chap. 5 we have seen that the evaluation of the probabilities is based on the field that a moving electron induces in a target particle. In Sec. 3.2 we have introduced the T-Matrix Method and shown, that for a given incident field and particle, it can be used to calculate the scattered field. Therefore, it can also be applied to the probability calculation. If the field that is caused by a moving electron can be expanded in terms of Spherical Vector Wave Functions, we can use it as incident field in the T-Matrix formalism to calculate the induced field and finally evaluate the probabilities. We will see in this chapter, that the expansion coefficients can be evaluated and that the T-Matrix Method turns out to be a very efficient approach to the calculation of the loss and cathodoluminescence probability. This will be demonstrated for selected particle shapes that are also typically encountered in experiments.

6.1 Electron Excitation

To implement the electron excitation in the T-Matrix Method, we have to evaluate the Spherical Vector Wave Function (SVWF) expansion coefficients for the field caused by a moving electron. In Sec. 7.1, we will study the charge- and current density of a moving electron as a function of position and time to obtain the electric and magnetic field caused by it. Attempting to Fourier transform these fields and project them onto the SVWFs would be the straight-forward approach to obtain the expansion coefficients. A more elegant way was proposed by Gracia de Abajo using the angular momentum operator formalism [103]. With the expressions of (3.23) we can write the field expansion of the incident field (3.26) as

$$\mathcal{E}_{inc} = \sum_{n=1}^{\infty} \sum_{m=-n}^n \tilde{a}_{mn} \hat{\mathbf{L}} u_{nm}^1(k\mathbf{r}) + \tilde{b}_{mn} \nabla \times \hat{\mathbf{L}} u_{nm}^1(k\mathbf{r}), \quad (6.1)$$

where some factors have been absorbed in the new coefficients $\tilde{a}_{mn}, \tilde{b}_{mn}$ to take different normalization of the basis functions into account. Multiplying (6.1) with $\hat{\mathbf{L}} \cdot$ on both

sides yields

$$\begin{aligned}\hat{\mathbf{L}} \cdot \boldsymbol{\mathcal{E}}_{inc} &= \sum_{n=1}^{\infty} \sum_{m=-n}^n \tilde{a}_{mn} \hat{L}^2 u_{nm}^1(k\mathbf{r}) + \tilde{b}_{mn} \underbrace{\hat{\mathbf{L}} \cdot \nabla \times \hat{\mathbf{L}}}_{=0} u_{nm}^1(k\mathbf{r}) \\ &= \sum_{n=1}^{\infty} \sum_{m=-n}^n \tilde{a}_{mn} \hat{L}^2 u_{nm}^1(k\mathbf{r}) = \sum_{n=1}^{\infty} \sum_{m=-n}^n \tilde{a}_{mn} n(n+1) u_{nm}^1(k\mathbf{r})\end{aligned}\quad (6.2)$$

where we have used that the angular part of u^1 , that \hat{L}^2 is acting on, is an eigenfunction of \hat{L}^2 , cf. Eq. (3.12). Similarly, multiplying (6.1) with $(\hat{\mathbf{L}} \times \nabla) \cdot$ on both sides we get an expression involving only the coefficient \tilde{b}_{mn} . Thus, we are able to obtain the contribution of the SVWFs \mathcal{M}, \mathcal{N} by means of projection.

Using the charge density, we can express the electric field with the help of the Green function of the Helmholtz equation (2.27)

$$\mathbf{E}^{ext}(\mathbf{r}) = \left(\nabla - \frac{ik\mathbf{v}}{c} \right) \int dt e^{i\omega t} G(\mathbf{r} - \mathbf{r}_e(t)), \quad (6.3)$$

where we have set the electron charge $q = -1$. We can employ the expansion of the Green function in terms of scalar wave functions

$$G = 4\pi k \sum_{n=1}^{\infty} \sum_{m=-n}^n j_n(k\mathbf{r}) ih_n^{(1)}(k\mathbf{r}_e(t)) Y_{mn}(\Omega_{\mathbf{r}}) Y_{mn}^*(\Omega_{\mathbf{r}_e(t)}) \quad (6.4)$$

to finally obtain an expression for the field caused by the moving electron

$$\mathbf{E}^{ext}(\mathbf{r}) = \left(\nabla - \frac{ik\mathbf{v}}{c} \right) \sum_{n=1}^{\infty} \sum_{m=-n}^n j_n(k\mathbf{r}) Y_{mn}(\Omega_{\mathbf{r}}) \phi_{mn} \quad (6.5)$$

with

$$\phi_{mn} = 4\pi ik \int dt e^{i\omega t} h_n^{(1)}(k\mathbf{r}_e(t)) Y_{nm}^*(\Omega_{\mathbf{r}_e(t)}). \quad (6.6)$$

Now we can apply the projections above (Eq. (6.2)) to the electric field (6.5) to obtain the expansion coefficients. Taking into account that $\hat{\mathbf{L}} \cdot \nabla = (\nabla \times \hat{\mathbf{L}}) \cdot \nabla = 0$ and that $\mathbf{v} \cdot \hat{\mathbf{L}} = v\hat{L}_z$, the projection of the above field on $\hat{\mathbf{L}}$ is

$$\hat{\mathbf{L}} \cdot \mathbf{E}^{ext} = \frac{-ikv^2}{c} \sum_{n=1}^{\infty} \sum_{m=-n}^n m j_n(k\mathbf{r}) Y_{mn}(\Omega_{\mathbf{r}}) \phi_{mn} \quad (6.7)$$

Comparison with (6.2) yields the expansion coefficient \tilde{a}_{mn} . \tilde{b}_{mn} can be obtained by similar reasoning that we will omit here and we refer the reader to Appendix B of [103] for the details. Finally, the SVWF expansion coefficients for the electric field caused by

an electron moving at velocity v along a straight line trajectory are given by

$$a_{mn} = \frac{-4\pi ikv}{c^2} \frac{mA_{mn}}{n(n+1)} K_m \left(\frac{\omega b}{v\gamma} \right) e^{im\phi_0 + i\omega z_0/v}, \quad (6.8a)$$

$$b_{mn} = \frac{-2\pi ik}{c\gamma} \frac{B_{mn}}{n(n+1)} K_m \left(\frac{\omega b}{v\gamma} \right) e^{im\phi_0 + i\omega z_0/v}, \quad (6.8b)$$

$$A_{mn} = \sqrt{\frac{2n+1}{\pi} \frac{(n-|m|)!}{(n+|m|)!}} (2|m|-1)!! \frac{i^{|m|}}{v} \left(\frac{c}{v\gamma} \right)^{|m|} C_{n-|m|}^{(|m|+1/2)} \left(\frac{c}{v} \right), \quad (6.8c)$$

$$B_{mn} = A_{m+1,n} \sqrt{(n+m+1)(n-m)} - A_{m-1,n} \sqrt{(n-m-1)(n+m)}, \quad (6.8d)$$

where (b, ϕ_0, z_0) are the cylindrical coordinates of the electron at $t = 0$. The evaluation of the coupling integral (6.6) resulting in

$$\phi_{mn} = \frac{4\pi}{c} A_{mn} e^{im\phi_0 + i\omega z_0/v} \quad (6.9)$$

is presented in [103]. The expansion of the Green function (6.4) is valid only for $|\mathbf{r}| < |\mathbf{r}_e(t)|$, i.e. the above expression for the incident field is valid only inside a sphere of radius $\min_t |\mathbf{r}_e(t)|$.

Discussing the electromagnetic field caused by the moving electron in terms of these expansion coefficients is not very vivid and we postpone the discussion to Sec. 7.1, where we derive the electric field as a function of time from the Liénard-Wiechert potentials. Nevertheless, we obtain some information about the field. While the dependence on the electron velocity v is non-trivial, the impact parameter b only enters the coefficients in the argument of the modified Bessel function $K_m(x)$. These functions decay exponentially with increasing argument x , such that we expect a similar behaviour for the expansion coefficients.

6.2 Calculation of the Loss- and Cathodoluminescence-Probability

The calculation of the loss probability (5.3) and CL probability (5.6) is done by directly plugging in the SVWF expansion of the scattered field (3.43) into the respective expressions. For the loss probability, this results in

$$P(\omega) = \frac{2e}{\hbar\omega} \int_{-\infty}^{+\infty} dt \Re \left\{ \mathbf{v}_e \cdot \boldsymbol{\mathcal{E}}^{ind}(\mathbf{r}_e(t), \omega) e^{-i\omega t} \right\} \quad (6.10)$$

$$= \sum_{m,n} \frac{2e}{\hbar\omega} \int_{-\infty}^{+\infty} dt \Re \left\{ \mathbf{v}_e \cdot (f_{mn} \mathcal{M}_{mn}^3(k\mathbf{r}_e(t)) + g_{mn} \mathcal{N}_{mn}^3(k\mathbf{r}_e(t))) e^{-i\omega t} \right\}. \quad (6.11)$$

Again, we encounter integrals of the SVWF along the electron trajectory similar to the one in Eq. (6.6). Due to the sign reversal in the phase factor $e^{-i\omega t}$ in the above equation, we obtain A^* instead of A for the first integral. We finally obtain¹

$$P(\omega) = \sum_{m,n} K_m^2 \left(\frac{\omega b}{v\gamma} \right) \left[\frac{mv}{\pi\omega^2} \Re \left(A_{mn}^* e^{im\phi_0 + i\omega z_0/v} f_{mn} \right) + \frac{c}{2\pi\omega^2\gamma} \Re \left(B_{mn}^* e^{im\phi_0 + i\omega z_0/v} g_{mn} \right) \right]. \quad (6.12)$$

The CL probability in any direction is obtained from Eq. (5.6) where we have integrated over the angles ϑ, φ to obtain

$$P_{rad}(\omega) = \frac{1}{4\pi^2 k^3} \sum_{m,n} n(n+1) \left[|f_{mn}|^2 + |g_{mn}|^2 \right]. \quad (6.13)$$

The far-field expressions for the electric field can be directly calculated by using the far-field expressions for the SVWF. Thus, we are also able to calculate the angle-resolved CL probability according to Eq. (5.10).

6.3 Results

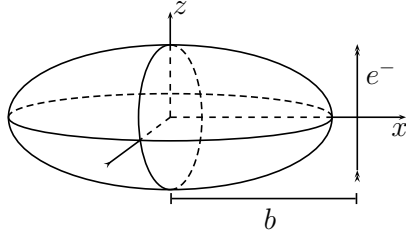


Figure 6.1: General setup for EELS calculation. The scatterer is located at the origin, the electron hits it with an impact parameter b and travels along the z -direction at velocity v . Here, the prolate spheroid is depicted, but we use the same coordinate system for all calculations.

We are now able to use the T-Matrix method to obtain results for the loss probability (EELP), the CL probability (CLP) and the far-field pattern of the emitted radiation. To begin our discussion, we start with spherical particles and discuss the influence of different parameters on the spectra before discussing spheroidal particles and a sphere dimer.

The size of the particles is chosen to correspond to sizes of particles encountered in the experiments listed in Tab. 5.1, which are in the order of 10 nm, typical materials are silver and gold. In principle, the T-Matrix method allows us to use measured datasets,

¹Note that the i^{-l} in Eqns. (27) and (28) in [103] should read i^l

like e.g. for gold or silver by Johnson and Christy [22], for the permittivity. Nevertheless, we use a simple Drude model with parameters to approximate the permittivity of gold in our discussion. The plasma energy is $\hbar\omega_p = 9.073\text{ eV}$ and the damping constant is $\hbar\gamma = 0.071\text{ eV}$ (cf. Sec. 2.4.4). The resulting spectra show distinct peaks for the eigenmodes which is advantageous for our discussion as it also allows to see how the eigenmodes contribute to the spectra and how the T-Matrix method reproduces these contributions. For comparison, we will also include spectra for the Johnson and Christy permittivity. We always assume the particle to be located in vacuum. The impact parameter is always chosen such that we have a distance of 0.5 nm between the particle surface and the electron trajectory. The electron trajectory is always contained in the x - z -plane and we indicate the location of the excitation relative to the particle in the graphs. The velocity of the electron is chosen to be $0.3c$, corresponding to 50 keV initial energy. All calculations were done for at least 300 points in the respective frequency interval to obtain smooth spectra. We will use a dimension-less quantity for the losses in the spectra. Instead of the Energy loss ΔE , we choose the energy loss $\Delta E = \hbar\omega$ over the plasma energy $\hbar\omega_p$, resulting in ω/ω_p . We do this in order to indicate that we study a Drude model material, where appropriate we will give the energy loss in units of electronvolt.

6.3.1 Spherical Particle

Spherical particles are an interesting model system to study different aspects of EELS and the T-Matrix method. For spherical particles, the Spherical Vector Wave Functions (SVWF) correspond to the eigenmodes of the particle. Thus, the expansion orders $n = 1, 2, \dots$ correspond to the dipole, quadrupole, etc. mode of the particle. We begin our discussion with the influence of the maximum expansion order used in the T-Matrix method.

Maximum Expansion order

The crucial parameter for convergence in the T-Matrix method is the truncation index N_r . For conventional Mie theory estimates for a minimal value of N_r exist, cf. Sec. 3.1.6, however the excitation by the moving electron encountered in EELS is spectrally broad and thus, we expect that more multipoles are required for convergence. Figure 6.2 shows the EEL and CL probability of a spherical particle for different maximum values of N_r . As this is the very first example for such a spectrum, we will discuss it more detailed. We see that the EEL spectrum shows distinct peaks for several energy losses. As mentioned above, these peaks indicate the eigenmodes of the particle and the respective eigenfrequencies. The eigenmodes of the particle are influenced by both, the particle shape and the permittivity of the particle. A huge number of eigenmodes contribute to the EELP indicating that the electron excites a broad spectrum of eigenmodes in the near-field. While the first few multipoles are clearly separated, the higher order multipole contributions sum up to a broad shoulder at the high-frequency end of the spectrum. This tells us that the contribution of the multipoles decrease with increasing multipole order

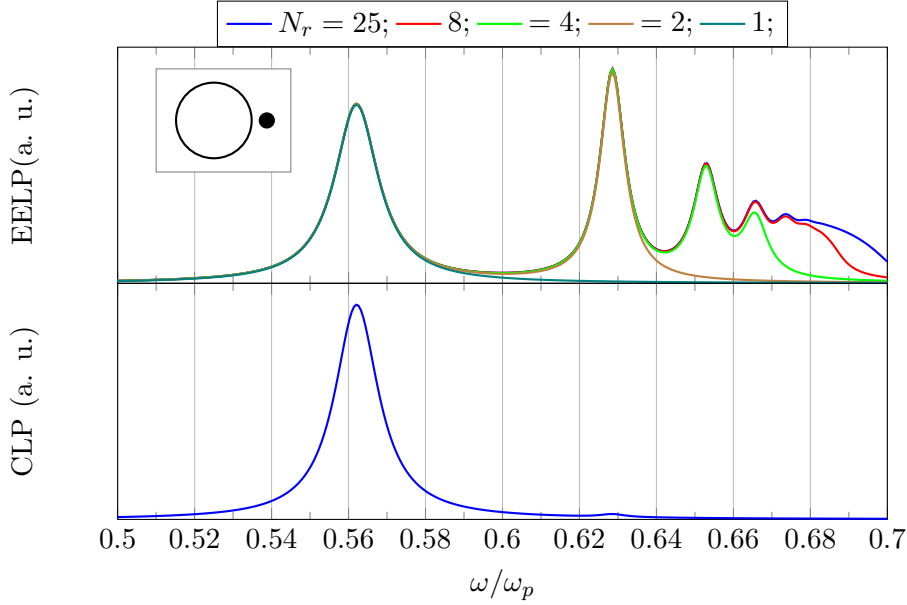


Figure 6.2: EEL (top) and CL (bottom) probability for a 10 nm sphere for different maximum expansion orders. While a huge number of multipoles contribute to the EELP, the CLP is mostly determined by the dipole contribution plus a small quadrupole contribution at around $0.63\omega_p$.

and that the eigenfrequencies increase and are more closely spaced, which actually is a consequence of the Drude model we used.

The cathodoluminescence probability (CLP), in contrast, is dominated by the dipole contribution. While the EELP is dominated by the near-field and evanescent fields, the CLP is a far-field quantity and indicates the coupling of the excited eigenmodes to the far-field, i.e. propagating electromagnetic radiation. Effectively, the particle acts like an antenna, mediating a coupling of the electron's localized field to the far-field.

Coming back to the influence of the truncation index N_r , we have seen that due to the Drude model the contribution of the higher order multipoles $n > 8$ is small and we might neglect it here. For the following calculations we will use $N_r = 12$ which is sufficient to get convergence for the first few multipoles. Where necessary we will check the spectra for different values of N_r to check for convergence.

Particle Sizes

We now want to study the influence of the particle size on the spectra. Figure 6.3 shows spectra for spheres of radius 10 nm – 20 nm. All other parameters are unaltered. Regarding the EELP, we see that with increasing radius

- the eigenfrequencies shift to the red
- the red-shift is larger for the lower order multipoles

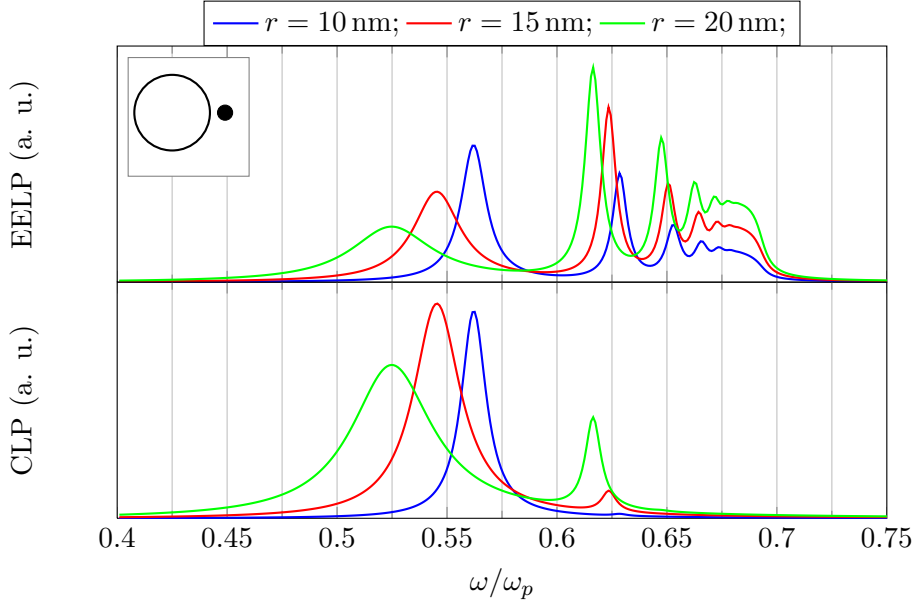


Figure 6.3: EEL (top) and CL (bottom) probability for spheres of different radius. With increasing radius the eigenmodes shift to the red and the contribution of higher order modes increases. In case of the CL, this leads to a considerable contribution from the quadrupole mode for the $r = 20$ nm sphere.

- the contribution of the higher order multipoles increases

The red-shift can be understood intuitively, when considering the plasmon resonances to be standing waves at the particle surface. With increasing radius the circumference increases and the resonance occurs at a longer wavelength, i.e. lower frequencies. In the CLP, we observe the same shifting behaviour of the eigenmodes, of course. However, for the $r = 10$ nm sphere, only the dipole contributes to the spectrum. With increasing radius, we see that the quadrupole also yields a significant contribution.

Electron velocity

In Sec. 6.1 we have seen that the electric field expansion coefficients depend on the electron velocity v in a non-trivial way. We now study the impact of the electron velocity on the EELP and CLP. Figure 6.4 shows the spectra for a $r = 15$ nm sphere for different electron velocities v . Again, all other parameters are as mentioned above. As the peaks in the spectra correspond to the eigenmodes which do not depend on the excitation, we observe no spectral shift of the peaks. We see, however, that the contribution to both, EELP and CLP decrease for increasing electron velocity. Intuitively, the interaction time between electron and particle is shorter and thus, the probability for an excitation decreases. For this reason, the electron velocity is chosen small in CL experiments as compared to EELS experiments, cf. Tab. 5.1 in Sec. 5.3. The intensities of the emitted

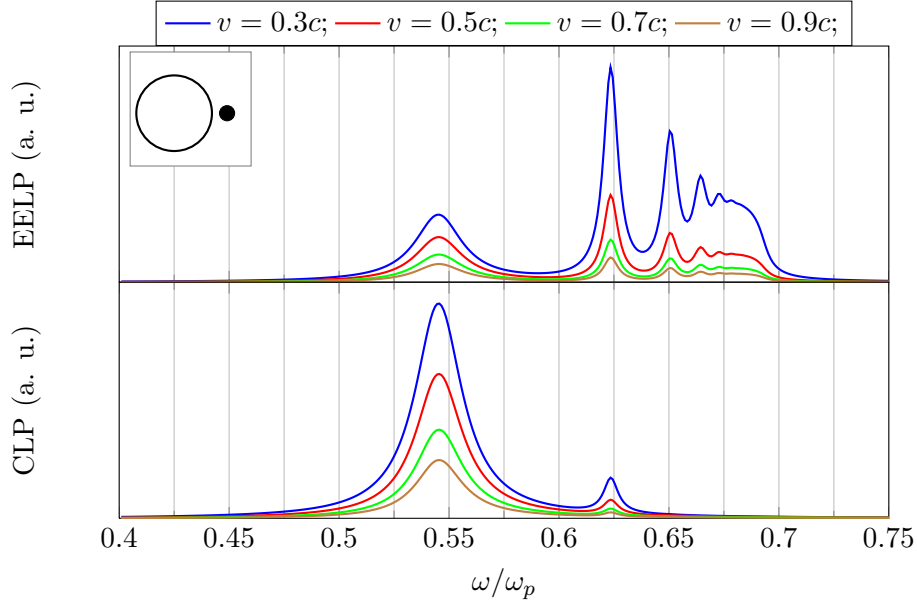


Figure 6.4: EEL (top) and CL (bottom) probability for a $r = 15$ nm sphere for different electron velocities. For increasing velocities both, the EEL and CL amplitudes decrease.

radiation are extremely small and using slow electrons, the increased probability also increases the intensities making it easier to measure.

Far-field Radiation Patterns

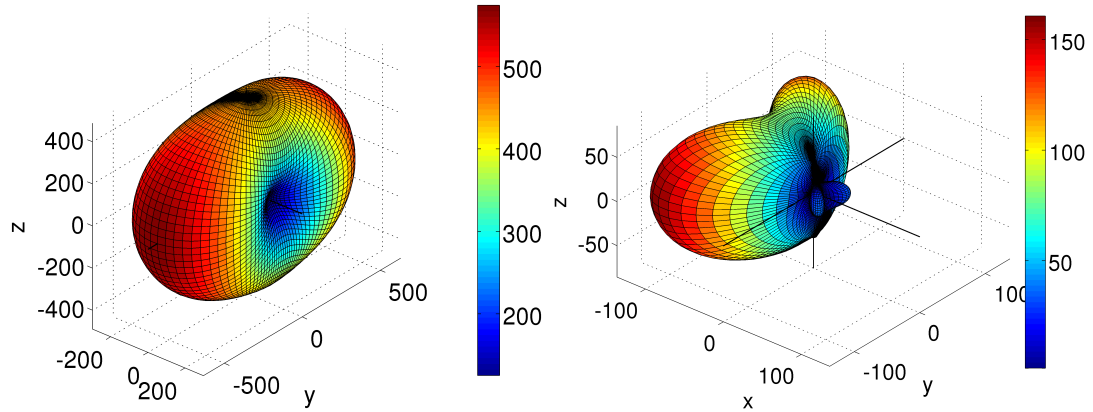


Figure 6.5: Far-field pattern $|\mathcal{E}_\infty|^2$ for the $r = 15$ nm sphere at the (a) dipole and (b) quadrupole resonance. Both plots are in the same arbitrary units.

In Sec. 5.3 we mentioned that in CL experiments the angular distribution of the emit-

ted radiation can be measured. As alluded to in Sec. 6.2 the far-field radiation pattern can be evaluated in the T-Matrix formalism, which corresponds to the angular distribution of the emitted radiation. We study the far-field pattern for a $r = 15$ nm sphere and an electron velocity of $v = 0.3c$ in Fig. 6.5. It shows the angular distribution at the dipole and quadrupole eigenfrequencies. Clearly, the angular distribution of the fields correspond to those of a radiating dipole and quadrupole, respectively. We see that the moment of the dipole is parallel to the x -axis and shows a slight asymmetry. The asymmetry of the quadrupole is much more pronounced and the radiation is emitted preferably to the far side of the sphere, i.e. the negative x -direction. This can be understood, if one considers the asymmetry of the excitation field of the electron. It is shifted from the origin along the x -axis by the impact parameter, while the sphere is located at the origin. Thus, we may expect a certain asymmetry.

Retardation effects

In Sec. 5.4.1 we have mentioned results that were obtained for certain particle shapes using the quasi-static approximation (QSA), which neglects retardation effects, cf. Sec. 2.1.8. We already presented results including retardation above, and we now want to compare them with QSA results for spherical particles. In QSA the loss probability for a sphere with radius r evaluates to [99]

$$P_{QSA}(\omega) = \frac{4}{\pi v^2 r^2} \sum_{m,n}^{\infty} \frac{2 - \delta_{0,m}}{(n+m)!(n-m)!} \left(\frac{\omega a}{v}\right)^{2n} K_m^2\left(\frac{\omega b}{v}\right) \Im \alpha_n(\omega) \quad (6.14)$$

with the *multipole polarizability*

$$\alpha_n(\omega) = \frac{\varepsilon(\omega) - 1}{\varepsilon(\omega) + (n+1)/n} a^3. \quad (6.15)$$

Comparison with the result including full retardation (6.12) shows an important difference. In the QSA result, the spectral position of the modes (and thus the peaks in the EEL spectra) are only determined by the permittivity of the particle $\varepsilon(\omega)$, but not by the size of the particle. This is reasonable as the QSA assumes an infinite speed of light and assumes the incident field outside the particle to be constant. In the full retardation result (6.12) the particle size enters via the T-Matrix that is used to calculate the coefficients f_{mn}, g_{mn} . This effect is clearly visible in Fig 6.6. Already for particles of 10 nm size, the QSA fails to correctly reproduce the spectral position of the dipole mode (blue curves). We have seen that increasing the particle size causes a red-shift of the resonances in the discussion above. This means that the deviations between the QSA results and the full retardation results increase with increasing particle size, too. This is apparent from the curves for a 20 nm sphere (red curves in Fig. 6.6). In recent experiments, the particles are usually larger than 20 nm and we can expect the deviation of the QSA results to the full retardation results to be even more dramatic. Therefore, retardation effects clearly have to be taken into account when calculating EEL spectra, especially in the context of the interpretation of experiments. It is necessary to go be-

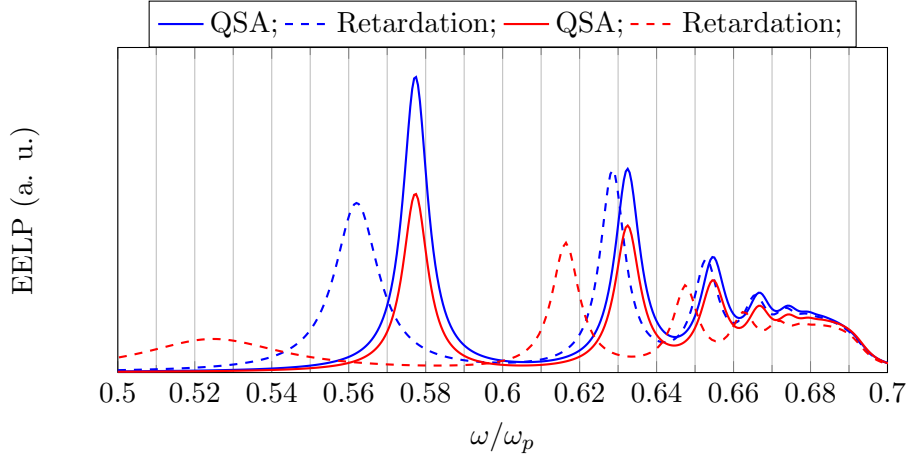


Figure 6.6: EEL spectra in quasi-static approximation (QSA, solid lines) and including full retardation (dashed lines) for a 10 nm sphere and electron velocity $v = 0.3c$ (blue) and a 20 nm sphere with $v = 0.5c$.

yond the QSA and this also justifies the demand for results including full retardation, which, for more complicated particle shapes, can only be obtained numerically.

Influence of the Permittivity

Before proceeding to spheroidal particles, we want to discuss the influence of the permittivity. So far, we have employed a Drude model for the permittivity. As mentioned in Sec. 2.4, the data set measured by Johnson and Christy [22] is also commonly used in plasmonics calculations. We therefore employ it for our calculations of the EEL and CL spectra for gold spheres of different radius. Figure 6.7 shows the results. Here we see that increasing the radius does not cause an observable shifting of the resonances.

The EEL spectrum shows more or less constant values for frequencies higher than the dipole frequency. This is due to the onset of the intra-band transitions in gold observable in the imaginary part of the measured permittivity of gold in Fig. 2.4.

6.3.2 Spheroidal Particles

Spheroids are ellipsoids with two of three axes being of equal length. They can be obtained as bodies of revolution from an ellipse, resulting in prolate (oblate) spheroids, if the ellipse is revolved around the long (short) axis. We already discussed in Sec. 3.1.7, that a Mie-like approach in spheroidal coordinates is in principle possible, however the evaluation of the spheroidal harmonics is computationally too expansive. Here, methods like the T-Matrix Method are required. Due to their rotational symmetry, spheroids can be treated very efficiently as the integrals needed to evaluate the T-Matrix (3.60) reduce to integrals over the generatrix of the spheroid. As outlined in Sec. 3.2.2, we are subject to the constraint that the expansion of the scattered field is valid only

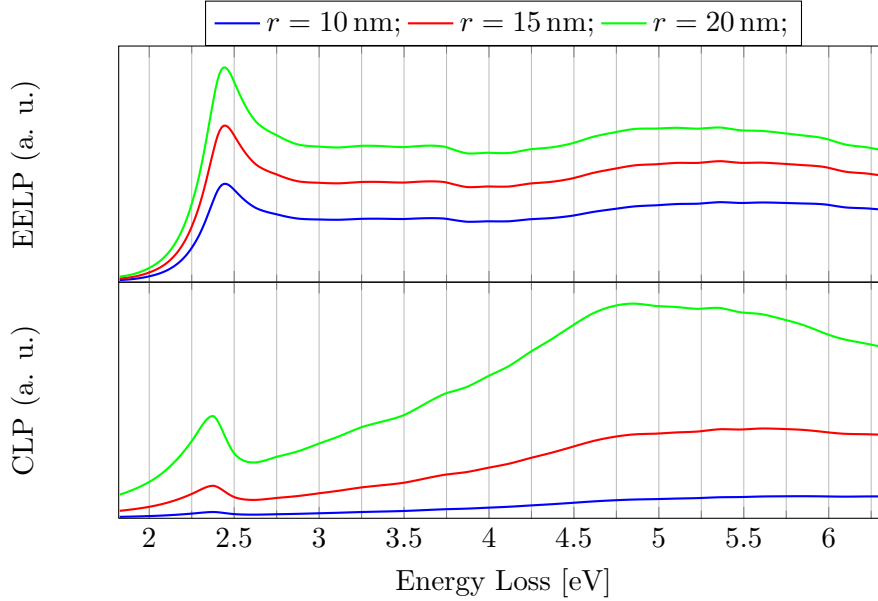


Figure 6.7: EEL and CL spectra for sphere of different radius with Johnson and Christy permittivity data for gold [22]. The dependence on the sphere radius is less pronounced than for a Drude material. The intra-band transitions cause a constant loss probability above 2.5 eV.

outside the smallest sphere circumscribing the scatterer. Obviously, this imposes a restriction for spheroids, such that the impact parameter has to be larger than the longest semi-axis of the spheroid. We choose the spheroid to have an aspect ratio of 1 : 1.5 and to have the same volume as a 15 nm sphere. This results in semi-axes length of $r_x = 19.66$ nm, $r_y = r_z = 13.10$ nm. We excite the spheroid at the end of the long half-axis with a surface-to-electron distance of 0.5 nm as indicated in the inset of Fig. 6.8. As we have changed the particle geometry considerably, we plot the spectra for different values of the truncation index N_r . Using $N_r = 25$ we have achieved sufficient accuracy. The EELP shows a similar behaviour as for the spherical particle. The first few eigenmodes are well separated, the higher order eigenmodes sum up to a broad shoulder at the high-frequency end of the spectrum. The lowest eigenmode of the spheroid is found at $\omega = 0.46\omega_p$ which is lower as compared to the 15 nm sphere at $\omega = 0.55\omega_p$ in Fig. 6.3. For the spherical particle, the eigenmodes were exactly the multipoles. This correspondence is not valid for spheroid anymore, therefore we need to further characterize the eigenmodes. We cannot directly map the eigenmodes by scanning the electron beam across the particle, because the electron must remain outside the smallest circumscribing sphere. Therefore, we study the far-field patterns to gain some insight in the eigenmodes. Figure 6.9 shows the far-field patterns at the respective resonance frequencies indicated in Fig. 6.8. We see that pattern 6.9(a) possesses a dipolar radiation characteristic where the dipole moment is aligned along the long axis of the spheroid,

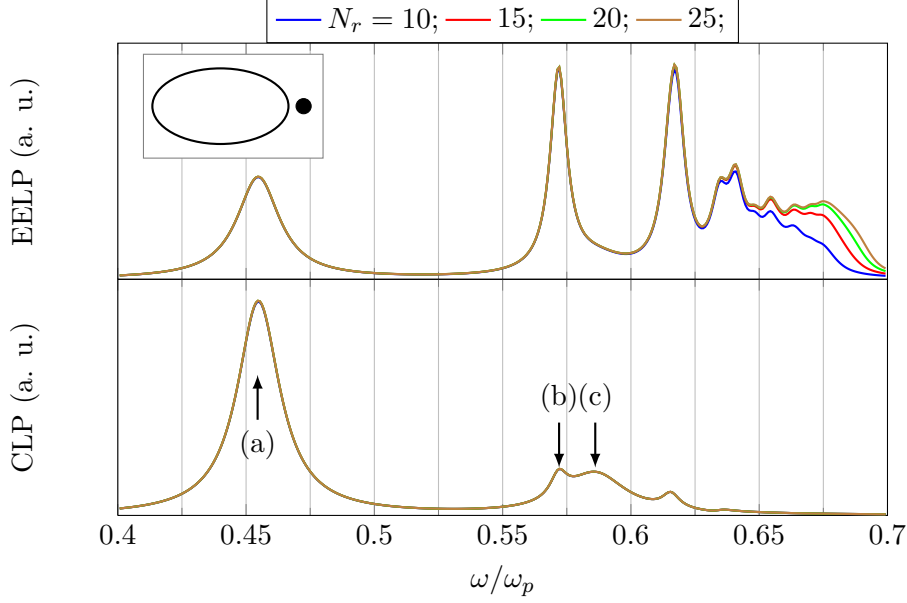


Figure 6.8: EEL and CL spectra for a prolate spheroid with aspect ratio 1.5 and the same volume as a 15 nm sphere. The CL spectrum has contributions from higher order multipoles. We plot the far-field pattern for the indicated peaks in Fig. 6.9.

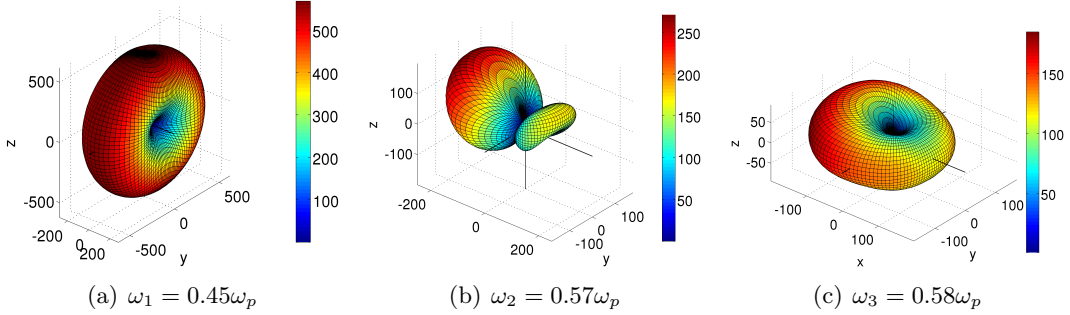


Figure 6.9: Far-field amplitude $|\mathbf{E}_\infty|^2$ as a function of the direction for the spheroid at frequencies indicated in Fig. 6.8. All plots are in the same arbitrary units. We see a dipolar characteristic for patterns (a) and (c) and a quadrupolar one for pattern (b).

i.e. the x axis. This is the same behaviour as for the lowest eigenmode of the spherical particle. Pattern 6.9(c) has the same dipolar characteristic, but the dipole moment is now aligned along the z axis, which is the short axis of the spheroid parallel to the electron trajectory. Comparing the frequencies of these two dipolar modes at $\omega_1 = 0.45\omega_p$ and $\omega_3 = 0.58\omega_p$ with the dipolar mode of the sphere at $\omega_s = 0.54\omega_p$, we see that

$\omega_1 < \omega_s < \omega_3$. This behaviour can be explained by again thinking of the eigenmodes as standing surface plasmon waves. For the modes depicted in pattern 6.9(a) and 6.9(c), the circumference is given by an ellipse with semi-axes r_x, r_z and a circle with radius r_z , respectively. This is larger and smaller than the sphere circumference, respectively. We therefore expect the resonances to be at lower and higher frequency, respectively. This behaviour is well known for spheroids from optical spectroscopy, where the two dipole modes can be addressed by using linearly polarized light with polarization along the respective axis of the spheroid, which has been already been discussed in Sec. 4.1. Pattern 6.9(b) has a quadrupolar characteristic with contributions from the dipolar pattern 6.9(b) which is already expected from the CL probability in Fig. 6.8 due to the broad peak (c).

6.3.3 Dimers of Spheres

Beyond single particle properties, experiments already study the coupling behaviour of particles with EELS as mentioned in Tab. 5.1. So far, we have only studied single particles using the T-Matrix, however, the method can also be applied to particle systems. To illustrate this, we will now study a dimer of nominally identical spheres. To that end, we have to introduce the necessary extensions of the T-Matrix formalism.

Translation and Rotation of the Scatterer

The key element to the treatment of particle systems in the T-Matrix formalism are the *addition theorems for the Spherical Vector Wavefunctions (SVWF)* [37] and the multiple scattering problem. The addition theorems allow for a translation and rotation of a SVWF expansion from one coordinate system 1 with origin \mathbf{R}_1 to some coordinate system with origin \mathbf{R} . A rotation of the coordinate system only affects the angular part of the SVWFs, i.e. the Spherical Harmonics $Y_{mn}(\vartheta, \varphi)$. The Spherical Harmonics for given n are basis functions of an irreducible representation of the group of rotations $SO(3)$. For this reason, the spherical harmonics transform under rotations as

$$Y_{mn}(\vartheta, \varphi) = \sum_{m'=-n}^n a_{nm'} Y_{m'n}(\vartheta_1, \varphi_1). \quad (6.16)$$

Consequently, the rotated SVWFs $\mathcal{M}_{mn}(r, \vartheta, \varphi)$ [$\mathcal{N}_{mn}(r, \vartheta, \varphi)$] for given n can also be written as a linear combination of SVWFs $\mathcal{M}_{m'n}(r, \vartheta_1, \varphi_1)$ [$\mathcal{N}_{m'n}(r, \vartheta_1, \varphi_1)$] of the same n . For our truncated expansion, we can express this with the help of the *rotation matrix*

$$\begin{pmatrix} \mathcal{M}_{mn}^p(k\mathbf{r}) \\ \mathcal{N}_{mn}^p(k\mathbf{r}) \end{pmatrix} = \underline{\mathcal{R}}(\alpha, \beta, \gamma) \begin{pmatrix} \mathcal{M}_{mn}^q(k\mathbf{r}_1) \\ \mathcal{N}_{mn}^q(k\mathbf{r}_1) \end{pmatrix}, \quad (6.17)$$

where α, β, γ are the Eulerian angles characterizing the rotation.

For translations, things are more involved and expressing the rotated and translated SVWF \mathcal{M}_{mn} or \mathcal{N}_{mn} requires a linear combination of *both* SVWFs $\mathcal{M}_{m'n'}$ and $\mathcal{N}_{m'n'}$ where the sum now also runs over n' . For the primed indices, we again have to truncate

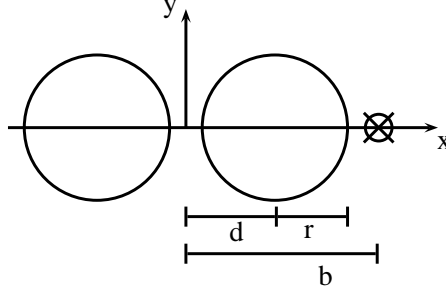


Figure 6.10: Sphere dimer geometry in top-view. The crossed circle indicates the electron trajectory.

the sum over n' at some maximum value N'_r , which has to be sufficiently large. Ultimately, the relation between the SVWF expansions can be expressed with the help of the matrices

$$\begin{pmatrix} \mathcal{M}_{mn}^p(k\mathbf{r}) \\ \mathcal{N}_{mn}^p(k\mathbf{r}) \end{pmatrix} = \mathcal{T}^{pq}(k\mathbf{R}_0) \begin{pmatrix} \mathcal{M}_{mn}^q(k\mathbf{r}_1) \\ \mathcal{N}_{mn}^q(k\mathbf{r}_1) \end{pmatrix}, \quad (6.18)$$

where (p, q) is one of $(1, 1)$, $(3, 3)$, $(3, 1)$ and $\mathbf{R}_0 = \mathbf{R} - \mathbf{R}_1$.

Multiple Scattering Problem

So far, we have used the T-Matrix to calculate the scattered field for the incident field of the moving electron. The incident field, however, is not restricted to some external excitation, but could also be caused by another scatterer. We illustrate this for the example of the sphere dimer. We can construct the T-Matrices of the two spheres by calculating the T-Matrix \mathbf{T}_0 for a sphere located at the origin and using the translation matrices to move the SVWF expansion to the new origin $\mathbf{R}_{1/2} = (\pm d, 0, 0)$, the coordinate systems of which we denote with 1 and 2 respectively. We thus obtain the T-Matrices of the two spheres \mathbf{T}_1 and \mathbf{T}_2 . The incident field for sphere 1 is the field of the electron plus the field scattered from sphere 2 and vice-versa. Expressing this in terms of the T-Matrices and solving for the total scattered field yields the T-Matrix of the particle system which in our case evaluates to

$$\begin{aligned} \mathbf{T}_0 = & \mathcal{T}_{01}^1 \mathbf{T}_1 (\mathbf{I} - \mathcal{T}_{12}^3 \mathbf{T}_2 \mathcal{T}_{21}^3 \mathbf{T}_1)^{-1} (\mathbf{I} + \mathcal{T}_{12}^3 \mathbf{T}_2 \mathcal{T}_{21}^1) \mathcal{T}_{10}^1 \\ & + \mathcal{T}_{02}^1 \mathbf{T}_2 (\mathbf{I} - \mathcal{T}_{21}^3 \mathbf{T}_1 \mathcal{T}_{12}^3 \mathbf{T}_2)^{-1} (\mathbf{I} + \mathcal{T}_{21}^3 \mathbf{T}_1 \mathcal{T}_{12}^1) \mathcal{T}_{20}^1, \end{aligned} \quad (6.19)$$

where the translation matrix \mathcal{T}_{ij}^p translates the SVWFs of kind p from coordinate system i to system j . This expression can easily be generalized to a larger number of scatterers that also can have arbitrary rotation. However, we restrict ourselves to the sphere dimer.

Application to the Sphere Dimer

We choose the spheres to have 10 nm radius and shift them along the x axis with $d = \pm 10.5$ nm to obtain a 1 nm gap between the spheres. The permittivity is the same Drude model as in the previous calculations. The impact parameter is chosen to be 21 nm. Using the formalism outlined above, we are able to calculate the T-Matrix for the sphere dimer and obtain EEL and CL spectra. Figure 6.11 shows the spectra for different maximum expansion orders N_r . Due to the solution of the multiple scattering problem the convergence behaviour is now different from the examples above. We see, however, that using $N_r = 20$ is sufficient to achieve reasonable accuracy. For the truncation index of the translation matrices we have chosen $N'_r = N_r$. The spectra for a single $r = 10$ nm sphere have been shown in Fig. 6.3 and in comparison we see that the dimer possesses a resonance at around $0.41\omega_p$, which is at lower frequency than for the single sphere, the dipole resonance of which occurred around $0.56\omega_p$. Interestingly, the CLP

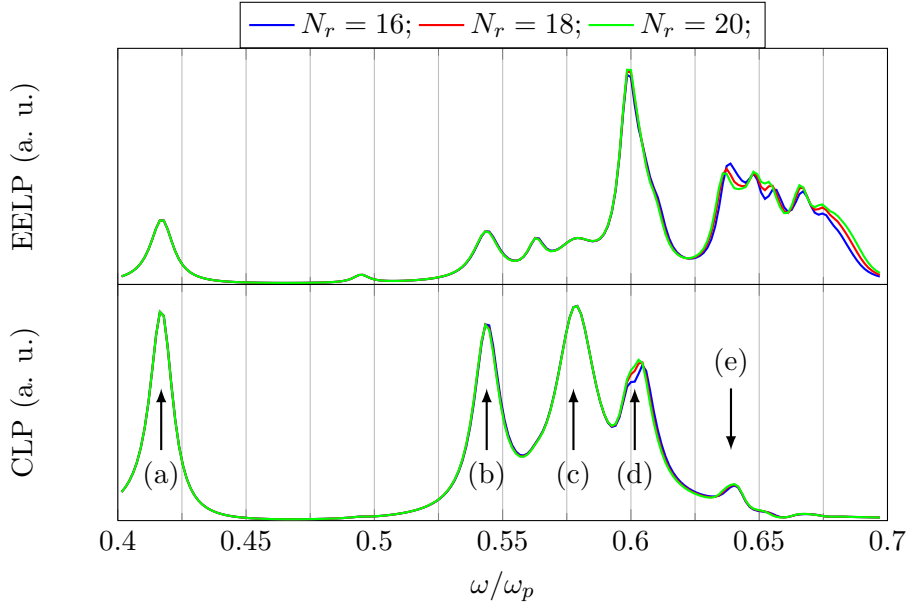


Figure 6.11: EEL (top) and CL (bottom) spectra for the sphere dimer for different maximum expansion orders N_r . In contrast to the single sphere, the dimer shows a significant CL signal for higher-order modes. The arrows indicate the frequencies at which far-field patterns shown in Fig. 6.12 are calculated.

of the dimer shows contributions from higher order modes as well. This is in contrast to the single sphere, the CLP of which was dominated by the dipole contribution. To further investigate the radiation emitted by the electron-excited dimer, Fig. 6.12 shows the far-field patterns of the scattered field at the frequencies indicated in Fig. 6.11. Pattern 6.12(a) and 6.12(c) exhibit dipolar characteristic with moment aligned parallel to the dimer-axis and the electron trajectory, respectively. While all peaks in the CLP have a similar amplitude, pattern 6.12(d) shows a much more directed emission of radiation

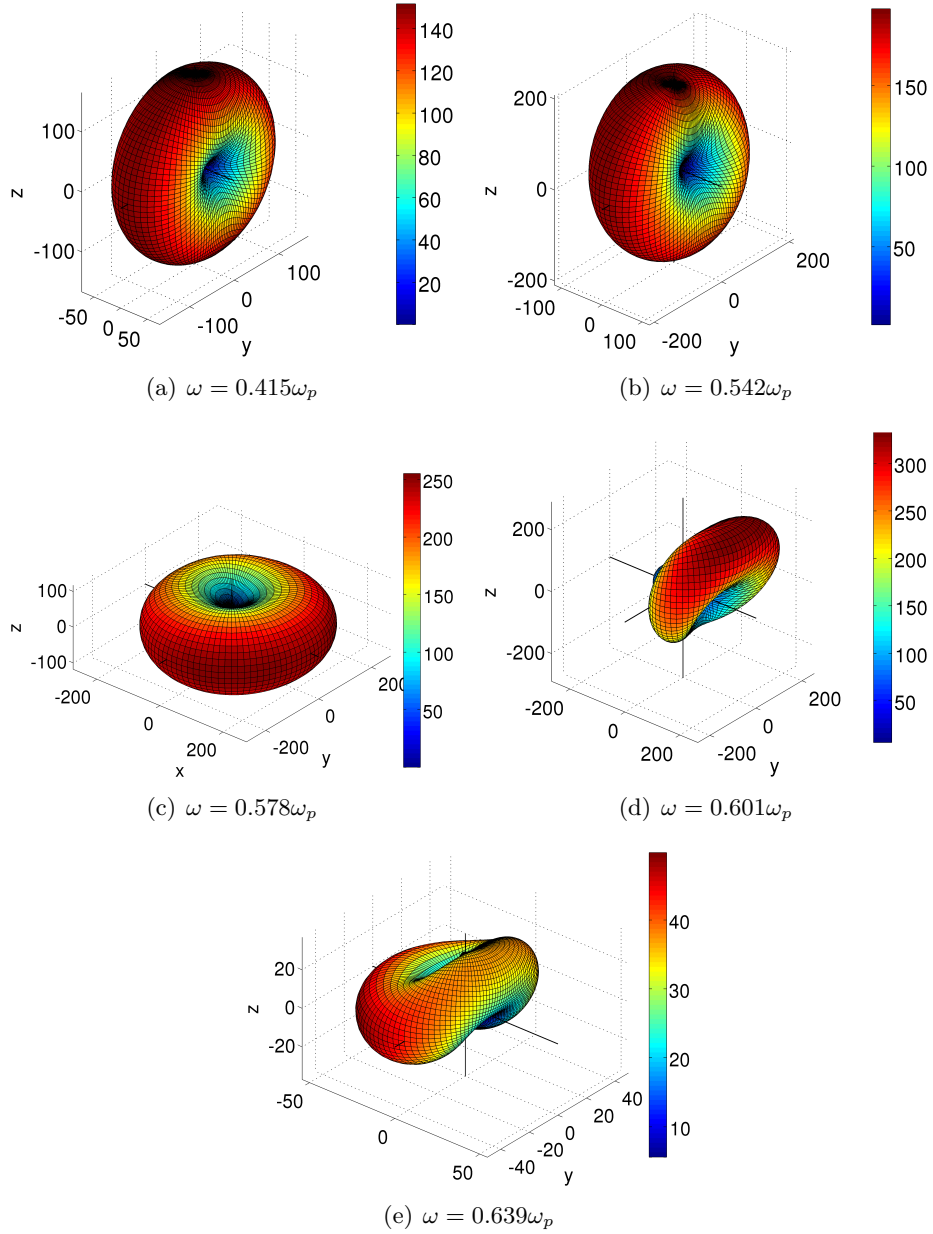


Figure 6.12: Far-field amplitude $|\mathbf{E}_{s,\infty}|^2$ as a function of the direction for the sphere dimer at frequencies indicated in Fig. 6.11. For details see the text.

than the other ones with most of the radiation being emitted to the positive x - y -direction. This means that here, it is mostly emitted towards the electron beam. Thinking of the dimer as a nano-antenna, we see that we can increase the directivity of the far-field emission just as it is done in radio frequency antenna technology. This idea was already applied to nano-antennas [7] and we will come back to it in Sec. 7.5.

For the dimer there are restrictions regarding possible electron trajectories, too. As the expansion of the electron field (6.8) is only valid for $|\mathbf{r}| < b$, where b is the impact parameter, we can only excite the dimer with an impact parameter $b > 20.5$ nm in our case. This prohibits to study some of the modes of the dimer in more detail. We will, however, come back to the sphere dimer and study the modes in more detail using the Discontinuous Galerkin Time-Domain method in Sec. 7.4.

6.4 Conclusion

We have applied the T-Matrix method, which is well established in optical scattering calculations, to the problem of EEL and CL spectroscopy experiments. Results for spherical particles have been presented and the influence of the important parameters, like sphere size and electron velocity, has been discussed. The far-field patterns of the excited modes have been computed and discussed. They were in particular useful for the discussion of the prolate spheroid, where we could identify the two dipolar modes along the long and short half-axes. Using a multiple scattering formalism, we were able to treat a sphere dimer. While particles of almost spherical shape are preferred, the method is not restricted to such particles.

In summary, we have shown that the T-Matrix method is well-suited for EEL and CL spectroscopy simulations. The method is very efficient due to its semi-analytical approach and for particles that possess a certain symmetry, it is particularly efficient. Calculations for the spheroidal particle, e.g., required only 0.8 s per frequency. The Null-Field Method as well as the derivation of the expansion coefficients of the incident field restrict the choice of electron trajectories. We will come back to these restrictions and how they can possibly be overcome in the conclusion of this thesis.

7 The Discontinuous Galerkin Time-Domain Method for Electron Microscopy

In the preceding chapter, we have used the T-Matrix Method to calculate the electron energy loss probability and the cathodoluminescence probability. The method has proven to be efficient, however there are restrictions concerning the electron trajectory and as well as the particle shape. In this chapter, we are going to apply the Discontinuous Galerkin Time-Domain Method, introduced in Sec. 3.3, to the probability calculation. It comes with a flexible spatial discretization and no a priori restrictions for the electron trajectory. Also, it has the advantage of being a time-domain method, which will allow us to directly observe the time evolution of the induced field. We will discuss the incident field as a function of space and time, before we discuss the influence of some important parameters on the results. Then, we will compare time-domain results for spheroids with the T-Matrix frequency-domain results to check the accuracy of the time-domain approach. Finally, we will exploit the advantages of the method to study the Sierpinski triangle and a pair of nano-antennas.

7.1 Electron Excitation

The Total-Field/Scattered-Field formalism detailed in Sec. 3.3.5 enables us to inject a given electromagnetic field into the computational domain. Likewise, the Scattered-Field formalism allows to compute the field caused by a scatterer for a given incident electromagnetic field. Therefore, we have to calculate the field caused by a single moving electron in order to simulate EELS experiments using the DGTD.

We start by considering the charge and current distribution for a single moving electron

$$\rho(\mathbf{r}, t) = \delta(\mathbf{r} - \mathbf{R}(t)), \quad (7.1a)$$

$$\mathbf{J}(\mathbf{r}, t) = \dot{\mathbf{R}}(t) \rho(\mathbf{r}, t) = \dot{\mathbf{R}}(t) \delta(\mathbf{r} - \mathbf{R}(t)), \quad (7.1b)$$

where we have denoted the trajectory of the electron by $\mathbf{R}(t)$. The electromagnetic potentials $\mathbf{A}(\mathbf{r}, t)$, $\phi(\mathbf{r}, t)$ can be calculated from these expressions with the retarded Green function

$$G^{ret}(\mathbf{r} - \mathbf{r}', t - t') = \frac{1}{4\pi |\mathbf{r} - \mathbf{r}'|} \delta\left(\frac{|\mathbf{r} - \mathbf{r}'|}{c} - (t - t')\right), \quad (7.2)$$

which is obtained from the Fourier transform of (2.27). The δ -distribution introduces the retardation, i.e. any perturbation travels with the finite velocity c .

$$\phi(\mathbf{r}, t) = \frac{q}{4\pi\epsilon_0\epsilon} \int d^3r' \int dt' \frac{1}{|\mathbf{r} - \mathbf{R}(t')|} \delta\left(\frac{|\mathbf{r} - \mathbf{R}(t')|}{c} - (t - t')\right) \quad (7.3a)$$

$$\mathbf{A}(\mathbf{r}, t) = \frac{q\mu_0\mu}{4\pi} \int d^3r' \int dt' \frac{\dot{\mathbf{R}}(t')}{|\mathbf{r} - \mathbf{R}(t')|} \delta\left(\frac{|\mathbf{r} - \mathbf{R}(t')|}{c} - (t - t')\right) \quad (7.3b)$$

Due to the retardation, the t' -integrals can not be evaluated directly, but require some arguing. We define the argument of the δ -distribution as

$$f(t') = \frac{|\mathbf{r} - \mathbf{R}(t')|}{c} - (t - t') \quad (7.4)$$

and exploit that

$$\delta(f(t')) = \sum_{j=1}^n \frac{\delta(t' - t_j)}{\left|\left(\frac{df}{dt'}\right)_{t'=t_j}\right|} \quad (7.5)$$

where t_j are the n roots of $f(t')$. We evaluate the derivative in the above expression

$$\frac{df}{dt'} = 1 - \frac{1}{c} \frac{(\mathbf{r} - \mathbf{R}(t')) \cdot \dot{\mathbf{R}}(t')}{|\mathbf{r} - \mathbf{R}(t')|} \quad (7.6)$$

With $V(t') = \left|\dot{\mathbf{R}}(t')\right|$ we can estimate that

$$1 - \frac{V(t')}{c} \leq \frac{df}{dt'} \leq 1 + \frac{V(t')}{c}. \quad (7.7)$$

As we know that $V(t') < c$, we deduce that $f(t')$ is monotonous and can have no more than one root. If there is none, we would end up with the unphysical result that $\mathbf{A} \equiv 0, \phi \equiv 0$, so there must be exactly one root $t_{ret}(\mathbf{r}, t)$ which is the solution of the equation

$$t_{ret}(\mathbf{r}, t) = t - \frac{1}{c} |\mathbf{r} - \mathbf{R}(t_{ret}(\mathbf{r}, t))|. \quad (7.8)$$

We can now perform the t' -integration in (7.3) and obtain

$$\phi(\mathbf{r}, t) = \frac{q}{4\pi\epsilon_0\epsilon} \frac{1}{|\mathbf{r} - \mathbf{R}(t_{ret})| - \frac{1}{c} (\mathbf{r} - \mathbf{R}(t_{ret})) \cdot \dot{\mathbf{R}}(t_{ret})}, \quad (7.9)$$

$$\mathbf{A}(\mathbf{r}, t) = \frac{q\mu_0\mu}{4\pi} \frac{\dot{\mathbf{R}}(t_{ret})}{|\mathbf{r} - \mathbf{R}(t_{ret})| - \frac{1}{c} (\mathbf{r} - \mathbf{R}(t_{ret})) \cdot \dot{\mathbf{R}}(t_{ret})}. \quad (7.10)$$

These equations define the electromagnetic potentials \mathbf{A} and ϕ for a moving charge and are termed *Liénard-Wiechert potentials*. Due to the retardation their evaluation for general particle trajectories is quite involved. As discussed in Sec. 5.4, if incident on

some metallic target particle, the electron will induce some electric and magnetic fields at the particle which act back onto the electron. Therefore, it is subject to the force

$$\mathbf{F}_L(\mathbf{r}, t) = q\mathbf{E}_{ind}(\mathbf{r}, t) + q\dot{\mathbf{R}}(\mathbf{r}, t) \times \mathbf{B}_{ind}(\mathbf{r}, t) \quad (7.11)$$

In addition, any accelerated charged particle will emit radiation, which leads to further energy loss and therefore to a change in the state of motion of the electron. The rigorous solution would require the following steps at every time t :

1. Evaluate the fields caused by the electron
2. Evaluate the fields induced at the particle surface
3. Evaluate the force \mathbf{F}_L and energy emitted by the electron
4. Integrate the equation of motion of the electron
5. Continue with step 1

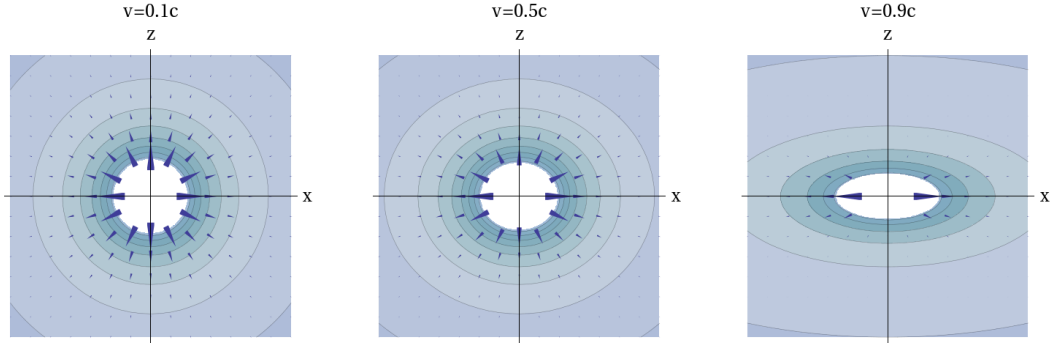


Figure 7.1: Plot of the electric field vector and equipotential lines of an electron moving along the z -direction for different velocities $v = 0.1c, 0.5c, 0.9c$. With increasing velocity, the field is compressed in the direction of travel, however it remains central.

Such coupled electrodynamic-Newtonian mechanics calculation are used, e.g., in plasma physics in so-called Particle-in-Cell simulations for a huge number of particles [104]. In principle, the same technique could be applied here for just one particle. However, the accurate description of EELS experiments does not require a rigorous solution of the equation of motion of the electron. In the derivation of the loss probability in Sec. 5.4 we have applied the no-recoil approximation, which assumes that the momentum of the electron remains unchanged. Of course, the same argument applies here and we can assume that $\dot{\mathbf{R}}(t) = \mathbf{v} = \text{const.}$, which simplifies things a lot. First of all, the trajectory of the electron is $\mathbf{R}(t) = \mathbf{v}t + \mathbf{r}_0$. This means, there is no acceleration and thus no emission of radiation from the electron. Furthermore, the Liénard-Wiechert potentials

and the resulting fields can be evaluated analytically. We obtain:

$$\mathbf{E}(\mathbf{r}, t) = \frac{q\gamma}{4\pi\epsilon_0\epsilon} \frac{(\mathbf{R}(t) - \mathbf{r})}{\left(|\mathbf{R}(t) - \mathbf{r}|^2 + (1/\gamma^2 c^2) ((\mathbf{R}(t) - \mathbf{r}) \cdot \mathbf{v})^2\right)^{3/2}}, \quad (7.12a)$$

$$\mathbf{B}(\mathbf{r}, t) = \frac{\mathbf{v}}{c^2} \times \mathbf{E}(\mathbf{r}, t), \quad (7.12b)$$

with $\gamma = 1/\sqrt{1 - (v/c)^2}$. The resulting field is still central, though it gets compressed in the direction of travel. This result is somewhat counter-intuitive as one might have expected the retardation to produce a more complicated field pattern. Figure 7.1 shows the field caused by an electron moving along the z -direction. For small velocities, the field remains almost isotropic as in the $v = 0$ case, for larger velocities, however, it gets compressed in the direction of travel more and more. This effect arises due to the retardation and the large velocity of the electron.

Alternatively, one can derive the expressions for the fields in terms of general relativity. In the eigensystem of the electron it is at rest and the field caused by the electron is the common central field from electrostatics, i.e.

$$\mathbf{E}_{el}(\mathbf{r}) = \frac{q}{4\pi\epsilon_0\epsilon} \frac{1}{|\mathbf{r}|^2} \quad (7.13)$$

and in this case, of course, $\mathbf{B}_{el} = 0$. We now can apply the Lorentz transform to calculate the field that an observer in the reference system will measure and obtain the same expressions Eq. (7.12) but by a completely different method [8].

7.2 Sphere - Discretization and Accuracy

Having the electric and magnetic field caused by the electron as a function of time and space, we are now able to use the fields in the DGTD to model Electron Energy Loss (EEL) and cathodoluminescence (CL) experiments within the no-recoil approximation. This can be done using either the Scattered-Field/Total-Field formalism (TFSF) or a pure Scattered-Field formalism (SF) as explained in Sec. 3.3.5. As we calculate in time-domain and on a finite computational domain, we have to shortly discuss how we can obtain the EEL and the CL probability, which we have so far only discussed in frequency-domain in Sec. 5.4. Apparently, we will have to perform a Fourier transform to obtain the Fourier components of the fields required in Eqns. (5.3) and (5.6). To see how we can calculate these components, we will first introduce the geometry for a typical EELS calculation for the DGTD.

The general setup is sketched in Fig. 7.2. It shows a cross-section of the computational domain that is discretized with tetrahedral elements as outlined in Sec. 3.3. The outer boundaries are equipped with PML boundaries that absorb any incident fields without reflection to simulate unbounded space (cf. Sec. 3.3.5). The dark blue region is the scattered field region (SF), the light blue region is the total field region (TF), where both, the excitation and the scattered field, are propagated. The excitation field diverges at

the electron position and to screen this divergence, the electron must be located *outside* the total field domain. This is achieved by extending the SF region to a small channel that intersects the TF region and contains the electron trajectory. This small channel can be seen in Fig. 7.2 and also in Fig. 3.6 on Page 46. Using the pure Scattered-Field (SF) formalism, we do not have to introduce such a virtual boundary in the domain. The SF formalism, however, relies on the linearity of Maxwell's equations in the entire domain, while the TFSF formalism only relies on the linearity at the virtual boundary. In the case of a non-linear material scatterer we had to use the TFSF formalism. We will restrict ourselves to linear permittivities in this thesis and we are free to use either the TFSF or the SF formalism. The small channel introduced in the TFSF setup increases the number of overall elements significantly and thus we will prefer to use the pure SF formalism in our calculations.

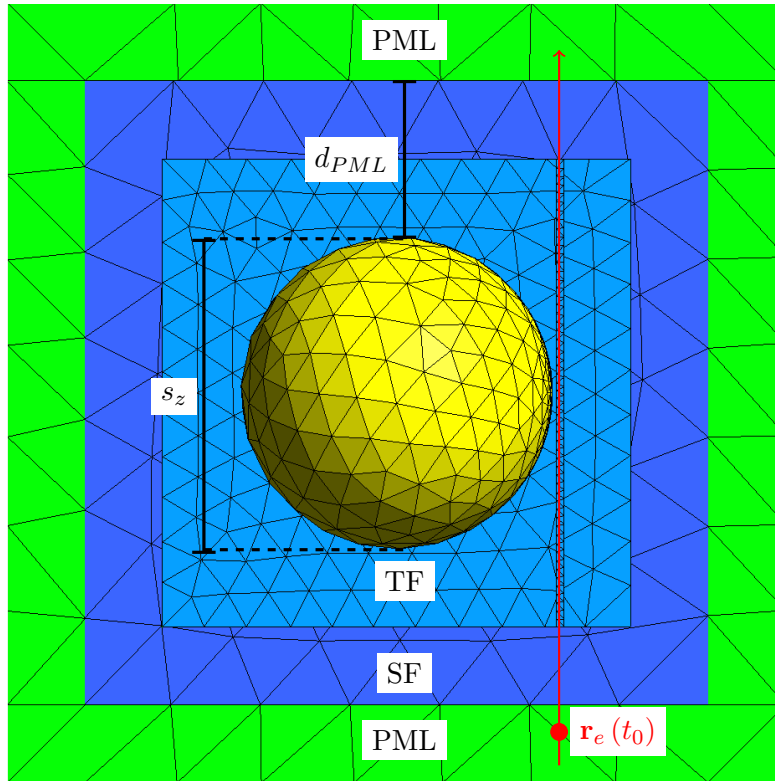


Figure 7.2: **DGTD setup for EELS.** Cross-section of Fig. 3.6. Sketch of the geometry for EELS calculation in the Total-Field/Scattered-Field formalism. The computational domain is surrounded by PML, a virtual boundary is introduced that divides the domain outside the scatterer into total field (TF, light blue) and scattered field (SF, dark blue) region. The electron trajectory as well as the initial electron position are indicated in red.

In either formalism, we directly obtain the induced field along the electron trajectory,

which is exactly the quantity needed to evaluate the loss probability (5.3). In order to perform the Fourier transform to obtain $\mathcal{E}^{ind}(\mathbf{r}_e(t), \omega)$ we will have to record the induced $\mathbf{E}^{ind}(\mathbf{r}_e(t), t)$ along the electron trajectory and perform the Fourier transform in every point. Here, the DGTD method imposes two restrictions. First, the computational domain is finite and thus we can only calculate the electric field along the part of the trajectory inside the computational domain. Second, the simulated time is finite and in order for the Fourier transform to converge, we must propagate the fields until they have decayed sufficiently. These two restrictions are no principle hurdle for the method when trying to simulate EELS on metallic nano-particles.

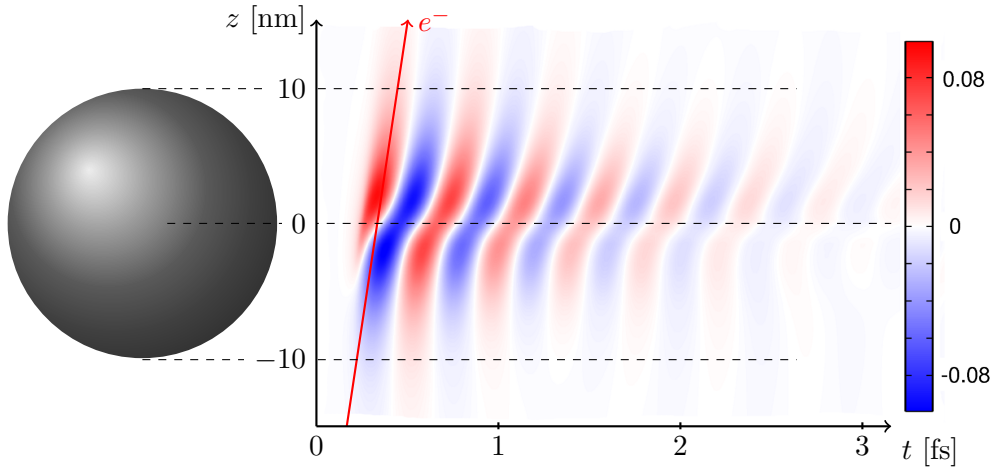


Figure 7.3: Example of induced field. We plot the z -component of the field induced at a 10 nm radius aluminum sphere along the electron trajectory as a function of time. The position of the electron as well as the relation to the sphere is indicated. Due to the high damping in aluminum, the field decays rapidly. We also see that the field is strongly localized at the particle.

Figure 7.3 shows an example of the induced field along the electron trajectory as a function of time. The target particle is a 10 nm sphere with a Drude model for aluminum. We see that the fields are localized at the particle and decay in time. Both characteristics facilitate the simulation of EELS experiments on a finite computational domain in finite simulation time. In the following two sections we will study how these truncations influence the results for the loss probability.

7.2.1 Finite Simulation Time

From the induced field shown in Fig. 7.3 we calculate the Fourier components in order to evaluate the loss probability. We have to run the simulation until the fields have almost vanished to get converged Fourier components. To check the influence of simulation time on the results, Fig. 7.4 shows the loss probability for a gold sphere for different

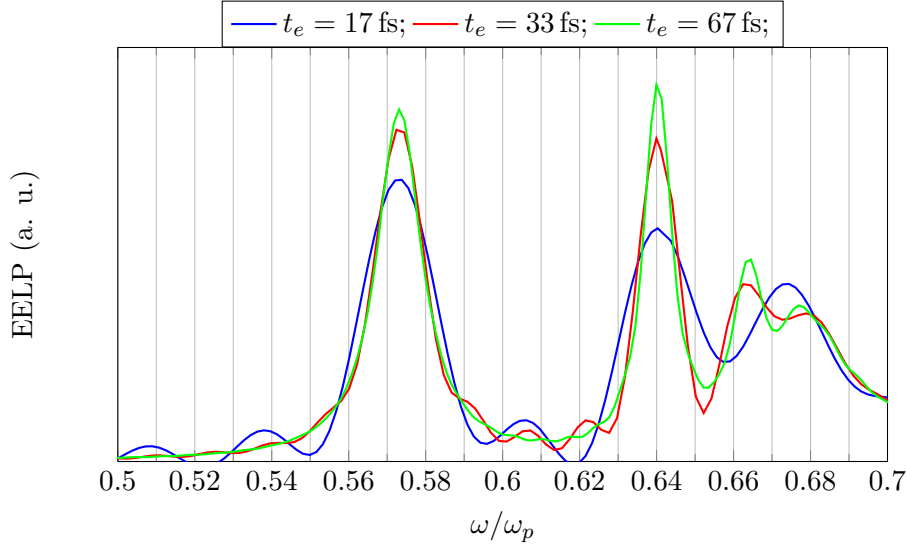


Figure 7.4: Influence of the time probability in the DGTD simulations. If the simulation time is too short, the Fourier components of the induced field have not converged and cause oscillations in the loss probability.

times. For $t_e = 17$ fs there are huge oscillations, the amplitude of which decreases for $t_e = 33$ fs. To get converged results we have to choose $t_e = 67$ fs in this simulation. The time necessary depends, of course, on the particle properties, especially the permittivity. For the aluminum Drude model used to generate Fig. 7.3 the damping is much higher as compared to the gold Drude model used for the tests above. For dimers, we will have to use simulation times of up to 230 fs to get converged results.

In summary, choosing the simulation time too short will result in an oscillatory behaviour of the loss probability and can always be compensated for by increasing the simulation time. Therefore, we can easily rule out any artefacts resulting from the finite time.

7.2.2 Finite Computational Domain

We now consider the finite computational domain required by the DGTD method. In principle, the electron trajectory extends to infinity. Again, we benefit from the characteristics of the induced surface plasmons. They are localized at the scatterer surface and decay with increasing distance from the surface. Therefore, we can choose the computational domain sufficiently large, such that the induced field at the boundaries of the computational domain is negligible. Thus, the distance between scatterer and the PML, which we want to call d_{PML} has to be chosen sufficiently large. This is especially important in order to prevent the surface plasmons from leaking into the PML where they would be absorbed which would ultimately lead to an overestimated damping. We note that the initial position of the electron $\mathbf{r}_e(t_0)$ is not necessarily located inside the

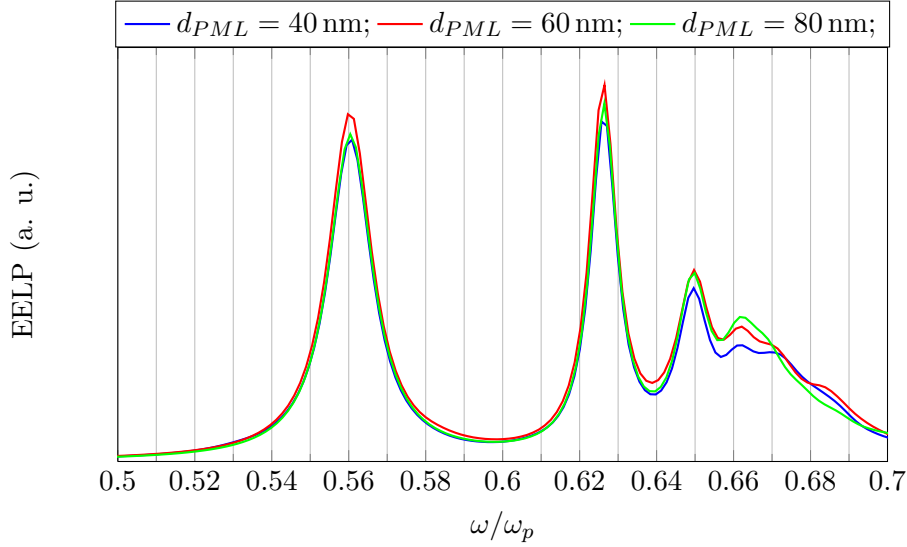


Figure 7.5: Influence of the size of the computational domain on the loss probability in the DGTD simulations.

computational domain. The electron is represented by its electric and magnetic field either on the TFSF boundary, or, if a SF formalism is used, inside the scatterer. These fields may well be calculated if the electron is outside the domain.

The results for different scatterer-to-PML distances d_{PML} are shown in Fig. 7.5. In contrast to the finite computation time results in Fig. 7.4, the results for the different domain sizes do not show a convergent behaviour. We see, however, that the spectral position of the loss peaks does not shift. Furthermore, the differences in the peak amplitude for the different sizes are quite small. The main deviations occur at the high-frequency end of the spectrum. We have already discussed this part of the spectrum when discussing results for the sphere using the T-Matrix method in Sec. 6.3.1. There, we have seen that the broad peak at the end of the spectrum consists of the contributions of a huge number of multipoles. Thus, as far as the applicability of the method to the identification of individual eigenmodes of the particle is concerned, the deviations are acceptable. More importantly, we have a high accuracy concerning the spectral position of the first few eigenmodes and a reasonable accuracy for the amplitude of the loss peaks.

7.2.3 Spatial Resolution

Finally, the tetrahedral mesh determines the accuracy of the results. All geometric properties of the particle must be represented accurately. Also, the mesh must be fine enough to resolve the incident field of the electron. For the particles considered in the following, the latter condition is the stronger one. Therefore, geometric features are well represented. Concerning the incident field, we can use the T-Matrix method to benchmark the DGTD results to see whether we get a good agreement. This is done in

the following section for the spheroid.

7.3 Spheroid — Far-field Patterns and Cathodoluminescence

We have already studied the spheroid in Sec. 6.3.2 using the T-Matrix method. In this section we will compare the T-Matrix results with those obtained by the DGTD, not only for the loss probability but also for the photon emission probability, which can also be obtained using the DGTD.

The parameters are the same as in Sec. 6.3.2 and in addition we choose the distance to the PML to be $d_{PML} = 100$ nm and the maximum element size for the scatterer to be $h_{scat} = 1$ nm. The computation time is $t_e = 133$ fs, which is sufficient for the fields to decay. Before showing the results, we will briefly discuss how the far-field properties can be calculated in the DGTD method.

7.3.1 Cathodoluminescence

The CL probability can be evaluated in the DGTD framework, too. As it is a frequency-domain quantity, we will have to perform a Fourier transform just as in the calculation of the loss probability. We are free to calculate the CL probability on any surface S enclosing the scatterer according to Eq. (5.6). Because $\mathcal{F}(\mathbf{E}) \times \mathcal{F}(\mathbf{H}) \neq \mathcal{F}(\mathbf{E} \times \mathbf{H})$, we have to first perform the Fourier-transform and then evaluate the cross product. This means we have to store the field values for each time-step for every node of the surface S , which increases the memory demands of the method, however on modern computers these demands can easily be satisfied. Thus, the DGTD method can also be used for the simulation of cathodoluminescence experiments. Figure 7.6 shows the EELS and CL probability of the prolate spheroid introduced in Sec. 6.3.2 calculated with the DGTD and the T-Matrix method for comparison.

The agreement for the EELP for the lowest order modes is excellent. Some minor deviations occur for the higher order modes between $0.65\omega_p$ and $0.7\omega_p$. Nevertheless, the agreement is still good.

For the CLP we also see an excellent agreement between the T-Matrix and the DGTD results. Both, the spectral position as well as the amplitudes of the peaks are accurately reproduced. This proves that the DGTD is well suited not only for the EELP calculation, but also for the calculation of the CLP. In the next section we will show that also the far-field patterns can be calculated accurately.

7.3.2 Far-field Patterns

The far-field patterns of the spheroid have already been discussed using the T-Matrix method in Sec. 6.3.1. We will now show that the patterns can also be calculated in the DGTD framework. Here, we have only a finite-computational domain and in order to reduce the influence of the near-fields, we could increase the size of the computational domain to a certain extend. This, however, will also increase the number of elements

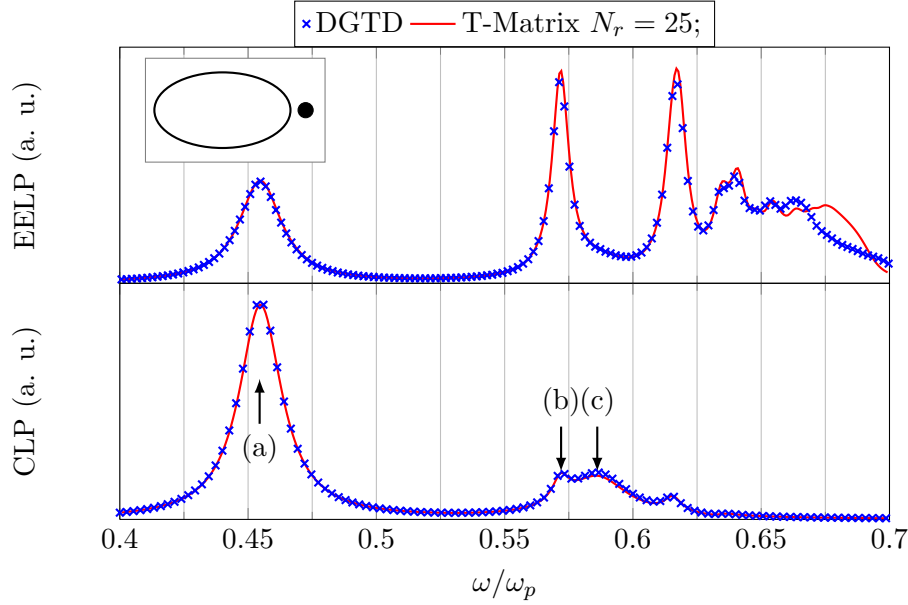


Figure 7.6: Comparison of the EEL and CL probability for the prolate spheroid obtained using the T-Matrix method and the DGTD method. We see a very good agreement between the two methods for both, the spectral position and the amplitude of the peaks in the spectra.

and thus the computational effort. Alternatively, we can employ a near-to-far field transformation.

The basic equation for the far-field calculation is the representation theorem for electromagnetic fields (3.47). It can be used to represent the electric field outside a given volume V as surface integrals over ∂V involving the tangential components of the electric and magnetic field on the surface ∂V as well as the Green function of the Helmholtz equation. The surface ∂V is not restricted to correspond to a physical boundary. We are free to introduce a virtual boundary of spherical shape that completely encloses the scatterer. If we assume the observation point \mathbf{r} , where we want to evaluate the far-field, to be in a huge distance to V we can make use of the *far-field approximation*. The situation is sketched in Fig. 7.7.

We have already discussed that the asymptotic form of the scattered field is a spherical outgoing wave, cf. Eq. (5.7a) on P. 70. Thus we can assume that $\mathbf{k} = k\mathbf{e}_r$. Furthermore, the gradient operator ∇ acting on \mathbf{r} can be replaced by $\nabla \approx -i\mathbf{k}$. Finally, we see that $|\mathbf{r} - \mathbf{r}'| \approx |\mathbf{r}|$. With these assumptions, the Green function of the Helmholtz equation in the far-field approximation reduces to

$$\left. \begin{aligned} \frac{1}{4\pi} \frac{e^{-ik|\mathbf{r}-\mathbf{r}'|}}{|\mathbf{r}-\mathbf{r}'|} &\approx \frac{1}{4\pi} \frac{e^{-ikr}}{r} e^{i\mathbf{k}\cdot\mathbf{r}'} \\ \nabla &\approx -i\mathbf{k} \end{aligned} \right\} \text{for } \mathbf{r}' \in \partial V \text{ and } |\mathbf{r}| \gg |\mathbf{r}'| \quad (7.14)$$

with $\mathbf{k} = k\mathbf{e}_r$. By plugging in these expressions in the representation theorem (3.47), we obtain the so-called near-to-far-field transform. It rules out all near-field contributions

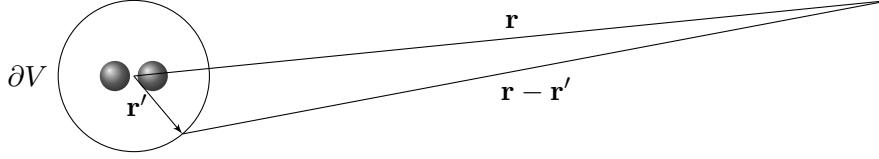


Figure 7.7: **Sketch of the far-field approximation.** The observation point \mathbf{r} is far away from the point \mathbf{r}' . The latter one is assumed to be on a spherical surface ∂V which encloses the scatterer. Under these assumptions the Green function of the Helmholtz equation can be simplified as explained in the text.

and allows for an accurate calculation of the far-field amplitude that is proportional to the angle-resolved photon emission probability as shown in Sec. 5.4. With this, we can evaluate the far-field patterns and compare them to the results of the T-Matrix method. A comparison is shown in Fig. 7.8. We see an excellent agreement between the results verifying the applicability of the DGTD method to angle-resolved CL calculations.

7.4 Sphere Dimer - Dark Mode Excitation

While the single particle properties can be nicely obtained using EELS, also the coupling between plasmonic particles can be studied. In contrast to optical spectroscopy, the unique characteristics of EELS allow for a more detailed analysis of particle systems. In the following we will demonstrate this on a simple test system - a dimer of nominally identical spheres.

We already discussed the sphere dimer using the T-Matrix method in Sec. 6.3.3, however there, the electron trajectory had to be located outside the smallest sphere circumscribing the scatterer (also, cf. Sec. 3.2.3). In the DGTD method, there is no such restriction and we can investigate the plasmonic properties of such a dimer in more detail. Also, because the DGTD works in time-domain, it is possible to study the time-evolution of the induced field.

7.4.1 Time-Evolution of the Excited Fields

Being a time-domain method, it is straight-forward to study the time evolution of the excited fields using the DGTD. Figure 7.9 shows a dimer of 10 nm spheres with a Drude model to approximate the permittivity of aluminum (cf. Tab. 2.1). We plot the z component of the electric field (causing the losses according to Eq. (5.3)) in the plane containing the centers of the spheres and the electron trajectory. We are using a TFSS formalism here, and the electron is contained in the small SF channel indicated by two lines between the spheres. The left column of Fig. 7.9 from top to bottom shows the excitation. At $t = 0.18$ fs the electron, indicated as a black circle, approaches the dimer. A detailed

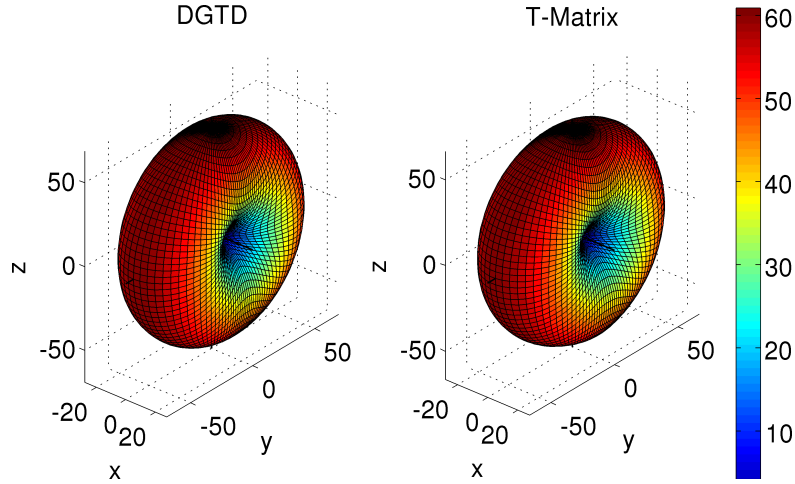


Figure 7.8: Far-field patterns for the lowest order mode of the prolate spheroid obtained with the DGTD and T-Matrix method. Both, the overall shape as well as the amplitude are in agreement. This also holds for the higher order mode patterns (not shown here).

look at the SF channel shows how the incident field is only propagated outside the channel. In the lower left image at $t = 0.38$ fs, one can already see that the electron induced an electric field at the particles that is sustained by the dimer. This induced field is also propagated *inside* the SF channel. The induced fields are oscillating and propagate along the particle surface at which they are localized. Skipping forward in time to $t = 0.82$ fs, we see that the fields are still sustained by the dimer. The three-image sequence on the right give an impression of the propagation of the fields. Starting from almost the center of the dimer, the field minimum, depicted in blue and indicated by a white arrow, propagates in positive z direction and finally splits up into two parts that are localized to the respective sphere. The field amplitude in the dimer gap is large due to the coupling whereas the amplitude decreases as the surface plasmons propagate to the far sides of the spheres. Due to the intrinsic damping of the dimer material, these oscillating fields decay and finally vanish at later times.

7.4.2 Dark and Bright Mode Excitation

In this section, we will use the same geometry as in the preceding section, however we now use a Drude model for gold instead of aluminum (cf. Tab. 2.1). The lower damping for gold leads to narrower peaks in the spectra and the lower order modes are well separated.

The coupling between the modes of the spheres can also be discussed within a hybridization model [93]. Inspired by molecular physics the modes are categorized as bonding and anti-bonding modes. If we approximate the spheres as dipoles, this translates to modes where dipole moment of the spheres is parallel (bonding) or anti-parallel (anti-

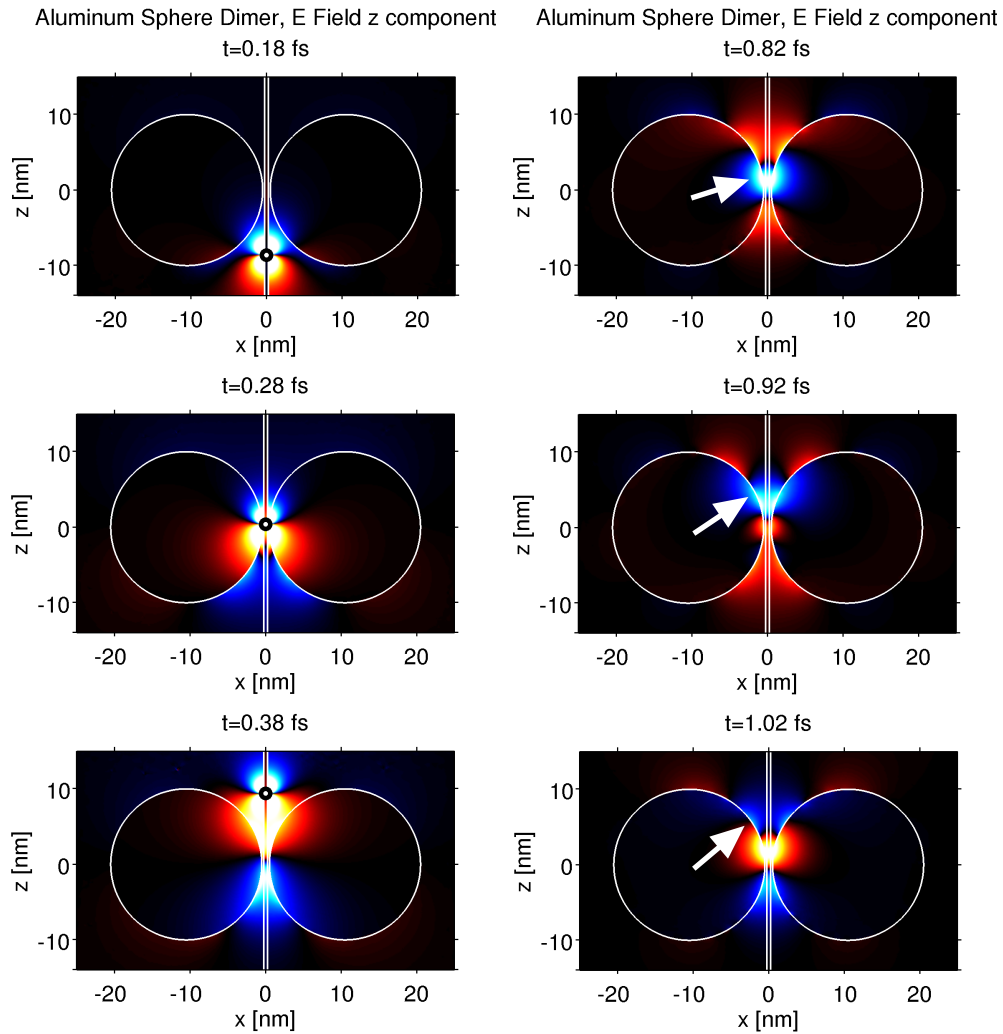


Figure 7.9: Time evolution of the z component of the electric field for an aluminum sphere dimer. The excitation is shown in the left-hand side images, where the electron moves in positive z direction and is marked with a black circle. The right-hand side images show the field at later instances. The white arrow indicates the propagation of the excited surface plasmons. For details see the text. Adapted from [M4].

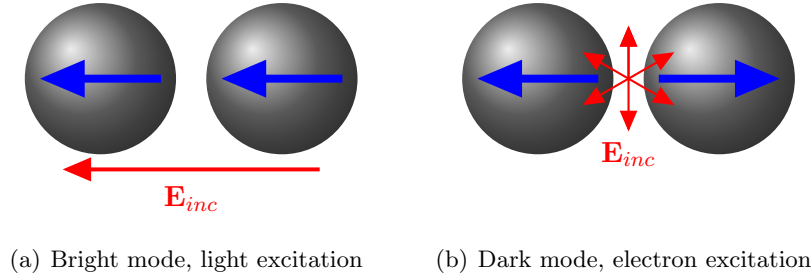


Figure 7.10: **Mode hybridization in dimers.** (a) When excited optically, e.g. with a laser beam, the dipole moments of the two spheres will be aligned parallel to the incident light polarization. (b) Modes where the dipole moments are anti-parallel cannot be excited optically but require a source localized between the sphere, such as the electron excitation in EELS.

bonding). Figure 7.10 gives a schematic representation of these modes.

For an eigenmode to be excited, not only the frequency of the excitation has to match the frequency of the eigenmode, but also the symmetry of the eigenmode must be compatible with that of the excitation. As apparent from Fig. 7.10(a), the modes with parallel dipole moments can be excited with light, e.g. with a plane wave as indicated in the figure. Due to symmetry reasons, the modes with anti-parallel dipole moments cannot be excited this way. Accordingly, these modes are also called *bright modes* and *dark modes*, respectively. The dark modes can be excited, however, by a localized source between the spheres. This can be, e.g. the spontaneous emission by a molecule in the gap or the electron in EELS experiments, if the electron trajectory passes the sphere gap as indicated in Fig. 7.10(b). We study the EEL spectra for the gold sphere dimer for different excitation trajectories in Fig. 7.11. We note that for the central excitation at position 1 indicated in the figure, the bright modes are even symmetry forbidden. Hence, the *optically bright modes* are the dark modes of EELS. For the excitation at positions 2 and 3, we expect that these optically bright modes are excited as well. We see that for position 2 and 3 (blue and red curve) there are two modes between at $0.43\omega_p$ and $0.5\omega_p$ that are excited, that do not appear in the central excitation (green curve). Hence, these modes are optically bright modes. On the high frequency end of the spectrum, i.e. $> 0.7\omega_p$ we see several modes that are only excited in the central excitation. Thus, they can assumed to be optically dark modes.

7.5 Sphere Dimer as a Nano-Antenna

Antennas are well known in every-day life and much of our modern communication relies on them, be it mobile phones, radio or television broadcasting. Basically, antennas are devices that turn localized currents into propagating electromagnetic radiation and vice-

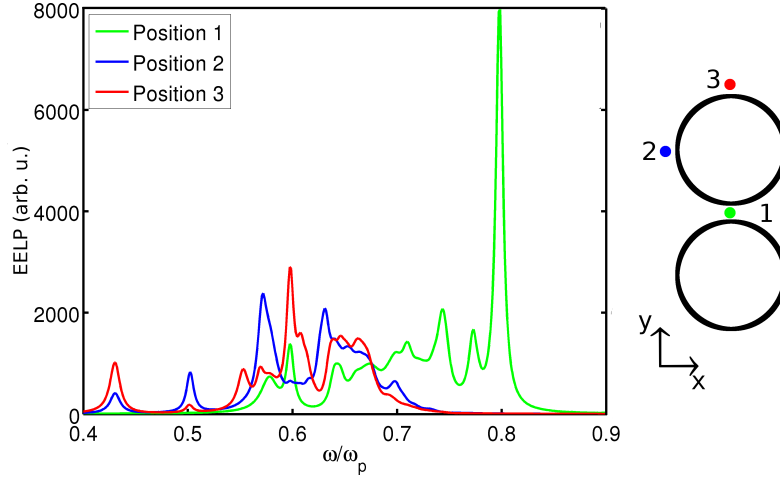


Figure 7.11: EELP of a gold dimer of 10 nm sphere excited at different positions to selectively excite dark modes. For details see the text.

versa. Radio frequency antennas are macroscopic objects. For example, a simple dipole antenna for terrestrial video broadcasting (DVB-T) has the size of some 20 cm and the wavelength of the used frequency bands (VHF III, UHF IV, V) is between 60 cm and 160 cm. The scale invariance of Maxwell's equations (cf. Sec. 2.1.6) suggests that an *antenna for light* should have dimensions of some 100 nm. Indeed, the notion *Nano-Antenna* is already well established in the literature [105] and analogs of radio frequency antenna techniques can also be applied to nano-antennas. One example of which is the combination of several components to increase the directivity of such antennas, which are then termed Yagi-Uda antennas. In Sec. 6.3.3 we have studied the far-field patterns of the sphere dimer and have observed one mode with a high directivity around $\omega = 0.6\omega_p$, plotted in Fig. 6.12(d). We now exploit this characteristic to construct a nano-transmission line. Our transmitter will be a sphere dimer, which is excited by an electron. In the high transmission direction, that we estimate from the far-field pattern, we place a second dimer that will act as receiver. The distance between the dimers is chosen sufficiently large to suppress a direct coupling due to the evanescent near-fields. The basic setup is shown on the left-hand side of Fig. 7.12. The lateral distance is $d_x = 420$ nm and the vertical distance is $d_z = 130$ nm (not to scale in the figure). In the right-hand side of Fig. 7.12 we plot the z -component of the field that is received along the blue line as a function of time. We see oscillations of the field after a short time. This radiation originates from the excited transmitter dimer. We observe huge field amplitude near the receiver dimer at $z = +65$ nm, which indicates that the radiation from the transmitter indeed excites the receiver. These localized excited fields are sustained even after the radiation from the transmitter dimer has vanished. To further investigate the transmission, we perform a Fourier transform of the received field and plot the power spectrum of the E_z component as a function of the z -coordinate in Fig. 7.13. We clearly see a peak near the location of the receiver dimer at +65 nm

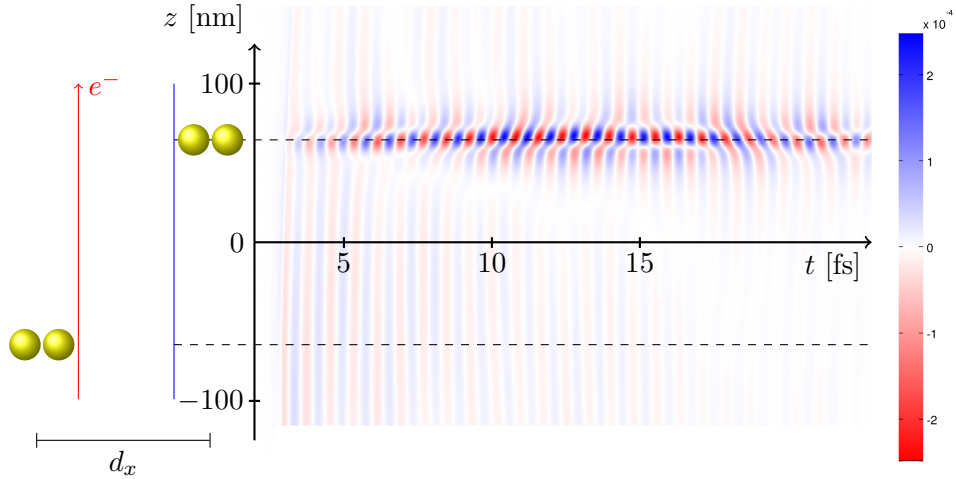


Figure 7.12: A nano-transmission-line. The left-hand dimer is excited by an electron and acts as a transmitter. The right-hand side dimer is not excited and acts as a receiver. The lateral distance is $d_x = 420$ nm to prevent a coupling of the two dimers by the near-fields. The field along the dashed vertical line near the receiver dimer is shown on the right-hand side of the figure.

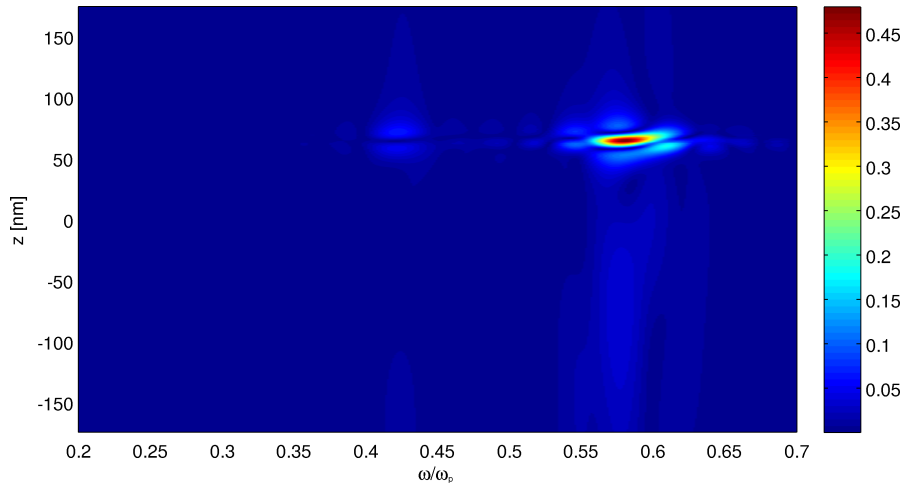


Figure 7.13: Absolute value of the Fourier component of \mathbf{E}_z as a function of frequency along the electron trajectory.

for a frequency around $0.6\omega_p$. As this is exactly the frequency of the high directivity mode, we conclude that we have indeed used the two dimers as a nano-transmission line facilitating "wireless communication in the nano-world".

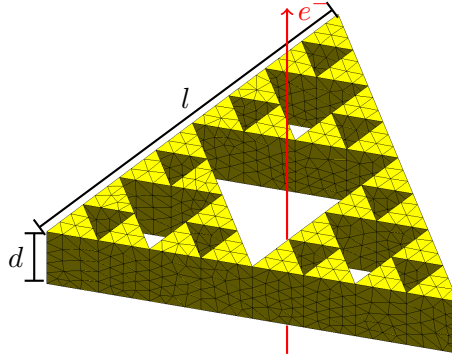


Figure 7.14: Sierpinski triangle in 3rd iteration represented by a tetrahedral mesh. The electron trajectory passes the geometric center of the triangle as indicated.

7.6 Sierpinski Triangle

So far, we have only considered particles of simple shape that could also be treated using the T-Matrix method. One of the valuable advantages of the DGTD method is the tetrahedral mesh, which allows for an accurate representation of complicated geometries. To demonstrate the capabilities of the method, we choose the target particle to be the self-similar Sierpinski triangle. It can be constructed by starting with a solid triangle, dividing it into four triangles and removing the middle one. Iterating this process another two times for all resulting triangles leads to the structure shown in Fig. 7.14. Fractal antennas are a well known approach in radio-frequency applications and recently also the nano-meter equivalent was investigated numerically simulating optical spectroscopy [106]. Due to the flexible tetrahedral mesh of the DGTD, we are able to simulate EELS and CLS experiments for such complicated structures, too. Figure 7.15 shows the EEL and CL probability for the structure and excitation shown in Fig. 7.14 for different side-lengths l . The EELP shows three distinct peaks at the low-frequency end of the spectrum that shift according to the side-length. Thus, they could correspond to the fundamental modes of the faces of the triangle. These modes, however, do not significantly contribute to the CLP. In the mid- and high-frequency region, we see a huge number of modes that form a broad band response of the structure that contributes to both, the EELP and the CLP. We study the influence of the iteration on the loss probability in Fig. 7.16. The parameters are the same as above, but now we also consider the second iteration of the triangle. At the low-frequency end of the spectrum we see two peaks for the second as compared to three peaks for the third iteration. This suggests that these peaks indeed are associated with the fundamental modes of the faces of the triangle faces. After the common spectral gap, we see that for higher frequencies, there are fewer modes that contribute to the losses for the triangle in second iteration. We see that the DGTD opens the way towards the analysis of complicated geometries.

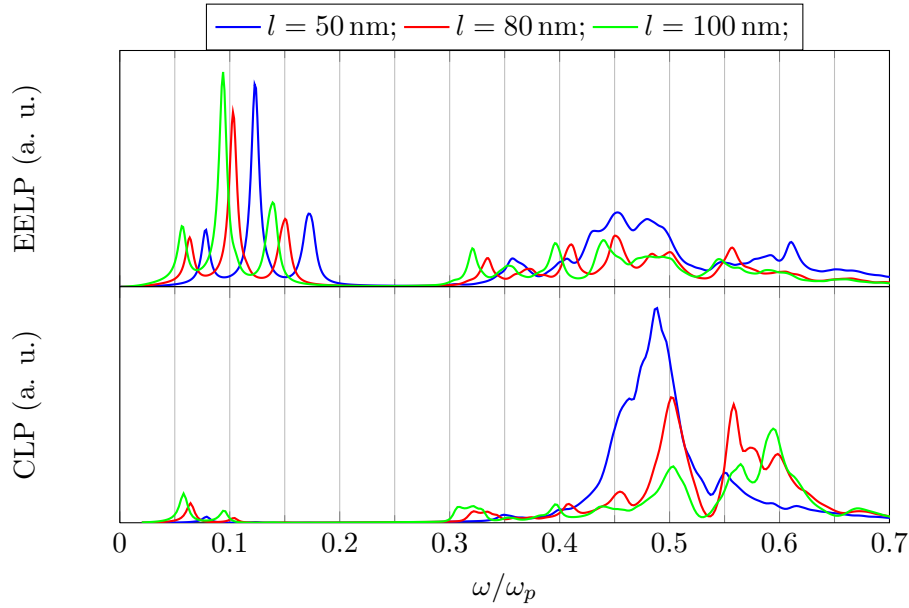


Figure 7.15: EEL and CL probability for the Sierpinski triangle in 3rd iteration for different side lengths. The EELP shows three distinct peaks at the low-frequency end of the spectrum that shift according to the sidelength. For higher frequencies, a number of peaks contribute and form a broad band of non-vanishing loss-probability. This broad band also dominates the CLP.

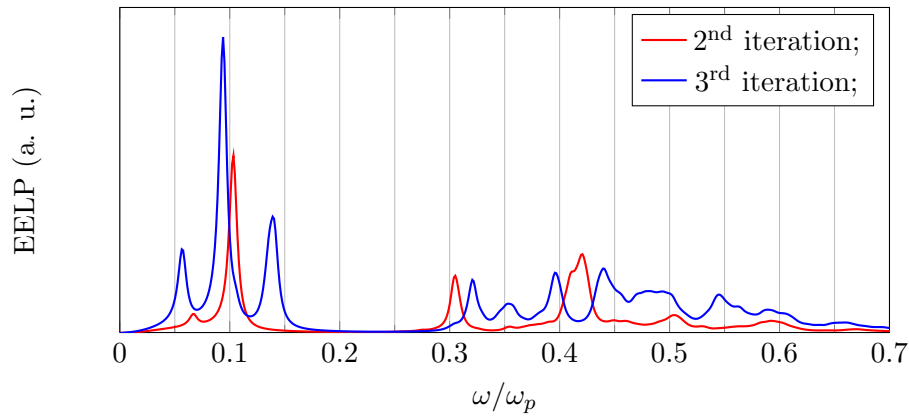


Figure 7.16: EEL spectra for the Sierpinski triangle with $l = 100$ nm in second and third iteration. On the low-frequency end of the spectrum the third iteration leads to a new peak.

7.7 Split Ring Resonator - Babinet's Principle

Split Ring Resonators (SRR) are the paradigm meta-atom for building metamaterials. Intuitively, a SRR acts as a LC-circuit. A closed ring would sustain a ring current possessing a considerable magnetic moment. If the ring is broken by a slit, this slit will act like a capacitor and the split ring will basically act like an inductance. In contrast to natural materials, a metamaterial consisting of SRRs will show a considerable magnetic response in the visible part of the electromagnetic spectrum, given the parameters of the SRR as size, gap and material are carefully chosen. For such materials the permeability μ could even be negative. Together with the metallic properties of the SRR, i.e. $\varepsilon < 0$, one could construct materials with a $\varepsilon < 0$ and $\mu < 0$ at the same frequency. As pointed out by Veselago [18], in this case, the basic equations governing electrodynamics would remain unchanged, e.g. the refractive index $n = \sqrt{\varepsilon\mu}$, however for a plane wave, \mathbf{E} , \mathbf{B} and \mathbf{k} would merely form a left-handed set of vectors instead of a right-handed one if we had $\varepsilon > 0, \mu > 0$. Constructing such a material, however, would require to exactly match the resonance frequencies of ε and μ , which is far from being feasible even with today's fabrication technologies. Nevertheless, potential applications, such as optical cloaking [107] are already being discussed. Reaching for improved metamaterials requires the exact characterization of the meta-atom, e.g. the SRR. Here, EELS offers an excellent tool to study the plasmonic properties of SRRs as demonstrated recently [M3, 108]. Also, the experiments performed in [M3] were simulated using the DGTD and the results compared to the measured spectra. To that end, we represent the SRR with a tetrahedral mesh. The lateral dimensions of the SRR are approx. 200 nm, the thickness is assumed to be 35 nm. The SRR is suspended on a 30 nm thick silicon nitride substrate. Further details on the fabrication process can be found in [M3].

Figure 7.17, that we have already encountered in Chap. 5, shows simulated and measured spectra of a single gold SRR obtained at three different spots. We see a very good agreement between simulation and experiment. The major deviations concern the relative amplitudes of the loss peaks and the fine structure of the peaks above 2.0 eV. The latter one can be explained by the energy resolution of the measurements, which is deduced from the width of the ZLP and evaluates to 0.18 eV. Therefore, fine features are likely to be smeared out in the measurement while they are present in the simulation. This also reduces the amplitudes of the peaks which explains that the peaks in the red and green curve at 0.7 eV and the one in the blue curve at 2.0 eV are more pronounced in the simulation.

A special mode of operation in EELS experiments is the so-called energy-filtered EELS. Here, the electron beam is scanned across the structure and the number of electrons within a narrow energy window is measured. Such measurements result in so-called EELS maps. We show the maps at different energies obtained experimentally and numerically for the SRR in Fig. 7.18 and its complementary structure (an aperture in a gold film) in Fig. 7.19. Dark blue colors correspond to a low loss probability, bright yellow colors to a high one. Again, we see a very good agreement between the experiment and the simulation. We have already discussed that the loss probability is determined by the E_z component of the excited eigenmodes. In the case of well separated modes,

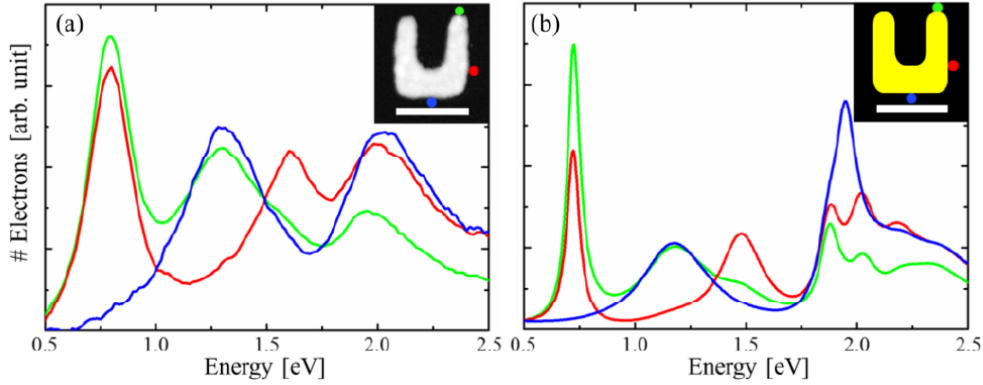


Figure 7.17: EEL spectra of a single gold SRR, measured (left-hand side) and simulated using the DGTD (right-hand side). The scale bars are 200 nm. For details see the text.

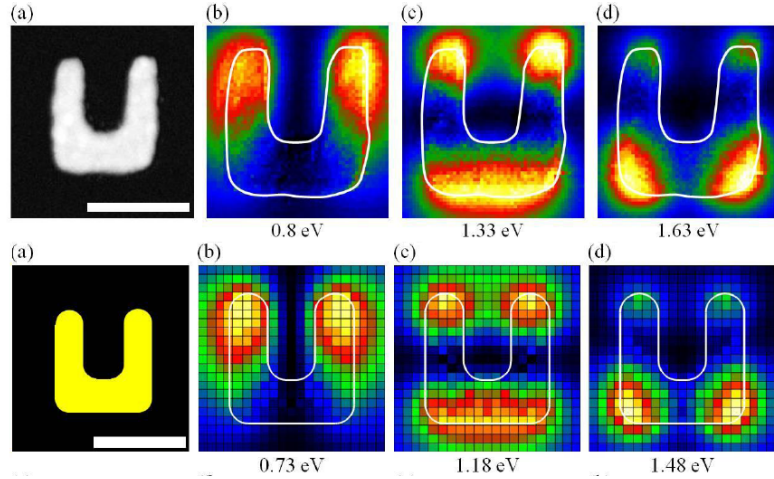


Figure 7.18: Experimental (top) and numerical (bottom) EELS maps of a SRR for different loss energies. Blue colors correspond to low, yellow colors to high amplitudes. Scale bars are 200 nm. We see a very good agreement between theory and experiment. Adapted from [M3].

energy-filtered EELS thus maps the E_z component of a single eigenmode. For planar metallic structures like the SRR, the electric field component can be assumed to be proportional to the current density. Accordingly, low loss probabilities correspond to nodes in the current density. With this we see that the current density has one node for the lowest mode (b) in Fig. 7.18. For mode (c), we observe two nodes located at the arms of the SRR and three nodes for mode (d). The discussion for the complementary structure is not that straight-forward. However, we can make use of the generalized Babinet prin-

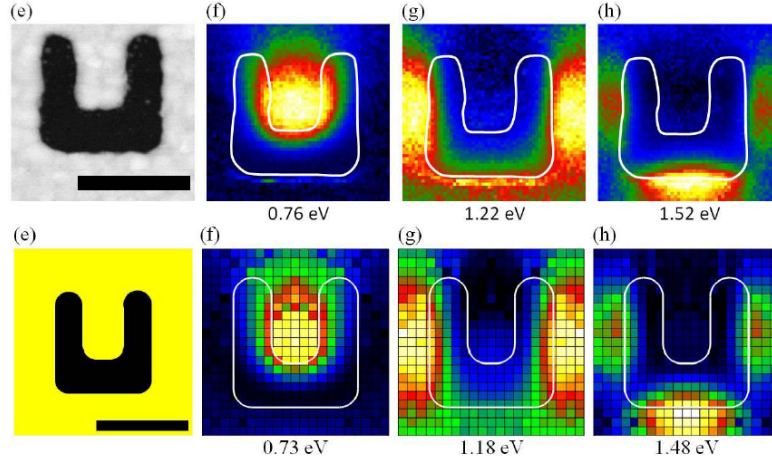


Figure 7.19: Experimental (top) and numerical (bottom) EELS maps of the complementary SRR structure for different loss energies. Scale bars are 200 nm. Again, we see a very good agreement between theory and experiment. Adapted from [M3].

ciple [109]. Originating from scalar diffraction theory for screens with apertures and the complementary screen, it has also been applied to vector diffraction theory. It states that the electric field of the direct structure and the magnetic field of the complementary one are proportional and vice-versa. Figure 7.20 shows the z component of the electric and magnetic field for the SRR and its complementary structure. The fields are recorded in a plane 20 nm above the structure. The structures are excited by a plane with polarization indicated by the white arrows. We see indeed, that the electric and magnetic field of the direct structure are proportional to the magnetic and electric field of the complementary one, respectively as predicted by the generalized Babinet principle. We also see that indeed the E_z component of the direct structure corresponds to the EELS maps for the direct structure in Fig. 7.18. Finally, we see that the EELS maps of the complementary structure correspond to the magnetic field of the direct structure.

7.8 Conclusion

In this chapter, we have extended the DGTD method to the simulation of EELS and CLS experiments, which required to calculate the electromagnetic field caused by a moving electron. This makes the advantages of the DGTD method, which are the flexible spatial discretization, high order accuracy and the possibility to include non-linearities, available for electron microscopy simulations. To the best of the author's knowledge it is the first report on a time-domain approach to EELS simulations and the first one of CLS experiments that does not use an approximation of the incident field. We have discussed the influence of the finite computational domain and finite simulation time, and we have seen that we get accurate results with reasonable computational resources.

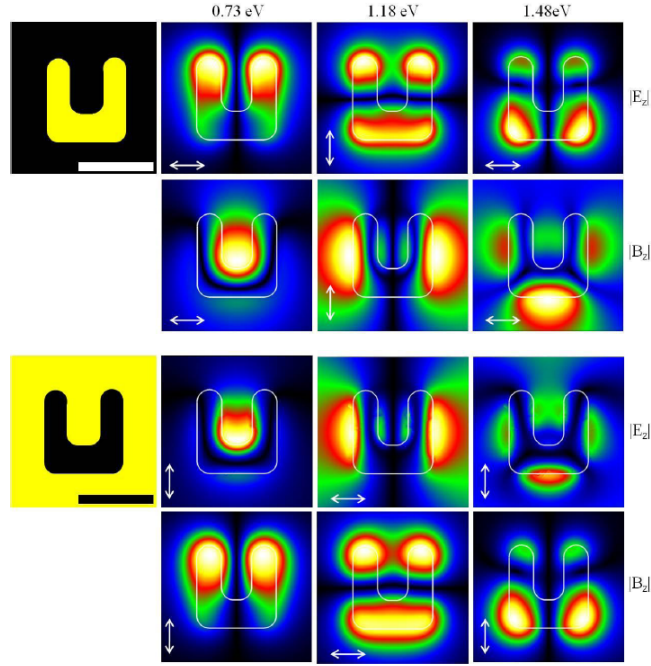


Figure 7.20: Demonstration of the generalized Babinet Principle. Absolute value of the z component of the electric and magnetic field for the SRR (top) and its complementary structure (bottom), excited by a plane wave with the respective photon energy and polarization as indicated by the arrows. We see that for the direct structure the E_z component is proportional to the B_z component of the complementary one and vice-versa. Taken from [M3].

We have benchmarked results for a spheroidal particle for both, EEL and CL probability plus far-field amplitude against results obtained with the T-Matrix method. We have seen an excellent agreement, which was not necessarily expected when comparing results of a time-domain and a frequency-domain method. The advantages of the flexible spatial discretization have been demonstrated by simulating EELS and CLS on a fractal structure as the Sierpinski triangle. The advantage of the time-domain approach was demonstrated on a nano-transmission line consisting of two sphere dimers, where one was excited with an electron acting as a transmitter and the other, far from the excited one, acted as a receiver. Finally, the method has proven to yield results that are in very good agreement with measurements performed on a Split Ring Resonator and its inverse structure.

In summary, the Discontinuous Galerkin Time-Domain method can be considered as a reliable tool for electron microscopy simulations. The flexibility regarding the spatial discretization comes at the price of higher computational cost as compared to the T-Matrix method. However, a time-domain method that may be extended to include non-linear material properties might be useful in the future simulations.

8 Conclusion and Outlook

In this thesis we have presented simulations of experiments involving metallic nanoparticles. We have applied available methods to the problem of light-scattering from spheroidal silver nano-particles in Chap. 4. We have compared the results of several numerical methods for the near-field at the particles and also the scattering efficiency. All methods have shown good results, however, the Discrete Dipole Approximation requires massive computational resources to yield good accuracy as compared to the other methods.

Having tested the numerical methods, we were able to undertake the simulation of experiments where spherical silver nano-particles can be transformed to spheroidal shape using laser irradiation. The transformation process is believed to crucially depend on the electric near-field enhancement inherent to resonantly excited metallic nano-particles. The simulation results were shown to be in good agreement with the possible explanation of the process, giving evidence that the near-field plays indeed a crucial role.

Beyond the application of numerical methods, we have also extended two available methods for light scattering, the T-Matrix Method and the Discontinuous Galerkin Time Domain method (DGTD), to be applicable for Electron Energy Loss (EELS) and Cathodoluminescence Spectroscopy (CLS) experiments. The necessary extensions have been presented and were the spherical vector wave function expansion coefficients of the field caused by a moving electron for the T-Matrix method and the field as a function of time and space for the DGTD Method.

The T-Matrix method is very efficient due to the semi-analytical approach and can be applied to particle shapes usually encountered in EELS experiments, like spheres, sphere dimers and nano-rods. We have shown results for these particles for both, EELS and CLS experiments. Furthermore we were able to study the far-field pattern emitted by the excited nano-particles. Overall, the T-Matrix approach to EELS and CLS is very promising and the efficiency of the method could open up the way for the optimization of metallic nano-structures for a given purpose. To improve the applicability of the method to the interpretation of experiments, there are some desirable extensions. In the scope of this thesis, unfortunately, it was not possible to cover them all. The most important aspect would be the inclusion of a substrate to support the particle under examination. This is no principle hurdle for the method, however, if the electron trajectory is supposed to intersect the substrate, the derivation of the expansion coefficients must be adapted. The same holds true for electron trajectories penetrating the particle itself. In that case, the longitudinal modes must be taken into account in the internal field.

The Discontinuous Galerkin Time-Domain (DGTD) method was shown to be well-suited for electron microscopy simulations as well. It has the advantage of being very flexible regarding the particle shapes, however this comes at the price of higher compu-

8 Conclusion and Outlook

tational demands as compared to the T-Matrix method. Nevertheless, computations can easily be done on a modern desktop computer. Here, improvements of the numerics, especially the use of general purpose graphics processing units, might yield a dramatic increase in efficiency. Another advantage of the DGTD method is the computation in time-domain. Comparing results with T-Matrix results has shown an excellent agreement, therefore the time-domain approach can be considered validated. It allowed to study the time evolution of the electromagnetic fields and we have exploited this ability to study the fields induced at a sphere dimer as well as to illustrate a nano-transmission line consisting of two sphere dimers. Most importantly, we had the opportunity to compare numerical and experimental results for a split-ring resonator and have seen a very good agreement. Further development for the DGTD surely should exploit the time-domain approach to include more sophisticated, non-linear material models, like e.g. the hydrodynamic model. Recent experiments suggest that the classical Drude and Lorentz model are valid down to the nano-meter regime ¹, however, more sophisticated models could yield better agreement on even smaller scales. Here, the DGTD could be used in conjunction with Electron Microscopy experiments to find out, for what dimensions classical electrodynamics is still valid and what new effects are yet to be found.

¹arXiv:1112.5008v1

Bibliography

- [1] J. C. Maxwell. *A Treatise on Electricity and Magnetism*. Oxford, 1873.
- [2] G. Mie. “Beiträge zur Optik trüber Medien, speziell kolloidaler Metallösungen”. In: *Annalen der Physik* 330 (1908), pp. 377–445.
- [3] R. Zia et al. “Plasmonics: the next chip-scale technology”. In: *Materials Today* 9 (2006), pp. 20–27. DOI: 10.1016/S1369-7021(06)71572-3.
- [4] M. E. Stewart et al. “Nanostructured Plasmonic Sensors”. In: *Chemical Reviews* 108 (2008), pp. 494–521. DOI: 10.1021/cr068126n.
- [5] H. A. Atwater and A. Polman. “Plasmonics for improved photovoltaic devices”. In: *Nat Mater* 9 (2010), pp. 205–213. DOI: 10.1038/nmat2629.
- [6] J. Nelayah et al. “Mapping surface plasmons on a single metallic nanoparticle”. In: *Nat Phys* 3 (2007), pp. 348–353. DOI: 10.1038/nphys575.
- [7] T. Coenen et al. “Directional Emission from Plasmonic Yagi-Uda Antennas Probed by Angle-Resolved Cathodoluminescence Spectroscopy”. In: *Nano Letters* 11 (2011), pp. 3779–3784. DOI: 10.1021/nl201839g.
- [8] J. D. Jackson. *Classical Electrodynamics*. 3rd ed. John Wiley & Sons, 1998.
- [9] S. A. Maier. *Plasmonics - Fundamentals and Application*. Springer Verlag, 2007.
- [10] J. C. Maxwell. “A dynamical Theory of the Electromagnetic Field”. In: *Phil. Trans. R. Soc. Lond.* 155 (1865), pp. 459–512.
- [11] N. Engheta and R. W. Ziolkowski, eds. *Metamaterials - Physics and Engineering Explorations*. IEEE Press, 2006.
- [12] S. S. Jha. “Theory of Optical Harmonic Generation at a Metal Surface”. In: *Phys. Rev.* 140 (1965), A2020–A2030. DOI: 10.1103/PhysRev.140.A2020.
- [13] J. Polo and A. Lakhtakia. “Surface electromagnetic waves: A review”. In: *Laser & Photonics Reviews* 5 (2011), pp. 234–246. DOI: 10.1002/lpor.200900050.
- [14] J. D. Jackson. “Examples of the zeroth theorem of the history of science”. In: *American Journal of Physics* 76 (2008), pp. 704–719. DOI: 10.1119/1.2904468.
- [15] R. D. L. KRONIG. “ON THE THEORY OF DISPERSION OF X-RAYS”. In: *J. Opt. Soc. Am.* 12 (1926), pp. 547–556. DOI: 10.1364/JOSA.12.000547.
- [16] J. D. Joannopoulos et al. *Photonic Crystals: Molding the flow of Light*. 2nd ed. Princeton University Press, 2008.
- [17] R. B. Wehrspohn, H.-S. Kitzerow, and K. Busch, eds. *Nanophotonic Materials*. 1st ed. Wiley VCH, 2008.

Bibliography

- [18] V. G. Veselago. “The Electrodynamics of Substances with simultaneous negative values of ϵ and μ ”. In: *Soviet Physics Uspekhi* 10 (1968), p. 509. DOI: 10.1070/PU1968v010n04ABEH003699.
- [19] E. Rutherford. “LXXIX. The scattering of alpha and beta particles by matter and the structure of the atom”. In: *Philosophical Magazine Series 6* 21 (1911), pp. 669–688. DOI: 10.1080/14786440508637080.
- [20] M. Husnik et al. “Absolute extinction cross-section of individual magnetic splitting resonators”. In: *Nat Photon* 2 (2008), pp. 614–617. DOI: 10.1038/nphoton.2008.181.
- [21] N. W. Ashcroft and N. D. Mermin. *Festkörperphysik*. 2nd ed. Oldenbourg, 2005.
- [22] P. B. Johnson and R. W. Christy. “Optical Constants of the Noble Metals”. In: *Phys. Rev. B* 6 (1972), pp. 4370–4379. DOI: 10.1103/PhysRevB.6.4370.
- [23] E. D. Palik. “Handbook of Optical Constants of Solids”. In: Elsevier, 1998. Chap. Lynch and Hunter.
- [24] N. D. Mermin. “Lindhard Dielectric Function in the Relaxation-Time Approximation”. In: *Phys. Rev. B* 1 (1970), pp. 2362–2363. DOI: 10.1103/PhysRevB.1.2362.
- [25] F. J. García de Abajo. “Nonlocal Effects in the Plasmons of Strongly Interacting Nanoparticles, Dimers, and Waveguides”. In: *The Journal of Physical Chemistry C* 112 (2008), pp. 17983–17987. DOI: 10.1021/jp807345h.
- [26] C. Prohm. “Modellierung der linearen und nichtlinearen optischen Eigenschaften metallischer Nanostrukturen mithilfe unetstetiger Galerkin Verfahren”. MA thesis. Karlsruhe Institute of Technology, 2010.
- [27] G. Toscano et al. “Modified field enhancement and extinction by plasmonic nanowire dimers due to nonlocal response”. In: *Opt. Express* 20 (2012), pp. 4176–4188. DOI: 10.1364/OE.20.004176.
- [28] G. Veronis and S. Fan. “Bends and splitters in metal-dielectric-metal subwavelength plasmonic waveguides”. In: *Applied Physics Letters* 87, 131102 (2005), p. 131102. DOI: 10.1063/1.2056594.
- [29] E. Ozbay. “Plasmonics: Merging Photonics and Electronics at Nanoscale Dimensions”. In: *Science* 311 (2006), pp. 189–193. DOI: 10.1126/science.1114849.
- [30] J. Homola, S. S. Yee, and G. Gauglitz. “Surface plasmon resonance sensors: review”. In: *Sensors and Actuators B: Chemical* 54 (1999), pp. 3–15. DOI: DOI:10.1016/S0925-4005(98)00321-9.
- [31] A. A. Yanik et al. “An Optofluidic Nanoplasmonic Biosensor for Direct Detection of Live Viruses from Biological Media”. In: *Nano Letters* 10 (2010), pp. 4962–4969. DOI: 10.1021/nl103025u.
- [32] P. Genevet et al. “Large Enhancement of Nonlinear Optical Phenomena by Plasmonic Nanocavity Gratings”. In: *Nano Letters* 10 (2010), pp. 4880–4883. DOI: 10.1021/nl102747v.

Bibliography

- [33] E. Verhagen, L. Kuipers, and A. Polman. “Enhanced Nonlinear Optical Effects with a Tapered Plasmonic Waveguide”. In: *Nano Letters* 7 (2007), pp. 334–337. DOI: 10.1021/nl1062440f.
- [34] W. L. Barnes. “Comparing experiment and theory in plasmonics”. In: *Journal of Optics A: Pure and Applied Optics* 11 (2009), 114002 (9pp). DOI: 10.1088/1464-4258/11/11/114002.
- [35] C. F. Bohren and D. R. Huffman. *Absorption and Scattering of Light by Small Particles*. Wiley VCH, 2004.
- [36] J. A. Stratton. *Electromagnetic Theory*. McGraw-Hill, Inc., 1941.
- [37] A. Doicu, T. Wriedt, and Y. E. Eremin. *Light Scattering by Systems of Particles*. Springer, 2006.
- [38] W. J. Wiscombe. “Improved Mie scattering algorithms”. In: *Appl. Opt.* 19 (1980), pp. 1505–1509. DOI: 10.1364/AO.19.001505.
- [39] W. Neutsch. *Koordinaten*. Spektrum Verlag.
- [40] C. Flammer. *Spheroidal Wave Functions*. Stanford University Press, 1957.
- [41] M. J. Mendes et al. “Near-field scattering by dielectric spheroidal particles with sizes on the order of the illuminating wavelength”. In: *J. Opt. Soc. Am. B* 27 (2010), pp. 1221–1231. DOI: 10.1364/JOSAB.27.001221.
- [42] N. V. Voshchinnikov and V. G. Farafonov. “Optical properties of spheroidal particles”. In: *Astrophysics and Space Science* 204 (1993), pp. 19–86. DOI: 10.1007/BF00658095.
- [43] L.-W. Li et al. “Computations of spheroidal harmonics with complex arguments: A review with an algorithm”. In: *Phys. Rev. E* 58 (1998), pp. 6792–6806. DOI: 10.1103/PhysRevE.58.6792.
- [44] P. C. Waterman. “Symmetry, Unitarity, and Geometry in Electromagnetic Scattering”. In: *Phys. Rev. D* 3 (1971), pp. 825–839. DOI: 10.1103/PhysRevD.3.825.
- [45] M. I. Mishchenko. *Light scattering by nonspherical particles : theory, measurements, and applications*. Academic Press, 2000.
- [46] M. I. Mishchenko et al. “Comprehensive T-matrix reference database: A 2004-2006 update”. In: *Journal of Quantitative Spectroscopy and Radiative Transfer* 106 (2007), pp. 304–324. DOI: 10.1016/j.jqsrt.2007.01.022.
- [47] M. I. Mishchenko et al. “Comprehensive T-matrix reference database: A 2007-2009 update”. In: *Journal of Quantitative Spectroscopy and Radiative Transfer* 111 (2010), pp. 650–658. DOI: 10.1016/j.jqsrt.2009.11.002.
- [48] J. A. Stratton and L. J. Chu. “Diffraction Theory of Electromagnetic Waves”. In: *Phys. Rev.* 56 (1939), p. 99. DOI: 10.1103/PhysRev.56.99.
- [49] A. Doicu and T. Wriedt. “Near-field computation using the null-field method”. In: *Journal of Quantitative Spectroscopy and Radiative Transfer* 111 (2010), pp. 466–473. DOI: DOI:10.1016/j.jqsrt.2009.10.003.

Bibliography

- [50] P. W. Barber and S. C. Hill. *Light scattering by particles: computational methods*. World Scientific Publishing, 1990.
- [51] W. H. Reed and T. R. Hill. “Triangular mesh methods for the neutron transport equation, Technical Report, LA-UR-73-479”. In: *Los Alamos Scientific Laboratory Technical* (1973), pp. 1–23. DOI: [ReedHil11973](https://doi.org/10.2172/111973).
- [52] J. Hesthaven and T. Warburton. “Nodal High-Order Methods on Unstructured Grids: I. Time-Domain Solution of Maxwell’s Equations”. In: *Journal of Computational Physics* 181 (2002), pp. 186–221. DOI: [10.1006/jcph.2002.7118](https://doi.org/10.1006/jcph.2002.7118).
- [53] K. Busch, M. König, and J. Niegemann. “Discontinuous Galerkin methods in nanophotonics”. In: *Laser & Photonics Reviews* 5 (2011), pp. 773–809. DOI: [10.1002/lpor.201000045](https://doi.org/10.1002/lpor.201000045).
- [54] J. S. Hesthaven and T. Warburton. *Nodal Discontinuous Galerkin Methods: Algorithms, Analysis, and Applications*. Springer, 2008.
- [55] T. Warburton. “An explicit construction of interpolation nodes on the simplex”. In: *Journal of Engineering Mathematics* 56 (2006), pp. 247–262. DOI: [10.1007/s10665-006-9086-6](https://doi.org/10.1007/s10665-006-9086-6).
- [56] M. H. Carpenter and C. A. Kennedy. “Fourth-order 2N-storage Runge-Kutta schemes”. In: *Nasa Technical Report* 109112 (1994).
- [57] G. G. Dahlquist. “A special stability problem for linear multistep methods”. In: *BIT Numerical Mathematics* 3 (1963), pp. 27–43. DOI: [10.1007/BF01963532](https://doi.org/10.1007/BF01963532).
- [58] R. Diehl, K. Busch, and J. Niegemann. “Comparison of Low-Storage Runge-Kutta Schemes for Discontinuous Galerkin Time-Domain Simulations of Maxwell’s Equations”. In: *Journal of Computational and Theoretical Nanoscience* 7 (2010), pp. 1572–1580. DOI: [doi:10.1166/jctn.2010.1521](https://doi.org/10.1166/jctn.2010.1521).
- [59] J. Niegemann, R. Diehl, and K. Busch. “Efficient low-storage Runge-Kutta schemes with optimized stability regions”. In: *Journal of Computational Physics* 231 (2012), pp. 364–372. DOI: [10.1016/j.jcp.2011.09.003](https://doi.org/10.1016/j.jcp.2011.09.003).
- [60] J.-P. Berenger. “A Perfectly Matched Layer for the Absorption of Electromagnetic Waves”. In: *Journal of Computational Physics* 114 (1994), pp. 185–200.
- [61] S. Gedney. “An anisotropic perfectly matched layer-absorbing medium for the truncation of FDTD lattices”. In: *Antennas and Propagation, IEEE Transactions on* 44 (1996), pp. 1630–1639. DOI: [10.1109/8.546249](https://doi.org/10.1109/8.546249).
- [62] J. Niegemann et al. “Higher-order time-domain methods for the analysis of nanophotonic systems”. In: *Photonics and Nanostructures - Fundamentals and Applications* 7 (2009), pp. 2–11. DOI: [10.1016/j.photonics.2008.08.006](https://doi.org/10.1016/j.photonics.2008.08.006).
- [63] P. Monk. *Finite Element Methods for Maxwell’s Equations*. Numerical Analysis and Scientific Computation Series. Oxford, 2003.
- [64] Y. Saad and M. H. Schultz. “GMRES: A Generalized Minimal Residual Algorithm for Solving Nonsymmetric Linear Systems”. In: *SIAM Journal on Scientific and Statistical Computing* 7 (1986), pp. 856–869. DOI: [10.1137/0907058](https://doi.org/10.1137/0907058).

Bibliography

- [65] K. Yee. “Numerical solution of initial boundary value problems involving maxwell’s equations in isotropic media”. In: *Antennas and Propagation, IEEE Transactions on* 14 (1966), pp. 302–307. DOI: 10.1109/TAP.1966.1138693.
- [66] R. Holland. “Pitfalls of staircase meshing”. In: *Electromagnetic Compatibility, IEEE Transactions on* 35 (1993), pp. 434–439. DOI: 10.1109/15.247856.
- [67] A. Cangellaris and D. Wright. “Analysis of the numerical error caused by the stair-stepped approximation of a conducting boundary in FDTD simulations of electromagnetic phenomena”. In: *Antennas and Propagation, IEEE Transactions on* 39 (1991), pp. 1518–1525. DOI: 10.1109/8.97384.
- [68] C. Hafner. *MaX-1: A Visual Electromagnetics Platform for PCs*. Wiley, 1998.
- [69] E. M. Purcell and C. R. Pennypacker. “Scattering and Absorption of Light by Nonspherical Dielectric Grains”. In: *Astrophysical Journal* 186 (1973), pp. 705–714. DOI: 10.1086/152538.
- [70] B. T. Draine and P. J. Flatau. “Discrete-dipole approximation for scattering calculations”. In: *J. Opt. Soc. Am. A* 11 (1994), pp. 1491–1499. DOI: 10.1364/JOSAA.11.001491.
- [71] B. T. Draine and P. J. Flatau. “User Guide for the Discrete Dipole Approximation Code DDSCAT 7.0”. In: (2008).
- [72] N. Geuquet and L. Henrard. “EELS and optical response of a noble metal nanoparticle in the frame of a discrete dipole approximation”. In: *Ultramicroscopy* 110 (2010), pp. 1075–1080. DOI: DOI:10.1016/j.ultramic.2010.01.013.
- [73] F. J. García de Abajo and A. Howie. “Relativistic Electron Energy Loss and Electron-Induced Photon Emission in Inhomogeneous Dielectrics”. In: *Phys. Rev. Lett.* 80 (1998), pp. 5180–5183. DOI: 10.1103/PhysRevLett.80.5180.
- [74] J. Qiu et al. “Space-selective precipitation of metal nanoparticles inside glasses”. In: *Applied Physics Letters* 81 (2002), pp. 3040–3042. DOI: 10.1063/1.1509095.
- [75] J. Qiu et al. “Manipulation of Gold Nanoparticles inside Transparent Materials”. In: *Angewandte Chemie International Edition* 43 (2004), pp. 2230–2234. DOI: 10.1002/anie.200352380.
- [76] X. Jiang et al. “Laser-controlled dissolution of gold nanoparticles in glass”. In: *Chemical Physics Letters* 391 (2004), pp. 91–94. DOI: DOI:10.1016/j.cplett.2004.04.061.
- [77] M. Kaempfe et al. “Ultrashort laser pulse induced deformation of silver nanoparticles in glass”. In: *Applied Physics Letters* 74 (1999), pp. 1200–1202. DOI: 10.1063/1.123498.
- [78] H. Hofmeister, W.-G. Drost, and A. Berger. “Oriented prolate silver particles in glass – characteristics of novel dichroic polarizers”. In: *Nanostructured Materials* 12 (1999), pp. 207–210. DOI: DOI:10.1016/S0965-9773(99)00100-2.

Bibliography

- [79] K. J. Berg, A. Berger, and H. Hofmeister. “Small silver particles in glass surface layers produced by sodium-silver ion exchange their concentration and size depth profile”. In: *Zeitschrift für Physik D Atoms, Molecules and Clusters* 20 (1991), pp. 309–311. DOI: 10.1007/BF01543998.
- [80] A. Stalmashonak, G. Seifert, and H. Graener. “Optical three-dimensional shape analysis of metallic nanoparticles after laser-induced deformation”. In: *Opt. Lett.* 32 (2007), pp. 3215–3217. DOI: 10.1364/OL.32.003215.
- [81] A. Stalmashonak et al. “Intensity-driven, laser induced transformation of Ag nanospheres to anisotropic shapes”. In: *Applied Physics B: Lasers and Optics* 94 (2009), pp. 459–465. DOI: 10.1007/s00340-008-3309-7.
- [82] A Stalmashonak, G Seifert, and H Graener. “Spectral range extension of laser-induced dichroism in composite glass with silver nanoparticles”. In: *Journal of Optics A: Pure and Applied Optics* 11 (2009), 065001 (5pp). DOI: 10.1088/1464-4258/11/6/065001.
- [83] A. A. Ünal. “Time-resolved investigations on ultrafast shape modification dynamics of silver nanoparticles embedded in glass”. PhD thesis. Martin-Luther-Universität Halle-Wittenberg, 2009.
- [84] F. J. García de Abajo. “Optical excitations in electron microscopy”. In: *Rev. Mod. Phys.* 82 (2010), pp. 209–275. DOI: 10.1103/RevModPhys.82.209.
- [85] R. F. Egerton. “Electron energy-loss spectroscopy in the TEM”. In: *Reports on Progress in Physics* 72 (2009), 016502 (25pp). DOI: 10.1088/0034-4885/72/1/016502.
- [86] B. Fultz. “Introduction”. In: *Transmission Electron Energy Loss Spectrometry in Materials Science and The EELS Atlas*. Wiley-VCH Verlag GmbH & Co. KGaA, 2005, pp. 1–19. DOI: 10.1002/3527605495.ch1.
- [87] W. H. RICHARDSON. “Bayesian-Based Iterative Method of Image Restoration”. In: *J. Opt. Soc. Am.* 62 (1972), pp. 55–59. DOI: 10.1364/JOSA.62.000055.
- [88] L. B. Lucy. “An iterative technique for the rectification of observed distributions”. In: *Astronomical Journal* 79 (1974), p. 745. DOI: 10.1086/111605.
- [89] M. Bosman et al. “Mapping surface plasmons at the nanometre scale with an electron beam”. In: *Nanotechnology* 18 (2007), 165505 (5pp). DOI: 10.1088/0957-4484/18/16/165505.
- [90] B. Schaffer et al. “High-resolution surface plasmon imaging of gold nanoparticles by energy-filtered transmission electron microscopy”. In: *Physical Review B (Condensed Matter and Materials Physics)* 79, 041401 (2009), p. 041401. DOI: 10.1103/PhysRevB.79.041401.
- [91] M.-W. Chu et al. “Probing surface plasmons in individual Ag nanoparticles in the ultra-violet spectral regime”. In: *Nanotechnology* 20 (2009), 235705 (5pp). DOI: 10.1088/0957-4484/20/23/235705.

Bibliography

- [92] W. Sigle et al. “Electron energy losses in Ag nanoholes—from localized surface plasmon resonances to rings of fire”. In: *Opt. Lett.* 34 (2009), pp. 2150–2152. DOI: 10.1364/OL.34.002150.
- [93] A. L. Koh et al. “Electron Energy-Loss Spectroscopy (EELS) of Surface Plasmons in Single Silver Nanoparticles and Dimers: Influence of Beam Damage and Mapping of Dark Modes”. In: *ACS Nano* 3 (2009), pp. 3015–3022. DOI: 10.1021/nn900922z.
- [94] F. Song et al. “Visualizing Plasmon Coupling in Closely Spaced Chains of Ag Nanoparticles by Electron Energy-Loss Spectroscopy”. In: *Small* 6 (2010), pp. 446–451. DOI: 10.1002/smll.200901639.
- [95] M.-W. Chu et al. “Probing Bright and Dark Surface-Plasmon Modes in Individual and Coupled Noble Metal Nanoparticles Using an Electron Beam”. In: *Nano Letters* 9 (2009), pp. 399–404. DOI: 10.1021/nl803270x.
- [96] P. Chaturvedi et al. “Imaging of Plasmonic Modes of Silver Nanoparticles Using High-Resolution Cathodoluminescence Spectroscopy”. In: *ACS Nano* 3 (2009), pp. 2965–2974. DOI: 10.1021/nn900571z.
- [97] F. J. García de Abajo and M. Kociak. “Probing the Photonic Local Density of States with Electron Energy Loss Spectroscopy”. In: *Phys. Rev. Lett.* 100 (2008), p. 106804. DOI: 10.1103/PhysRevLett.100.106804.
- [98] U. Hohenester, H. Ditlbacher, and J. R. Krenn. “Electron-Energy-Loss Spectra of Plasmonic Nanoparticles”. In: *Physical Review Letters* 103, 106801 (2009), p. 106801. DOI: 10.1103/PhysRevLett.103.106801.
- [99] T. L. Ferrell and P. M. Echenique. “Generation of Surface Excitations on Dielectric Spheres by an External Electron Beam”. In: *Phys. Rev. Lett.* 55 (1985), pp. 1526–1529. DOI: 10.1103/PhysRevLett.55.1526.
- [100] N. Zabala and A. Rivacoba. “Electron energy loss near supported particles”. In: *Phys. Rev. B* 48 (1993), pp. 14534–14542. DOI: 10.1103/PhysRevB.48.14534.
- [101] B. L. Illman et al. “Spectrum of surface-mode contributions to the differential energy-loss probability for electrons passing by a spheroid”. In: *Phys. Rev. B* 38 (1988), pp. 3045–3049. DOI: 10.1103/PhysRevB.38.3045.
- [102] P. E. Batson. “Surface Plasmon Coupling in Clusters of Small Spheres”. In: *Phys. Rev. Lett.* 49 (1982), pp. 936–940. DOI: 10.1103/PhysRevLett.49.936.
- [103] F. J. García de Abajo. “Relativistic energy loss and induced photon emission in the interaction of a dielectric sphere with an external electron beam”. In: *Phys. Rev. B* 59 (1999), pp. 3095–3107. DOI: 10.1103/PhysRevB.59.3095.
- [104] D. Tskhakaya. “Computational Many-Particle Physics”. In: ed. by H. Fehnske, R. Scheider, and A. Weiße. *Lecture Notes in Physics 739*. Springer, 2008. Chap. Chapter 6: The Particle-in-Cell Method.
- [105] L. Novotny and N. van Hulst. “Antennas for light”. In: *Nat Photon* 5 (2011), pp. 83–90. DOI: 10.1038/nphoton.2010.237.

Bibliography

- [106] S. Sederberg and A. Elezzabi. “Sierpinski fractal plasmonic antenna: a fractal abstraction of the plasmonic bowtie antenna”. In: *Opt. Express* 19 (2011), pp. 10456–10461. DOI: 10.1364/OE.19.010456.
- [107] P. Alitalo and S. Tretyakov. “Electromagnetic cloaking with metamaterials”. In: *Materials Today* 12 (2009), pp. 22–29. DOI: DOI:10.1016/S1369-7021(09)70072-0.
- [108] G. Boudarham et al. “Spectral Imaging of Individual Split-Ring Resonators”. In: *Phys. Rev. Lett.* 105 (2010), p. 255501. DOI: 10.1103/PhysRevLett.105.255501.
- [109] F. Falcone et al. “Babinet Principle Applied to the Design of Metasurfaces and Metamaterials”. In: *Phys. Rev. Lett.* 93 (2004), p. 197401. DOI: 10.1103/PhysRevLett.93.197401.

Publication List

- [M1] A. Stalmashonak, C. Matyssek, O. Kiriyenko, W. Hergert, H. Graener, and G. Seifert. “Preparing large-aspect-ratio prolate metal nanoparticles in glass by simultaneous femtosecond multicolor irradiation”. In: *Opt. Lett.* 35 (2010), pp. 1671–1673. DOI: 10.1364/OL.35.001671.
- [M2] M. Karamehmedović, R. Schuh, V. Schmidt, T. Wriedt, C. Matyssek, W. Hergert, A. Stalmashonak, G. Seifert, and O. Stranik. “Comparison of numerical methods in near-field computation for metallic nanoparticles”. In: *Opt. Express* 19 (2011), pp. 8939–8953. DOI: 10.1364/OE.19.008939.
- [M3] F. von Cube, S. Irsen, J. Niegemann, C. Matyssek, W. Hergert, K. Busch, and S. Linden. “Spatio-spectral characterization of photonic meta-atoms with electron energy-loss spectroscopy”. In: *Opt. Mater. Express* 1 (2011), pp. 1009–1018.
- [M4] C. Matyssek, J. Niegemann, W. Hergert, and K. Busch. “Computing electron energy loss spectra with the Discontinuous Galerkin Time-Domain method”. In: *Photonics and Nanostructures - Fundamentals and Applications* 9 (2011), pp. 367–373. DOI: 10.1016/j.photonics.2011.04.003.

Submitted Manuscripts

- C. Matyssek, V. Schmidt, W. Hergert, Th. Wriedt: The T-Matrix method in electron energy loss and cathodoluminescence spectroscopy calculations for metallic nano-particles.
Submitted to *Ultramicroscopy* 24.02.2012, revised 03.03.2012.
- M. Beleites, C. Matyssek, H.-H. Blaschek, G. Seifert: Near-field optical microscopy of femtosecond laser reshaped silver nanoparticles in dielectric matrix
Submitted to *Nano Research Letters* 02.03.2012

Curriculum Vitae

Personal Data

Name Christian Felix Matyssek
Born 28th of December 1982 in Rinteln, Niedersachsen
Parents Volkhard Matyssek and Brigitte Matyssek, née Mönke

Education

08/1989–07/1993 Grundschule Quernheim, Kirchlengern
08/1993–06/2002 Freiherr-vom-Stein Gynmasium, Bünde
10/2003–09/2008 Studies in Physics at Martin Luther University Halle-Wittenberg (MLU)
18.09.2008 Diploma in Physics from MLU. Thesis title: *Optimierung photonischer Kristalle mittels Finite Difference Time Domain (FDTD) und genetischen Algorithmen*

Employment

10/2008–03/2012 Employment at the Max Planck Institute of Microstructure Physics, Halle (PhD position)

Halle, 30.03.2012

Signature

Eidesstattliche Erklärung

Ich erkläre hiermit, dass ich die vorliegende Arbeit selbständig und ohne fremde Hilfe verfasst habe und keine anderen als die angegebenen Quellen und Hilfsmittel benutzt habe. Stellen, die aus den benutzten Quellen wörtlich oder inhaltlich übernommen wurden, sind als solche kenntlich gemacht. Ferner erkläre ich, dass ich bisher keine Promotionsversuche unternommen habe und diese Dissertation an keiner anderen Institution eingereicht habe.

Halle, den 30.03.2012

Unterschrift

Acknowledgements

First of all, I would like to thank my supervisor Prof. Dr. Wolfram Hergert for the opportunity to write this thesis and especially for his confidence to let me work on a new exciting subject that was not among the well established topics at the institute. Also, this thesis would not have been possible without the interest in Plasmonics of the late Director of the Experimental Department 2 of the MPI Halle, Prof. Dr. Ulrich Gösele. His sudden and unexpected passing was a shock, not only to the Institute. I commemorate him and hope that he would have liked the results of this thesis. I am grateful to Prof. Dr. E.K.U. Gross, who took Prof. Gösele's place of being my mentor in the International Max Planck Research School for Science and Technology of Nanostructures. This work would also not have been possible without a number of people, with whom I had the privilege to work with. This includes the Optics Group of the MLU Halle, especially Prof. Dr. Heinrich Graener, Dr. Gerhard Seifert, Dr. Andrei Stalmashonak and Moritz Beleites. I would like to thank Dr. Reinald Hillebrand, MPI Halle, who initiated the first meetings with Dr. Katja Höflich and Dr. Andreas Berger to discuss plasmonics. Without the EELS experiments performed by Dr. Berger we would never have pursued this topic. Also, I was lucky to have contact to Prof. Dr. Kurt Busch and Dr. Jens Niegemann, to that time at the Karlsruhe Institute of Technology. Without them we would never have used the DGTD method for EELS and I thank them for their support, the opportunity to use and extend the DG Code developed in the group in Karlsruhe and for a collaboration that I have definitely benefited from. Along with this, I thank Felix v. Cube, Dr. Stephan Irsen and Prof. Dr. Stefan Linden in Bonn for the nice experiments and for choosing the DGTD for the corresponding simulations.

An equally enjoyable collaboration began at the conference *Mie 1908-2008* in December 2008 in Halle. There, I was introduced to Dr. Thomas Wriedt. With him and his group at the Institut für Werkstofftechnik in Bremen, especially Dr. Mirza Karamehmedovic and Vladimir Schmidt, PhD., we did not only undertake the comparison of different numerical methods for light-scattering, they also gave me great support when I got the idea to use the T-Matrix method for electron microscopy.

Beside the *far-field*, we have seen in this thesis, that the *near-field* is important as well. This also holds true for the every-day work. I would like to thank all the people at the Institute, especially in the Computational Physics Group. This includes Dr. Guntram Fischer, Dr. Steven Achilles, Dr. Michael Hengst, Stephan Borek, Nicki Hinsche, Michael Strauch, and all the other people I shared the coffee machine with. Also, I would like to thank Stefan Thomas for spotting some mistakes in the drafts of this work.

Last and definitively not least, I would like to thank the Referees for reading my thesis.